Dynamics of an electrolyte–*n*-type silicon system during anodization in hydrofluoric acid solutions

É. Yu. Buchin and A. V. Prokaznikov

Institute of Microelectronics, Russian Academy of Sciences, Yaroslavl'
(Submitted November 5, 1996)
Pis'ma Zh. Tekh. Fiz. **23**, 1–7 (March 12, 1997)

The dynamics of the morphology of porous silicon during anodization in hydrofluoric acid has been investigated. The current-voltage characteristics and their variation with time as well as the time dependence of the voltage in an electrolyte–silicon system are highly informative for the construction of a general theory of pore formation in silicon. Attention is drawn to the possible existence of a bifurcation in the transition to harmonic oscillations of $U(t)$ in the course of anodization. In this case, the laws governing the pore formation processes before and after the bifurcation will obviously differ. © *1997 American Institute of Physics.* [S1063-7850(97)00103-1]

Following the observation of various unusual new properties after special electrochemical treatment of silicon, considerable interest has been shown in studying the characteristics of this material, since its use offers the possibility of returning to traditional, less expensive, silicon technology even in cases where other substances and materials have generally been used. Many studies have therefore focused on the physicochemical properties of this new material, known as porous silicon, and on its behavior during fabrication. The processes taking place in the course of pore formation can be deduced from the dynamics of the main parameters of the system and from the final morphology of the porous structure. The dynamic behavior of the parameters of a hydrofluoric acid (HF)-silicon (Si) system during the pore formation processes and aspects of the morphology of the final porous structure have not been examined sufficiently comprehensively.[1,2] The dynamics of the behavior of the current-voltage characteristics obtained during the anodization of lightly doped *n*-type silicon was studied in Ref. 2. The potential-time curves plotted in Ref. 2 indicate that the potential exhibits fairly complex nonlinear time behavior. The morphological aspect of the problem was considered in Refs. 3–5. The behavior of the pore formation process was determined by a potential distribution with a maximum at the end of the pore. However the equations determining the kinetics of the chemical reaction did not appear directly in the expression for the pore growth rate. Approaches based on the random walk model[6] made no explicit allowance for the potential distribution.

An original method was proposed in Ref. 7, based on a model which was developed in Ref. 8. However, although the proposed model can account for the possible formation of several types of pore morphologies, it cannot be treated as definitive because the behavior of the transverse dimensions of the micropores as a function of the applied potential does not agree satisfactorily with the experiment when describing the formation of *n*-type porous silicon. Note that at present the theory of pore formation in silicon is far from complete.[1]

This reasoning indicates that there is a definite need for further studies of the system to evolve new approaches to the development of a general theory of pore formation in silicon. An investigation of the current-voltage characteristics and their variation with time, as well as the time-dependent behavior of the voltage $U(t)$ for an electrolyte-silicon system can provide a wealth of information for developing a general theory of pore formation in silicon. Information on the physicochemical processes taking place in an electrolyte-silicon system during anodization can be gleaned from a study of the current-voltage characteristics, their time variation, and the behavior of $U(t)$.

In the present paper we investigate the dynamics of the behavior of the HF-*n*-type Si system during anodization in mixtures of hydrofluoric acid and isopropanol in ratios of 1:1 and 1:3 by volume. Arguments are presented to support the hypothesis that the complex behavior of the dynamic variables $U(t)$ and $\dot{U}(t)$ ($\dot{U}(t)$ is the time derivative) in the HF-Si system indicates that bifurcations of the transition to the limit cycle may exist in the system.[9] Particular attention is focused on how the morphology of the porous silicon is influenced by anodization conditions for which the behavior of the system parameters may be described by different dynamics.

The experimental method was described in Refs. 10–13 and the current-voltage characteristics and potential-time curves were recorded by a standard method using KÉF-20 silicon samples. It was observed that when the following parameters were varied within specific ranges: temperature (T) 20–40 °C, optical power density incident on sample (J) 0.06–0.1 W/cm^2, current density $j \leqslant 50$mA/cm^2, and anodization time between 30 s and 5 min, for a specific 1:3 concentration of HF-isopropanol electrolyte, the current-voltage characteristics exhibit clearly defined nonmonotonic time behavior, so that the current-voltage characteristic (or some parts thereof) obtained at time τ_3 after the beginning of anodization is situated between the characteristics obtained at times τ_1 and τ_2 (where $\tau_1 < \tau_2 < \tau_3$, see Fig. 1). For a 1:3 HF-isopropanol electrolyte, the current-voltage characteristics exhibit an appreciable periodic rise and fall with time, which is reflected in the nonmonotonic behavior of the characteristics. Note that the general trend of the current-voltage

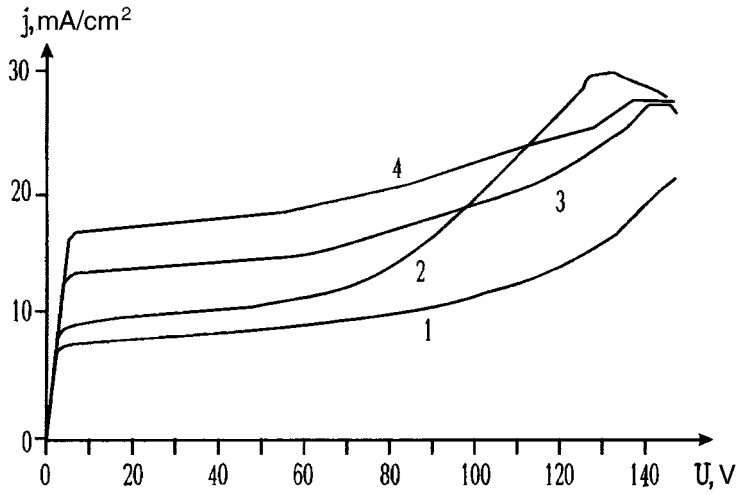

FIG. 1. Current–voltage characteristics obtained during anodization in a 1:3 by volume HF-isopropanol electrolyte: *1* — immediately after the beginning of anodization; *2* — 1 min after the beginning of anodization; *3* — 2 min after the beginning of anodization; *4* — 3 min after the beginning of anodization. The stabilized voltage was swept linearly at 10 V/s.

characteristics with time is a rise along the j axis.

The 1:1 HF-isopropanol electrolyte typically has a resonance curve $U(t)$ whose amplitude depends on the parameters of the system (Fig. 2). The curve of $U(t)$ corresponding to the formation of the third type of morphology (see the classification given in Refs. 10–12) has a clearly visible section of oscillating $U(t)$. For the curves of $U(t)$ corresponding to the formation of other types of morphology, these oscillations still exist but are less noticeable. We stress that the phase diagram in the coordinates $U(t)$, $\dot{U}(t)$ corresponding to $t\to\infty$ is clearly a coiling spiral. It has been noted that the potential-time diagrams in the form of resonant curves exhibit oscillations on the descending part of $U(t)$ and the amplitude of these oscillations increases as the isopropanol content is increased and the illumination of the sample decreases. This effect is observed particularly clearly for $j>20$ mA/cm^2 (Fig. 2).

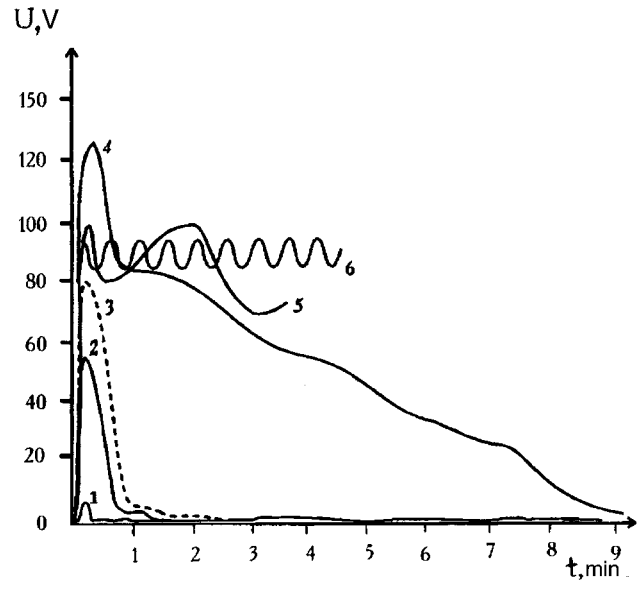

FIG. 2. Voltage U versus time t in an electrolyte–n-type silicon system obtained during anodization under various conditions for a 1:1 by volume HF-isopropanol electrolyte: *1* — curve of $U(t)$ corresponding to the formation of porous silicon with the zeroth type of morphology, *2* — $U(t)$ for the first type of morphology, *3* — $U(t)$ for the second type of morphology, *4* — $U(t)$ for the third type of morphology. Curves of $U(t)$ for a 1:3 by volume HF-isopropanol electrolyte: *5, 6* — $U(t)$ obtained under different conditions of illumination of an anodized sample, where curve *6* corresponds to a higher illumination intensity than curve *5*.

The behavior of $U(t)$ changes radically when the electrolyte contains HF and isopropanol in the ratio 1:3 by volume. Under certain anodization conditions, the curve $U(t)$ exhibits clearly defined oscillating behavior. The amplitude and frequency of the oscillations depend on the parameters of the system (in this case, on the illumination conditions of the silicon sample). On the phase diagrams of $U(t)$ versus $\dot{U}(t)$ this motion will correspond to closed trajectories. All the above reasoning supports the assumption that the creation of periodic motion in a HF–n-type Si system exhibits a bifurcation, i.e., that limit cycles exist in this dynamic system.

Note that the curves $U(t)$ for HF and isopropanol in the ratio 1:1 describe the formation of a fairly uniform homogeneous structure of macropores with different types of morphology depending on the choice of operating point on the current-voltage characteristic[10–12] and the formation of the porous structure is entirely controllable by selecting the operating point on this characteristic.

For the strictly oscillating curve $U(t)$, the porous structure exhibits an inhomogeneous morphology and usually consists of layers of pores of different length with self-similar pore shapes on different scales, either a fairly unusual alternation of the ''shower'' structure and a structure comprising a bundle of pores diverging from a common center (described in Ref. 14 as a ''cauliflower'' structure) or a ''swallowtail'' structure.

To sum up, we note that the transition to harmonic oscillations during anodization of n-type Si may exhibit a bifurcation for a 1:3 by volume HF-isopropanol electrolyte. This is accompanied by radical changes to the morphology of the porous structure so that the relationships describing pore formation before the bifurcation are clearly different from those describing these processes after the establishment of harmonic oscillations of $U(t)$.

These relationships suggest that the behavior of this sys-

tem is similar in many respects to that of a nonlinear system such as a van der Pol oscillator under soft excitation.[9] This oscillator system has been fairly comprehensively studied and various relations have been established to link the main parameters of the system (effective resistance, capacitance, and so forth) with the parameters of the phase trajectories. Thus a more detailed study of the behavior described above as a function of changes in the parameters of the system may shed light on the essential nature of the processes responsible for pore formation. These effects also allow us to utilize the well-developed mathematical apparatus for describing self-organizing systems to construct a theory of pore formation in silicon.

It should be stressed that further more detailed studies of this problem are required, with particular emphasis on the nature of the bifurcations and the nature of the transition from one anodization regime to another and how they depend on the various parameters of the system. We also need to consider how the behavior of this effect is influenced by the electrical circuit and the characteristics of the devices.

[1] R. L. Smith and S. D. Collins, J. Appl. Phys. **71**, R1 (1992).
[2] S. O. Izidinov, A. P. Blokhina, and T. S. Martynova, Elektrokhimiya **21**, 1172 (1985).
[3] M. I. J. Beale, J. D. Benjamin, M. J. Uren, N. G. Chew, and A. G. Cullis, J. Cryst. Growth **73**, 622 (1985).
[4] X. G. Zhang, J. Electrochem. Soc. **138**, 3750 (1991).
[5] V. Lehmann, J. Electrochem. Soc. **140**, 2836 (1993).
[6] B. I. Smith, S. -F. Chuang, and S. D. Collins, J. Electron. Mater. **17**, 533 (1988).
[7] V. P. Parkhutik, J. M. Albella, J. M. Martinez-Duart, J. M. Gómez-Rodríguez, A. M. Baró, and V. I. Shershulsky, Appl. Phys. Lett. **62**, 366 (1993)
[8] V. P. Parkhutik and V. I. Shershulsky, J. Phys. D **25**, 1258 (1992).
[9] A. A. Andronov, A. A. Vitt, and S. E. Khaĭkin, *Oscillation Theory* [in Russian], Nauka, Moscow (1981).
[10] É. Yu. Buchin, A. V. Postinikov, A. V. Prokaznikov, V. B. Svetovoĭ, and A. B. Churilov, Pis'ma Zh. Tekh. Fiz. **21**(1), 60 (1995) [Tech. Phys. Lett. **21**, 27 (1995)].
[11] E. Yu. Buchin, A. B. Churilov, A. V. Postnikov, A. V. Prokaznikov, and V. B. Svetovoy, Phys. Low-Dim. Struct. **2/3**, 97 (1995).
[12] E. Yu. Buchin, A. B. Churilov, and A. V. Postnikov, in *Proc. Intern. Symposium: ''Si Heterostructures: from Physics to Devices,''* Fodele, Crete, 1995, p. 149.
[13] Y. Arita and Y. Sunohara, J. Electrochem. Soc. **124**, 285 (1977).
[14] J. C. Russ, *Fractal Surfaces* (Plenum Press, New York, 1994).

Translated by R. M. Durham

Photoluminescence properties of $Al_xGa_{1-x}As$ epitaxial layers grown under conditions of ultrafast flux cooling

A. V. Abramov, A. G. Deryagin, N. G. Deryagin, S. I. Kokhanovskiĭ, V. I. Kuchinskiĭ, E. U. Rafailov, G. S. Sokolovskiĭ, and D. N. Tret'yakov

A. F. Ioffe Physicotechnical Institute, Russian Academy of Sciences, St. Petersburg
(Submitted October 11, 1996)
Pis'ma Zh. Tekh. Fiz. **23**, 8–13 (March 12, 1997)

Results are presented of studies of the photoluminescence properties of epitaxial layers of $Al_xGa_{1-x}As$ solid solutions grown by liquid-phase epitaxy with nonequilibrium crystallization achieved by ultrafast rates of cooling of the flux ($V \sim 10^2$–10^3 °C/s). The photoluminescence characteristics obtained indicate that the epitaxial layers are of high quality. It is also observed that when samples with $x_{buff} = 0.5$–0.55 are exposed to laser radiation of power density ~ 1 kW/cm^2 at a temperature of 77 K, the spectral composition of the radiation undergoes irreversible changes caused by the formation of an arsenic vacancy (V_{As})-donor impurity complex. © *1997 American Institute of Physics.* [S1063-7850(97)00203-6]

Solid solutions of $Al_xGa_{1-x}As$ are widely used to fabricate microelectronics and optoelectronics devices. In the method of liquid-phase epitaxy $Al_xGa_{1-x}As$–GaAs heterostructures are usually grown under conditions very close to equilibrium. The last few years have seen the introduction of a method of liquid-phase epitaxy where crystallization conditions far from equilibrium are achieved by ultrafast cooling of the flux.[1] It was shown in Ref. 2 that these crystallization conditions alter various parameters of the layers such as the thickness, the depth distribution of the composition, and the carrier concentration. In the present paper we report results of an investigation of the photoluminescence properties of epitaxial layers of AlGaAs solid solutions grown by nonequilibrium crystallization achieved by ultrafast cooling of the flux at rates of $\sim 10^2$– 10^3 °C/s (Ref. 2).

The photoluminescence characteristics were investigated by pumping the samples with radiation from an LG-106 argon laser ($\lambda_{pump} \cong 0.5 \mu$m) at temperatures of 77 K and 2 K. The pump power density was varied in the range 10–1000 W/cm^2. The samples consisted of a multilayer structure formed by an n-GaAs(100) substrate, on which was grown an $Al_xGa_{1-x}As$ buffer layer (x_{buff}=0.05–0.65) of constant composition, followed by an $Al_xGa_{1-x}As$ layer whose composition varied with thickness, grown under conditions of ultrafast variation in the temperature of the liquid phase. It should be noted that regardless of the aluminum content in the buffer layer, the AlAs distribution of the layer of variable composition has a characteristic minimum.[2]

Figure 1 shows photoluminescence spectra of samples having different AlAs contents in the buffer layer. The inset shows the typical distribution of AlAs over the thickness (d) of these structures. The samples may be divided into three groups: 1) samples having an AlAs content in the buffer layer $x \leqslant 0.45$, for which the value of x near the minimum corresponds to a direct band-gap structure of the $Al_xGa_{1-x}As$ solid solution; 2) samples having an AlAs content in the buffer layer $0.5 \leqslant x \leqslant 0.55$, for which the value of x near the minimum is close to the direct-indirect band-gap transition, and 3) samples having a high AlAs content ($x \sim 0.60$–0.65) in the buffer layer, for which the AlAs content near the minimum corresponds to an indirect band-gap structure.

The photoluminescence spectrum shown in Fig. 1 for a sample having an AlAs content $x \cong 0.26$ in the buffer layer is typical of all samples in the first group. It can be seen that the spectrum has two peaks. The short-wavelength peak is assigned to emission from that part of the sample having the minimum AlAs content while the long-wavelength peak is attributed to emission from the substrate. The spectral position of the short-wavelength peak can be used to determine the composition of the $Al_xGa_{1-x}As$ solid solution corresponding to this emission. We used the following relation linking the photoluminescence radiation energy with the AlAs content in the solid solution:[3]

$$E_{pl}(77\ \text{e}) = 1.508 + 1.443x, \tag{1}$$

where E_{pl} is the photon energy at the maximum and x is the composition of the $Al_xGa_{1-x}As$ solid solution. The AlAs content calculated according to formula (1) agrees well with the value of x determined by secondary ion mass spectroscopy. For example, for a structure with $x_{buff} = 0.26$, whose photoluminescence spectrum is shown in Fig. 1, the AlAs content calculated according to formula (1) is 12.6 mol%, while that determined by secondary ion mass spectrometry is 11.8 mol%. The experimentally determined half-widths of the photoluminescence short-wavelength maximum, $\Delta h\nu$, were 12–50 meV. It should be noted that the lowest values $\Delta h\nu$=12 meV were observed for samples having a fairly long ($\sim 0.3 \mu$m) region of almost constant composition near the minimum. These values of $\Delta h\nu$ indicate that the epitaxial layers grown under conditions of ultrafast cooling of the flux are of high quality.

The photoluminescence spectra of the third type of samples typically reveal a low-intensity short-wavelength band. This band is attributed to recombination of carriers in the indirect-gap material $Al_xGa_{1-x}As$. Some contribution of

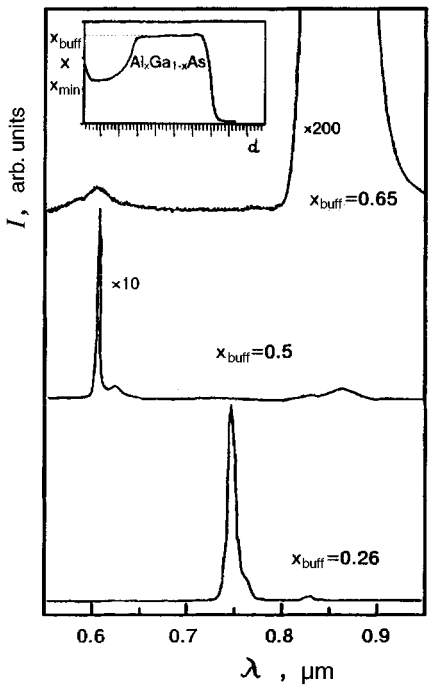

FIG. 1. Photoluminescence spectra measured at $T = 77$ K for $Al_xGa_{1-x}As$ epitaxial layers with different contents x in the buffer layer. The inset shows a typical distribution of AlAs over the thickness of the structure.

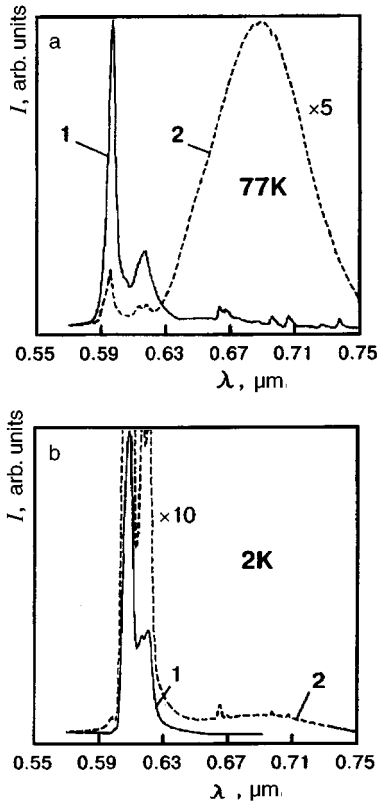

FIG. 2. Photoluminescence spectra of a sample with $x_{buff}=0.5$ recorded at $T = 77$ K and $T = 2$ K: *1* — initial spectra, *2* — modified spectra.

direct radiative transitions in the indirect-gap material from the Γ minimum of the conduction band and of indirect radiative transitions from the X minimum of the conduction band could also be detected in the spectrum. For example, for the sample with $x_{buff} = 0.65$ these are the peaks at $\lambda_{max}=0.584\mu$m and $\lambda_{max}=0.607\mu$m, respectively (Fig. 1).

The most interesting effects in the photoluminescence spectra were observed for the second group of samples with a value of x near the minimum for which the composition dependences of the direct and indirect band gaps ($E_g^{\Gamma}(x)$ and $E_g^{x}(x)$, respectively) intersect. A typical photoluminescence spectrum of this type of sample with $x_{buff}=0.5$ recorded at a pump power density of ~ 50 W/cm^2 is plotted in Fig. 1. The photoluminescence spectrum of this sample is shown in greater detail in Fig. 2. It can be seen from Fig. 2 that the spectrum consists of a group of high-intensity peaks near $\lambda\sim 0.61\mu$m. A similar spectral structure was observed in Ref. 4 for $Al_xGa_{1-x}As$ layers grown by vapor-phase epitaxy from metalorganic compounds and was interpreted as bound exciton photoluminescence (in Fig. 2b, $\lambda_{b.ex.}=0.597\mu$m) and several phonon replicas. These spectra are characteristic of high-quality layers.

An interesting feature of this second group of samples was an irreversible change in their photoluminescence characteristics when the pump density was increased to 1 kW/cm^2 at 77 K. Figure 2 also shows the photoluminescence spectrum of a sample after exposure to this ''laser annealing.'' The spectrum was modified by an abrupt drop (approximately twentyfold) in the intensity of the exciton line and the photon replicas near $\lambda\sim 0.61\mu$m, and by the appearance of a broad band ($\Delta h\nu\sim 200$ meV) at $\lambda_{max}\sim 0.69\mu$m. However, when the sample temperature was reduced to 2 K, the exciton line again dominated in the photoluminescence spectra (Fig. 2b). At the same time, laser annealing of the samples at the same pump power densities at room temperature did not cause any significant changes to their photoluminescence characteristics. Possible mechanisms for this behavior at 77 K were examined by us in Ref. 5 and were attributed to the optically induced annealing of defects and also to a recombination-generation process of impurity diffusion with the formation of an arsenic vacancy (V_{As})-donor impurity complex.

To summarize, an investigation of the photoluminescence characteristics of epitaxial layers obtained under conditions of ultrafast cooling of the flux has indicated that these layers are of high quality.

It has also been observed that when samples with $x_{buff} = 0.5$–0.55, i.e., with x_{min} near the minimum close to the direct–indirect band gap transition, are exposed to laser radiation with a power density of ~ 1 kW/cm^2 at 77 K, the spectral composition of the radiation undergoes irreversible changes associated with the formation of an arsenic vacancy (V_{As})–donor impurity complex.

This work was supported financially by the Russian Fund for Fundamental Research, under Project No. 96-02-17864a.

[1] A. V. Abramov, N. G. Deryagin, and D. N. Tret'yakov, Semicond. Sci. Technol. **11**, 607 (1996)
[2] A. V. Abramov, B. Ya. Ber, N. G. Deryagin, A. V. Merkulov, and D. N.

Tret'yakov, Pis'ma Zh. Tekh. Fiz. **21**(3), 34 (1995) [Tech. Phys. Lett. **21**, 103 (1995)].
[3] K. H. Chang, C. P. Lee, J. S. Wu, D. G. Liu, D. C. Liou, M. H. Wang, L. J. Chen, and M. A. Marais, J. Appl. Phys. **70**, 4877 (1991).
[4] T. F. Kuech, D. J. Wolford, R. Potemski, J. A. Bradley, K. H. Kelleher, D. Yan, J. P. Farrell, P. M. S. Lesser, and F. H. Pollak, Appl. Phys. Lett. **51**, 505 (1987).
[5] A. V. Abramov, A. G. Deryagin, N. G. Deryagin, V. I. Kuchinskii, M. N. Sobolev, and M. I. Papensev, Mater. Sci. Forum **196–201**, 1437 (1995).

Translated by R. M. Durham

Dynamics of field dislocations and disclinations in a few-mode optical fiber. III. Circularly polarized CP_{11} modes and *L* disclinations

A. V. Volyar, T. A. Fadeeva, and Kh. M. Reshitova

Simferopol State University
(Submitted November 11, 1996)
Pis'ma Zh. Tekh. Fiz. **23**, 14–20 (March 12, 1997)

It has been found experimentally and theoretically that when a stepped-index few-mode optical fiber is excited by a circularly polarized Gaussian beam, linearly polarized pure edge L_x and L_y disclinations are generated in the guided wave fields. The azimuths of the linear polarization of these disclinations rotate in the direction opposite to the rotation of the disclination axes. When the axes of the L_x and L_y disclinations are mutually orthogonal, a pure screw dislocation is created. When the axes are collinear, the $L_x$and L_y disclinations annihilate and a pure uniform circularly polarized edge dislocation is generated, its axis coinciding with the axis of the disclinations. Reversal of the circular polarization of the excitation changes the sign of the angles of orientation of the pure edge dislocations and disclinations, and also reverses the azimuth of the linear polarization and reverses the sign of the topological charge of the pure screw dislocation. The physical mechanism for the rotation of the disclination and dislocation axes is attributed to the optical Magnus effect in a few-mode fiber. The rotation of the plane of polarization of the L_x and L_y disclinations and the screw dislocation reflects the appearance of the Berry topological phase accompanied by a cyclic change in the orientation of these disclination axes.
[S1063-7850(97)00303-0]

The formation of optical vortices in a few-mode fiber is directly related to the excitation of circularly polarized fields. Known simple wave combinations are linearly polarized (the LP_{11} modes) (Ref 1). Thus the fields of the LP_{11} modes must be combined with the orthogonal linear polarizations to describe the excitation of circularly polarized fields at the entrance to a fiber. This wave combination will subsequently be called the circularly polarized CP_{11} mode.

It was shown in the first part of this work that any change in the field of the LP_{11} mode is determined by the interaction of the perturbation fields of orthogonal pure edge circular $C^{\pm}$ disclinations. The formation of CP_{11} modes from two LP_{11} modes can now be described by four $C^{\pm}$ disclinations. Summation of these disclinations creates new types of vector wave defects. The evolution of these new vector defects or disclinations will characterize the wave changes of the CP_{11} modes propagating in an inhomogeneous medium.

The aim of the present study is to make an experimental and theoretical investigation of the properties of vector defects — disclinations — in the CP_{11} modes of a few-mode fiber.

1. Let us analyze the optical field of a few-mode fiber which is uniformly circularly polarized at the entrance. From the four possible types of LP_{11} modes we can construct four types of CP_{11} modes of different parity and direction of circulation. Without loss of generality, we shall select the even right-circularly polarized $CP_{11}^{+e\nu}$ mode for our analysis. The field of this mode, being the result of the summation of two orthogonally polarized LP_{11} modes, may be expressed in the form:

$$e_t=[\hat{e}^+(\cos(\varphi-\delta\beta_{21}z)+\cos[\varphi-(\Delta\beta+\delta\beta_{21})z]\exp\{i\Delta\beta z\})+\hat{e}^-(\cos(\varphi+\delta\beta_{21}z)-\cos[\varphi+(\Delta\beta+\delta\beta_{21})z]\exp\{i\Delta\beta z\})]F_1\exp\{i\beta z\}, \quad (1)$$

where

$$\delta\beta_{21}=\frac{\delta\beta_2-\delta\beta_1}{2}; \quad \widetilde{\beta}_1=\widetilde{\beta}+\frac{\delta\beta_2-\delta\beta_1}{2};$$

$$\Delta\beta=\delta\beta_4-\delta\beta_2, \quad (2)$$

$\hat{e}^+$ and $\hat{e}^-$ are the unit vectors of the circular polarization, $\delta\beta_i$ are the polarization corrections of the HE_{21} $(i=1)$, TM_{01} $(i=2)$, and TE_{01} $(i=4)$ modes. For a graded-index fiber in the first approximation of perturbation theory[1] we have $\delta\beta_2=\delta\beta_4=0$ and from Eq. (1): $e_t=\hat{e}^+\times\cos(\varphi-\delta\beta_{21})F_1(R)$.

A uniformly circularly polarized $CP_{11}^{+e\nu}$ mode with a pure edge dislocation is formed in a fiber having a parabolic refractive index profile and propagates without any change in polarization state or type of dislocation. The axis of this dislocation is rotated through the angle $\gamma=\delta\beta_{21}z$ in the cross section $z=z_0$. If a graded-index fiber is excited by left-circularly polarized light, a uniformly left-circularly polarized wave field with a pure edge dislocation will propagate in the fiber. The axis of the dislocation is rotated through the angle $\gamma=-\delta\beta_{21}z$ in the cross section $z=z_0$. This process is due to the simultaneous creation of four circularly polarized pure $C^{\pm}$ edge disclinations in two orthogonal LP_{11} modes. These disclinations rotate at the same angular velocities but the pair of C^- disclinations are in antiphase and cancel out,

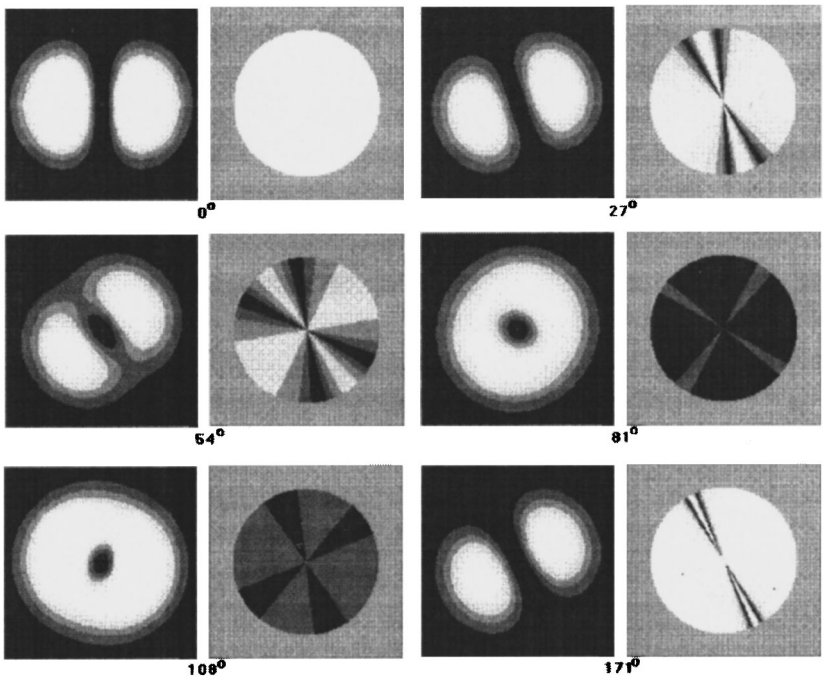

FIG. 1. Distribution patterns of the intensity I (left) and the degree of linear polarization η (right) of the field of the circularly polarized CP_{11} mode. The distributions $I(\rho,\varphi)$ and $\eta(\rho,\varphi)$ correspond to the fiber cross sections $\Delta\beta z_0$ in the phase interval between 0 and π. The white on the $\eta(\rho,\varphi)$ patterns indicates circular polarization and black indicates linear polarization.

forming a pure rotating edge dislocation. The other pair of C^+ disclinations are in phase and amplify each other by interference.

In a stepped-index fiber the polarization corrections $\delta\beta_2$ and $\delta\beta_4$ for the TE_{01} and TM_{01} modes in the LP_{11} group differ and the dynamics of the dislocations and disclinations is described by expression (1). Figure 1 shows field patterns for the intensity and polarization states of the CP_{11} mode. In this field combination the terms $C^{\pm}$ disclinations cannot be used, since the fiber field is only circularly polarized in the planes where $\Delta\beta z = m\pi$ ($m=0, 1, 2\ldots$). In the other cross sections the light does not become circularly polarized for any azimuthal angles φ. Thus for the calculations we used the term, the degree of linear polarization, which is defined as $\eta=(1-|Q|)/(1+|Q|)$, where Q is the eccentricity. It can be seen from Fig. 1 that linearly polarized lines appear on the pattern of polarization states of the field cross section. These lines are linearly polarized at their instant of creation, one along y and the other along x, but as they propagate, they rotate at different angular velocities. The directions of linear polarization of these lines also rotate but in the opposite direction. We called these lines pure L_x and L_y edge disclinations by analogy with the disclinations of the fields in free space[2,3] since for L_x the electric field is $\mathrm{Im}[e_y(z=0)]=0$, $\mathrm{Re}[e_y(z=0)]=0$ and for L_y it is $\mathrm{Im}[e_x(z=0)]=0$, $\mathrm{Re}[e_x(z=0)]=0$.

In Fig. 2b the solid curves giving the degree of linear polarization η as a function of the azimuthal coordinate φ describe the theoretically calculated evolution of the polarization state of the CP_{11}^{+ev} mode. The motion of the peaks of these curves reflects the dynamics of the L_x and L_y disclinations. It can be seen from Fig. 1 and Fig. 2b that for $\Delta\beta z=\pi/2+m\pi$, where the axes of the L_x and L_y disclinations are orthogonal, a pure screw dislocation is generated with the topological charge $l=+1$, its field being uniformly linearly polarized with the vector e having the azimuth $\psi=-\delta\beta_{21}z$. If the fiber is excited by left circularly polarized light, a pure screw dislocation is created with $l=-1$ and its linear polarization is oriented at an angle $\psi=+\delta\beta_{21}z$. When $\Delta\beta z=m\pi$, the axes of the L_x and L_y disclinations are parallel and a pure edge dislocation is created with its axis oriented at the angle $\gamma=\delta\beta_{21}z$ (this coincides with the dislocation axis of an equivalent graded-index waveguide). Reversal of the circular polarization of the exciting beam changes the sign of the angle γ. Figure 2a shows a phase portrait of the evolution of the $L_x$and L_y disclinations (by analogy with the phase portraits of the $C^{\pm}$ disclinations in the first part of this work). The phase curves were obtained from expression (1) and the condition that the third Stokes parameter is $S_3=i(E_xE_y^*-E_x^*E_y)=0$ for the linearly polarized L_x and L_y disclinations. The intersections of the spiral curves correspond to the creation of linearly polarized pure screw dislocations with the topological charge $l=+1$. The joining points of the solid and dashed curves correspond to the creation of circularly polarized pure edge dislocations.

2. An experimental investigation was made of the degree of linear polarization η as a function of the azimuthal angle φ in a few-mode fiber for various sections of length z. The measurements were made using an experimental setup and a few-mode fiber whose parameters were described in the first part of this work. The CP_{11}^{+ev} mode was formed at the entrance to the fiber by passing a Gaussian beam through the hologram of an edge dislocation and a quarter-wave plate. The results of the measurements given by the experimental points in Fig. 2 show that excitation of a few-mode fiber by circularly polarized light is associated with the creation of two linearly polarized disclinations rotating in the same direction at different angular velocities. The angles of orientation of the linear polarizations rotate in opposite directions to the rotation of the disclinations. It was found experimentally that uniform linear polarization is observed at the length

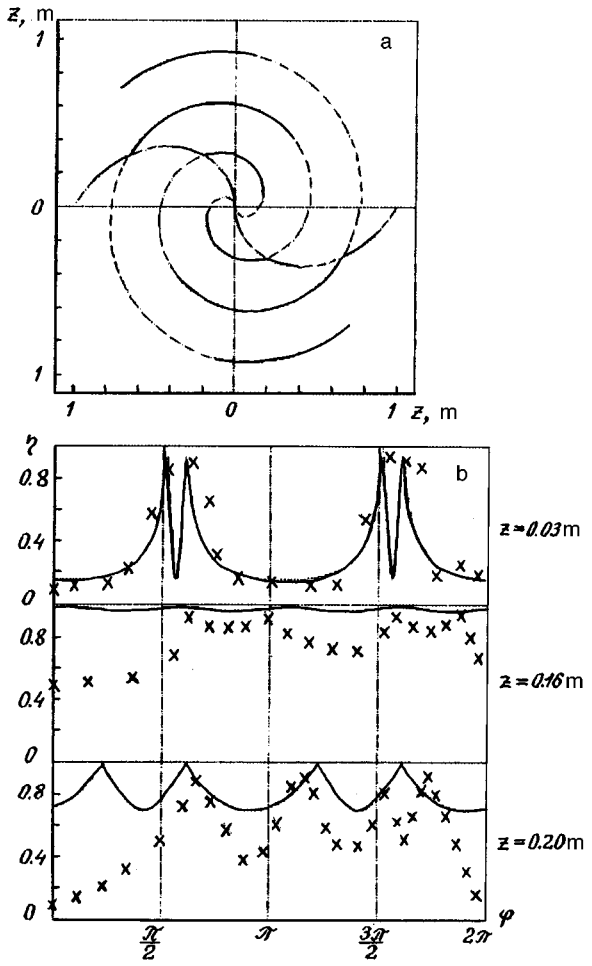

FIG. 2. a — Phase portrait of the evolution of L_x and L_y disclinations plotted in polar coordinates. The fiber length z is taken as the polar radius and the angle φ characterizes the azimuth of the edge disclination axis. The solid curve corresponds to the L_y disclination and the dashed curve to the L_x disclination; b — degree of linear polarization η versus azimuthal coordinate φ for various fiber lengths and the phase $\Phi=\Delta\beta z$. The solid curves give the theory and the crosses give the experimental values.

$s_0=18$ cm, which is approximately a quarter of the beat length $\Lambda_0=2\pi/\Delta\beta$. However, the azimuths of the linear polarizations of the L_x and L_y disclinations could not be constructed for fiber lengths of the order of 4 m. This is because four natural modes whose propagation constants β_i are irrational numbers participate in the formation of the L_x and L_y disclinations.[4]

It was found that no cross-sectionally uniform circular polarization orthogonal to the initial polarization state is observed in the emission of the CP_{11}^{+ev} mode. In addition, the charge of the screw dislocations at the $(2m+1)\Lambda_0/4$ cross sections does not change sign during evolution of the field.

An interference experiment showed that in the fiber cross sections $z=(2m+1)\pi/4\Delta\beta$ pure edge dislocations are formed whose topological charge changes sign when the circulation of the exciting-beam polarization is reversed.

The physical mechanism for rotation of the axis of an edge disclination is explained by the optical Magnus effect[5] for few-mode fibers. The rotation of the plane of linear polarization of the L_x and L_y disclinations is attributed to the Berry topological phase accompanied by a cyclic change in the direction of the disclination axis.

This work was partially supported by the International Soros Program for promotion of education in the exact sciences (ISSEP), Grant N PSU062108.

[1] A. W. Snyder and J. D. Love, *Optical Waveguide Theory* (Methuen, London, 1984) [Russ. transl., Radio i Svyaz, Moscow, 1987].
[2] J. F. Nye, Proc. R. Soc. London A **387**, 105 (1983).
[3] J. V. Hajnal, Proc. R. Soc. London A **414**, 447 (1987).
[4] A. V. Volyar, S. N. Lapaeva, and É. A. Modnikova, Pis'ma Zh. Tekh. Fiz. **20**(7), 6 (1994) [Tech. Phys. Lett. **20**, 261 (1994)].
[5] A. V. Volyar and S. N. Lapaeva, Pis'ma Zh. Tekh. Fiz. **18**(8), 53 (1992) [Tech. Phys. Lett. **18**, 261 (1992)].

Translated by R. M. Durham

Atomic distribution function of macroscopically isotropic objects in diffraction analyses

N. I. Gulivets, A. V. Bobyl', A. I. Dedoborets, and B. I. Peleshenko

Scientific-Industrial Organization, St. Petersburg State University
(Submitted December 4, 1996)
Pis'ma Zh. Tekh. Fiz. **23**, 21–26 (March 12, 1997)

When the atomic distribution function is determined by regularization of the Tikhonov equation in diffraction analyses of macroscopically isotropic objects, the introduction of a weighting function can significantly reduce the oscillating component associated with the measurement error and the existence of an upper limit on the wave vector fluctuations. The proposed procedure is demonstrated for the diffraction analyses of metallic melts. © *1997 American Institute of Physics.* [S1063-7850(97)00403-5]

A so-called structure factor $a(s)$, where s is the modulus of the change in the wave vector accompanying scattering, is widely used in various types of diffraction analysis (*x*-ray, electron, and neutron diffraction analysis). The basic equation used to study the atomic structure of macroscopically isotropic objects[1] is usually written as

$$a(s)=1+s^{-1}\int_0^\infty 4\pi r(\rho(r)-\rho_0)\sin sr\ dr, \tag{1}$$

where ρ_0 is the average atomic density of the sample and $\rho(r)$ is the atomic density at the distance r from an arbitrarily selected atom. Relation (1) can be used to obtain the difference radial atomic distribution function

$$\varphi(r)\equiv 4\pi r(\rho(r)-\rho_0)=\frac{2}{\pi}\int_\pi^\infty s(a(s)-1)\sin sr\ ds. \tag{2}$$

Since the measurements of the scattering intensity contain some error and are performed up to some upper value of the modulus s_m, the dependence $\varphi(r)$ contains oscillating errors, which are particularly appreciable for small r (Refs. 2–6).

In the present paper the function $\varphi(r)$ is obtained by transforming Eq. (1) using a weighting function in the residual of the Tikhonov smoothing functional.[7,8] By variation of its parameter, this function is used to obtain the kernel of the Tikhonov equation in the form of an exponential function from the smoothing functional. The proposed procedure is demonstrated for the diffraction analysis of metallic melts.

We transform Eq. (1) to give

$$\int_0^\infty \varphi(r)\sin sr\ dr=j(s), \tag{3}$$

where $j(s)\equiv s(a(s)-1)$ and we construct the zeroth-order Tikhonov functional

$$Q=\int_0^{s_m}B^2(s)\left(\int_0^\infty \varphi(x)\sin sx\ dx-j(s)\right)^2 ds + \alpha\int_0^\infty \rho(r)\varphi^2(r)dr, \tag{4}$$

where $B(s)$ is a positive monotonically decreasing function on $[0,s_m]$ and α is the regularization constant. Variation of Q with respect to $\varphi(x)$ reduces the problem to the following Tikhonov equation:

$$\int_0^\infty \varphi(x)dx\int_0^{s_m}B(s)\sin sx\sin sr\ ds+\alpha\rho(r)\varphi(r) =\int_0^{s_m}B(s)j(s)\sin sr\ ds. \tag{5}$$

For $B(s)\equiv 1$, Eq. (5) yields

$$\int_{-\infty}^\infty \varphi(x)\frac{\sin s_m(r-x)}{\pi(r-x)}dx+\frac{2\alpha}{\pi}\rho(r)\varphi(r) =\frac{2}{\pi}\int_0^{s_m}j(s)\sin sr\ ds. \tag{6}$$

The right-hand side of Eq. (6) is frequently considered to be equal to the unknown function $\varphi(r)$, which is obviously satisfied provided there is no experimental error and $s_m\to\infty$.

We shall take the function $B(s)$ in the form

$$B(s)=\exp(-\beta s^2/2),\quad 0>s>s_m \tag{7}$$

and we shall assume that the error of the approximation

$$\int_0^{s_m}\exp(-\beta s^2)\cos sx\ ds\approx k\left(\frac{\pi}{4\beta}\right)^{1/2}\exp\left(-\frac{x^2}{4\beta}\right) \tag{8}$$

is no greater than the experimental error for given k close to unity. In addition, apart from $\delta>0$, the following condition is satisfied for the function (7)

$$\left\{\int_0^{s_m}\left(\exp\left(\frac{\beta s}{2}\right)j(s)-j(s)\right)^2 dx\right\}^{1/2}>\delta, \tag{9}$$

which ensures that the experimental values of the structure factor are moderately distorted (blurred). The value of the parameter β is selected as follows. First we determine the highest value of β satisfying condition (9) and then we verify condition (8) for $k=1$. If necessary, we decrease k so as to satisfy condition (8). It was calculated that the value of β satisfying condition (8) for $k=1$ and the required error δ is $\sim 2\pi/s_m^2$.

Then we obtain from Eq. (5)

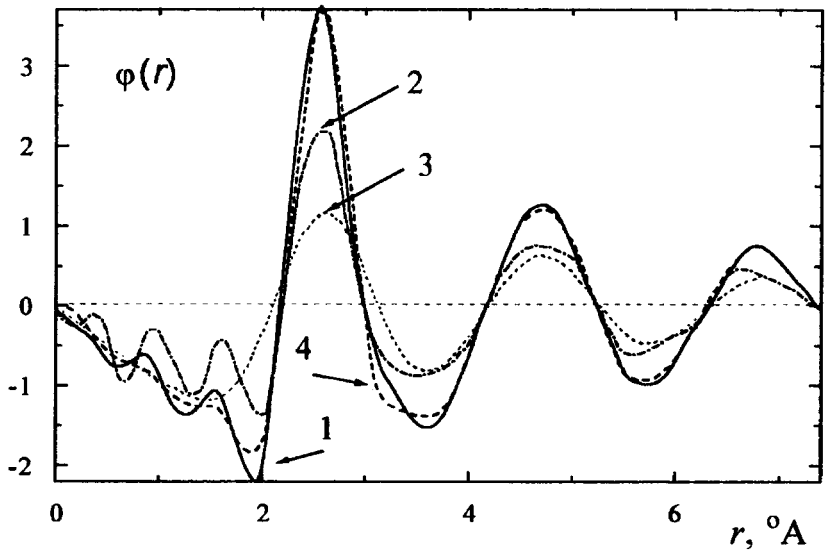

FIG. 1. Difference atomic distribution function of Cu melt at 1393 K: *1, 2* — right-hand side and solution of Eq. (6); *3, 4* — right-hand side and solution of Eq. (10), respectively.

$$(4\pi\beta)^{-1/2}\int_{-\infty}^{\infty}\varphi(x)\exp\left(-\frac{(r-x)^2}{4\beta}\right)dx+\frac{2\alpha}{\pi}\rho(r)\varphi(r)$$

$$=\frac{2}{\pi}\int_0^{s_m}e^{-\beta s^2}j(s)\sin sr\,ds. \qquad (10)$$

The right-hand side of Eq. (10) differs from that of Eq. (6) in that its extrema are broader, although their position and the area below the curves are the same.

The most efficient method of solving Eqs. (6) and (10) for $\varphi(r)$ is to solve the appropriate systems of linear equations. In this case, the problem reduces to solving the system of equations for $\varphi(r)$ at the quadrature points and then interpolating the values obtained.[9] The matrix of the system of equations to solve Eq. (10) is simpler than that for Eq. (6). It is a band matrix, and experience shows that several tens of solutions of the system is sufficient to find the regularization constant, which is fairly economical on computing time.

The proposed procedure can be demonstrated for the diffraction analyses of the structure factor of a copper melt at $T = 1393$ K (Ref. 3). Figure 1 shows graphs of the right-hand sides of Eqs. (6) and (10) calculated using the results of Ref. 3 and also the corresponding solutions for $\varphi(r)$. Equation (10) was solved using the value $\beta=0.08$ Å^{-2}, which provided the required accuracy. The criterion for optimization of the regularization constant α was taken as[9]

$$\left\|\alpha\frac{d\varphi_\alpha}{d\alpha}\right\|=\min_{\alpha>0}. \qquad (11)$$

According to Eq. (11), the optimum regularization constant to solve Eq. (6) is $\alpha_{\rm opt}=0.49$ whereas to solve Eq. (10) for the given value of β the optimum regularization constant is $\alpha_{\rm opt}=0.007$. This low value indicates that the introduction of the weighting function (because of its shorter-range kernel) additionally regularizes the Tikhonov equation (5), whereas the kernel in Eq. (6) is a peak with oscillating slowly decaying wings.

A comparison of the curves plotted in Fig. 1 indicates that although $\varphi(r)$ obtained by solving Eq. (10) is close to the values of the right-hand side of Eq. (6), appreciable deviations are observed on the leading edge of the first peak (for small r) as well as less significant deviations for other values of r. These deviations are caused by the right-hand side of Eq. (6) differing from the true function $\varphi(r)$ since the former is a convolution with an approximate form of the Dirac δ-function (i.e., with the function $\sin(s_m r)/(\pi r)$). As was noted, the result of this convolution is especially noticeable on the wings of the principal peak of the right-hand side of Eq. (6), where appreciable oscillations are observed and it is thus preferable to use the solution of Eq. (10). Another factor is that the oscillating component increases appreciably in the solutions of Eqs. (6) and (10) for $\alpha=0$, i.e., in the absence of regularization, but for the solution of Eq. (6) this component is fairly large even for optimum values of α for Eq. (10). A similar situation is encountered in the diffraction analyses of other macroscopic isotropic objects.

Thus, when determining the atomic distribution function by regularization of the Tikhonov equation in diffraction analyses of macroscopically isotropic objects, the introduction of a weighting function can significantly reduce the oscillating component associated with the measurement error and the existence of an upper limit for the wave vector fluctuations. Without this weighting function the procedure leads to broadening of the peaks of the atomic distribution function.

The authors would like to thank S. G. Konnikov, R. N. Kyutt, and R. A. Suris for useful comments. This work was supported by the Russian Fund for Fundamental Research, Project No. 18563.

[1] *Physics of Simple Liquids*, edited by H. N. V. Temperley, J. S. Rowlinson, and G. S. Rushbrooke (North-Holland, Amsterdam, 1968) [Russ. transl., Mir, Moscow 1971]
[2] E. Lorch, J. Phys. C **2**, 229 (1969).
[3] O. J. Eder, E. Erdpresser, B. Kunsch *et al.*, J. Phys. E **10**, 183 (1980).
[4] S. Hosokawa, T. Matsuoka, and K. Tamura, J. Phys.: Condens. Mater. **3**, 4443 (1991).
[5] V. É. Sokol'skiĭ, V. P. Kazimirov, and V. A. Shovskiĭ, Kristallografiya **40**, 989 (1995) [Crystallogr. Rep. **40**, 915 (1995)]

[6] J. H. Lee, A. P. Owens, A. Pradel *et al.*, Phys. Rev. B **54**, 3895 (1996).
[7] A. N. Tikhonov and V. Ya. Arsenin, *Solutions of Ill-Posed Problems*, transl of 1st Russ. ed (Halsted Press, New York, 1977) [Russ. original, 2nd ed., Nauka, Moscow, 1979].
[8] A. N. Tikhonov, A. S. Leonov, and A. G. Yagola, *Nonlinear Ill-Posed Problems* [in Russian], Nauka, Moscow (1995).
[9] A. F. Verlan' and V. S. Sizikov, *Integral Equations* [in Russian], Naukova Dumka, Kiev (1986).

Translated by R. M. Durham

Influence of the purity of the starting materials on the recording of dynamic holograms in $Bi_{12}TiO_{20}$ crystals

Yu. B. Afanas'ev, E. V. Mokrushina, A. A. Nechitaĭlov, and V. V. Prokof'ev

A. F. Ioffe Physicotechnical Institute, Russian Academy of Sciences, St. Petersburg; University of Joensuu, P.O. Box 111, SF-80101, Joensuu, Finland
(Submitted November 27, 1996)
Pis'ma Zh. Tekh. Fiz. **23**, 27–32 (March 12, 1997)

The parameters of $Bi_{12}TiO_{20}$ crystals grown with bismuth oxide of different degrees of purity were measured by a holographic recording technique in an external ac electric field and were compared with a crystal specially doped with chromium. Various crystal parameters such as the diffusion length of the photoexcited carriers and the Debye screening length were determined. It was found that the absorption spectrum of the material and the holographic recording efficiency were strongly influenced by light chromium doping and by insufficient purity of the starting mixture. © *1997 American Institute of Physics.* [S1063-7850(97)00503-X]

Piezoelectric crystals with the sillenite structure exhibit electrooptic coefficients considerably inferior to those of ferroelectric photorefractive materials but may have comparable two-wave mixing efficiency. This circumstance arises from the relatively long mean free path of the photoexcited carriers, which means that holograms can be recorded efficiently in an external ac electric field.[1] In this case, the field of the recorded grating depends strongly on the material parameters such as the diffusion length of the free carriers (L_d) and the Debye screening length (L_D), so that these parameters can be determined very accurately by a holographic technique. It was shown in Ref. 2 that even a small impurity content (less than 0.001 wt.%) originating from the inadequate purity of the starting mix ture strongly influences the holographic recording efficiency in a $Bi_{12}TiO_{20}$ (BTO) crystal because of the reduced diffusion length L_d. An investigation of sillenites lightly doped with chromium revealed that in all cases, a negligible ($\sim$0.0001 wt.%) chromium content in the starting mizture reduces the diffusion length of the photoexcited carriers, but the effect of this impurity differs very substantially for BTO and $Bi_{12}SiO_{20}$ (BSO) crystals. In BTO the two-wave mixing efficiency was reduced sharply whereas in BSO, it was increased slightly because of a decrease in the Debye screening length.[3]

In the present paper we compare how the properties of BTO crystals are influenced by different degrees of purity of the initial bismuth oxide and by light doping with chromium atoms. The parameters of the materials were determined as in Ref. 3 by measurements of the spatial-frequency dependences of the two-wave mixing efficiency. The samples were illuminated by an interference pattern formed by two (signal and reference) coherent light beams at 0.63 μm. The optical intensity at the surface of the crystal varied between 3 and 30 mW/cm^2. The ratio of the signal and reference beam intensities was around 0.01. A square-wave ac electric field with a period $\tau = 160$ ms and amplitude up to 6 kV was applied to the sample in the direction of the grating vector. The plane of polarization of the recording beams was oriented at an angle of 45° to the plane of incidence. In this case a volume refractive index grating was recorded in the sample and the intensity of the optical beams varied as a result of self-diffraction (two-wave mixing).

It is known[1] that in this case (subject to the condition $\tau \ll \tau_{\sim} \ll \tau_{cs}$, where τ is the lifetime of the photoinduced carriers and τ_{cs} is the characteristic grating recording time), the two-wave gain factor is given by

$$\Gamma = \frac{\pi}{U_{\lambda/2}} \cdot \frac{E_d}{K^2 L_D^2} \cdot \frac{1 + Q_d (E/E_d)^2}{1 + Q_D (E/E_d)^2}, \tag{1}$$

where $E_d = K(kT/e)$ is the diffusion field, K is the modulus of the wave vector of the grating, k is the Boltzmann constant, T is the absolute temperature, e is the electron charge, $Q_{d,D} = K^2 L_{d,D}^2/(1 + K^2 L_{d,D}^2)$, and $U_{\lambda/2}$ is the half-wave voltage of the material.

The dependence of the grating amplitude on the spatial frequency determined by expression (2) has a maximum at $K = K_{\max}$ and its form depends on the values of L_d and L_D, where to a first approximation the diffusion length determines the growth rate of $E_{cs}(K)$ at low spatial frequencies while the screening length determines the rate of decay for $K > K_{\max}$. These characteristics allow us to determine the diffusion and Debye lengths by measuring $\Gamma(K)$ and using these values as fitting parameters.

The BTO crystals were grown by the Czochralski method from a high-temperature nonstoichiometric (10:1) Bi_2O_3:TiO_2 melt at the A. F. Ioffe Physicotechnical Institute of the Russian Academy of Sciences. The samples were cut in standard geometry: the polished faces were parallel to the $\langle \underline{1}10 \rangle$ plane and an ac electric field was applied along the [110] axis. The thickness of the samples and the average distance between the electrodes were 6 mm and 4 mm, respectively.

Four BTO single crystals were grown using starting materials of different degrees of purity. Crystals BTO 1, BTO 2, and BTO 3 were prepared using extra pure, analytical grade, and pure bismuth oxide, respectively. Crystal BTO 4 was grown from extra pure bismuth oxide to which 0.001 wt.% Cr_2O_3 was added. The chromium concentration in the starting material and in the as-grown crystals was determined by

TABLE I. Crystal parameters.

	Grade of bismuth oxide	Chromium content, wt.% Initial mixture	Crystal	Diffusion length, μm	Debye screening length, μm
BTO 1	extra pure	$<5\times10^{-5}$	$<5\times10^{-5}$	0.25	0.10
BTO 2	analytic grade	1.1×10^{-4}	1.0×10^{-4}	0.07	0.11
BTO 3	pure	3.2×10^{-4}	3.0×10^{-4}	0.033	0.11
BTO 4	extra pure with 10^{-3} wt.% Cr_2O_3	8.1×10^{-4}	7.6×10^{-4}	0.031	0.15

photometric chemical analysis (the minimum detectable concentration was 5×10^{-5} wt.%) (Ref. 4). The analytical results are presented in Table I.

Figure 1 shows absorption spectra of crystals BTO 1 through BTO 4 measured with an SF-8 spectrophotometer. It can be seen that unlike BTO 1, the crystals grown from insufficiently purified materials exhibit strong (650–880 nm) and weaker (880–1060 nm) absorption in the near infrared. At the same time, the addition of 0.001% Cr to the extra pure bismuth oxide yields a similar absorption band profile (BTO 4).

Figure 2 gives the two-wave gain factor as a function of the spatial frequency of the recorded grating. The symbols give the experimental data and the solid curves show the theoretical dependences calculated according to expression (2) using the lengths L_d and L_D as fitting parameters. A comparison of curves *1*, *2*, and *3* obtained for the same fields reveals that the two-wave gain factor depends directly on the purity of the bismuth oxide. A low chromium impurity has a similar effect (crystals BTO 3 and BTO 4 have the same parameters so the curves were obtained for different fields so that the curves did not merge on the figure).

The values obtained for the diffusion length of the photoexcited carriers and the Debye screening length are also given in Table I.

It can be concluded from the data plotted in Figs. 1 and 2 and presented in Table I that even in small quantities, chromium is one of the main impurities strongly influencing the absorption spectrum of BTO crystals. However, it should be noted that crystals BTO 2 and BTO 3 obviously contain other types of impurities which do not have such a strong influence on the absorption spectrum as chromium but do also reduce the diffusion length L_d: the chromium concentration in BTO 3 is 2.5 times lower than that in BTO 4 but the diffusion length is the same in both crystals and is almost an order of magnitude lower than in the pure BTO 1 crystal. It was also established by means of chemical analysis that the iron content in the pure bismuth oxide fluctuates in the range $(1-2)\times10^{-3}$ wt.%, which is almost an order of magnitude higher than its content in the extra pure Bi_2O_3. It may well be that iron, as well as chromium, reduces the diffusion length L_d in crystal BTO 3.

It should be noted that in this case, the Debye screening length, which is inversely proportional to the bulk density of free traps, is almost independent of the impurity content. Thus in insufficiently pure BTO crystals the two-wave gain in an ac field is low (unlike BSO:Cr crystals[3] where both L_d and L_D decrease proportionately); i.e., a low impurity content in a BTO crystal does not influence the trap density but other parameters of the photoinduced carriers (mobility and trapping probability) on which L_d depends.

The following conclusions can therefore be drawn:

- chromium is most likely the main low-concentration impurity (up to 10^{-3} wt.%) influencing the absorption spectrum of BTO crystals;

- specially introduced chromium impurities as well as insufficient purity of the initial mixture give rise to a characteristic absorption band in the near infrared and substantially reduce the diffusion length of the photoinduced carriers, without altering the Debye screening length in BTO crystals;

- in consequence, impurities of low concentration in

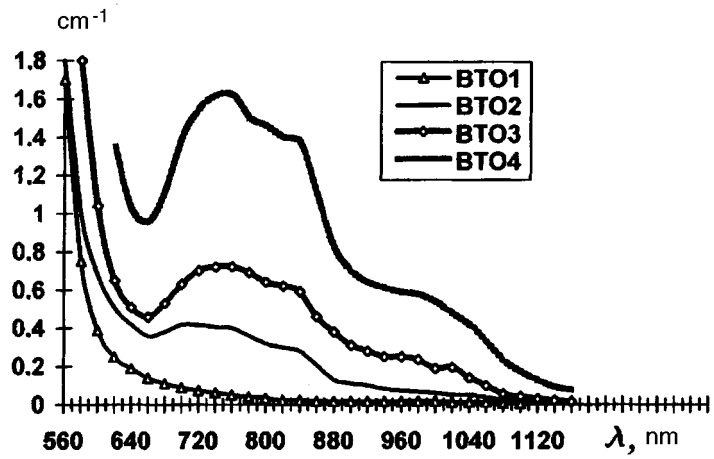

FIG. 1. Absorption spectra of crystals grown with bismuth oxide of different degrees of purity (BTO 1– BTO 3) and also of a crystal specially doped with chromium (BTO 4).

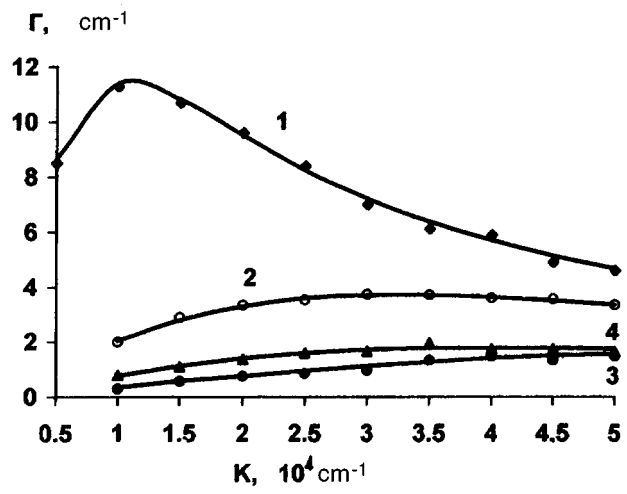

FIG. 2. Two-wave mixing gain factor in an external ac field: curves *1*, *2*, and *3* correspond to crystals BTO 1–BTO 3 with a field $E = 9$ kV/cm, and curve *4* corresponds to crystal BTO 4 with a field of 14 kV/cm.

BTO crystals (unlike BSO) reduce the two-wave mixing efficiency in an ac field.

The nature of the different influence of low-concentration impurities on the properties of BTO and BSO crystals may form the subject of a further study.

The work was partially supported by the Russian Fund for Fundamental Research.

[1] S. I. Stepanov and M. P. Petrov, in *Photorefractive Materials and their Applications*, edited by P. Gunter and J. P. Huignard (Springer-Verlag, London, 1987), Chap. 9.
[2] S. L. Sochava, E. V. Mokrushina, V. V. Prokof'ev, and S. I. Stepanov, J. Opt. Soc. Am. B **10**, 1600 (1993).
[3] E. V. Mokrushina, A. A. Nechitailov, and V. V. Prokofiev, Opt. Commun. **123**, 592 (1996).
[4] A. A. Nechitailov, V. V. Prokof'ev, and M. V. Krasin'kova, Sov. J. Anal. Chem. **940**, 1593 (1985).

Translated by R. M. Durham

Anisotropy of ^{63}Ni diffusion in single-crystal silicon iron in a static magnetic field

A. V. Pokoev and D. I. Stepanov

Samara State University
(Submitted September 27, 1996)
Pis'ma Zh. Tekh. Fiz. **23**, 33–38 (March 12, 1997)

An investigation is made of the influence of a static magnetic field on the diffusion of ^{63}Ni in single-crystal silicon iron. It is established that the diffusion coefficient depends on the annealing temperature, the external magnetic field strength, the direction of the Ni concentration gradient, and the crystallographic orientation of the sample, but does not depend on the direction of the field. © *1997 American Institute of Physics.* [S1063-7850(97)00603-4]

In our view, studies of impurity diffusion in ferromagnetic metals in a static magnetic field are of major interest in connection with the diffusion magnetic anomaly whose principal features were described in a review,[1] and with clarifying the influence of exchange interaction on the diffusion mobility of atoms in ferromagnetic materials. According to existing models, whose development can be traced in Refs. 2–5, the nature of the diffusion magnetic anomaly is related to the magnetic ordering of the ferromagnetic material. An external static magnetic field may alter the degree of magnetic order in the ferromagnetic material and thereby influence the diffusion mobility of the impurities.

Impurity diffusion in ferromagnetic metals such as Fe, Co, and Ni in a static magnetic field has been very little studied. In Ref. 6 we observed that grain-boundary diffusion of ^{63}Ni in polycrystalline Armco iron at 730 °C is slowed in a magnetic field of 399.4 kA/m. In Ref. 7 we reported the first systematic investigations of grain-boundary and bulk diffusion of ^{63}Ni in polycrystalline Armco iron in a static magnetic field of 0-399.4 kA/m at temperatures of 730 °C and 860 °C, which revealed a nonmonotonic dependence of the diffusion parameters on the static magnetic field strength. An analysis of data on Ni impurity diffusion in iron and its diffusion magnetic anomaly, contained in Refs. 1, 8, and 9, and also data on the diffusion of this isotope in a static magnetic field[6,7] reveals that the diffusion coefficients are predominantly measured in coarse-grained polycrystalline iron. In the present study, with a view to eliminating the structurally related factor associated with the presence of grain boundaries in the samples and also to improve experimental accuracy, we have used a radioactive isotope method for the first time to measure the diffusion coefficient of ^{63}Ni in [100] and [110] oriented single-crystal silicon iron (2.4 at.% Si) in a magnetic field.

The samples were prepared by the method described in Ref. 10. The diffusion coefficient was measured by the familiar method of residual activity proposed by P. L. Gruzin.[11] The measurements were made in the temperature range 660–860°, extending into both the ferromagnetic and the paramagnetic states of silicon iron (the Curie point of silicon iron is ~755 °C; Ref. 12), for diffusion times of 0.75–30 h and static magnetic fields of 0–557.04 kA/m. The measurement error for the diffusion coefficient was 6%.

When an external static magnetic field is applied at temperatures below the Curie point, the Arrhenius curves of the diffusion coefficient $\ln D = f(1/T)$ become highly nonlinear and it is no longer meaningful to plot them.

Figure 1 shows field dependences of the relative diffusion coefficient $D_{\rm rel}(H) = D_H / D_{H=0}$, where D_H is the diffusion coefficient of ^{63}Ni in single-crystal silicon iron at fixed temperature and magnetic field strength H, and $D_{H=0}$ is the diffusion coefficient without a magnetic field at the same temperature, for two orientations of the silicon iron single crystals and different temperatures. These field dependences exhibit various characteristic features: in weak static magnetic fields $D_{\rm rel}$ increases with the field but in the range near saturation of the magnetization, $D_{\rm rel}$ decreases, and at $H = 557.04$ kA/m is less than unity (or $D_{\rm rel} < 1$). This agrees with the results of Ref. 7. In intermediate fields $D_{\rm rel}$ has one principal peak and in many cases, unlike diffusion in polycrystalline Armco iron,[7] another small side peak. Note that the average level of $D_{\rm rel}(H)$ values for the [110] orientation under these conditions is 1.5-2 times higher than that for the [100] orientation, i.e., the static magnetic field has a greater influence on the ^{63}Ni impurity diffusion for the [110] orientation.

Measurements were usually made for from two to four samples at each temperature and each fixed value of the magnetic field in order to verify this behavior. The results showed good reproducibility within measurement error.

The influence of the direction of the external static magnetic field on the diffusion of ^{63}Ni was assessed by additional experiments in which the plane of the diffusion front of the samples was placed perpendicular to the magnetic field (the usual measurements) and parallel to it (additional measurements), and also for the forward and reverse directions of the magnetic field. Measurements of the diffusion coefficients made at fixed temperature and field strength showed that within measurement error the ^{63}Ni diffusion coefficients do not depend on the direction of the static magnetic field.

At temperatures above the Curie point the measurements showed that the diffusion coefficient of ^{63}Ni in single-crystal silicon iron for either orientation does not depend on the magnetic field strength and within measurement error is the same as its value without a field: the relative diffusion coefficient of ^{63}Ni under these conditions varied in the range $0.942 \leqslant D_{\rm rel} \leqslant 1.059$.

These results yield the following conclusions. The effect of a magnetic field on ^{63}Ni impurity diffusion in single-crystal silicon iron is determined by the annealing tempera-

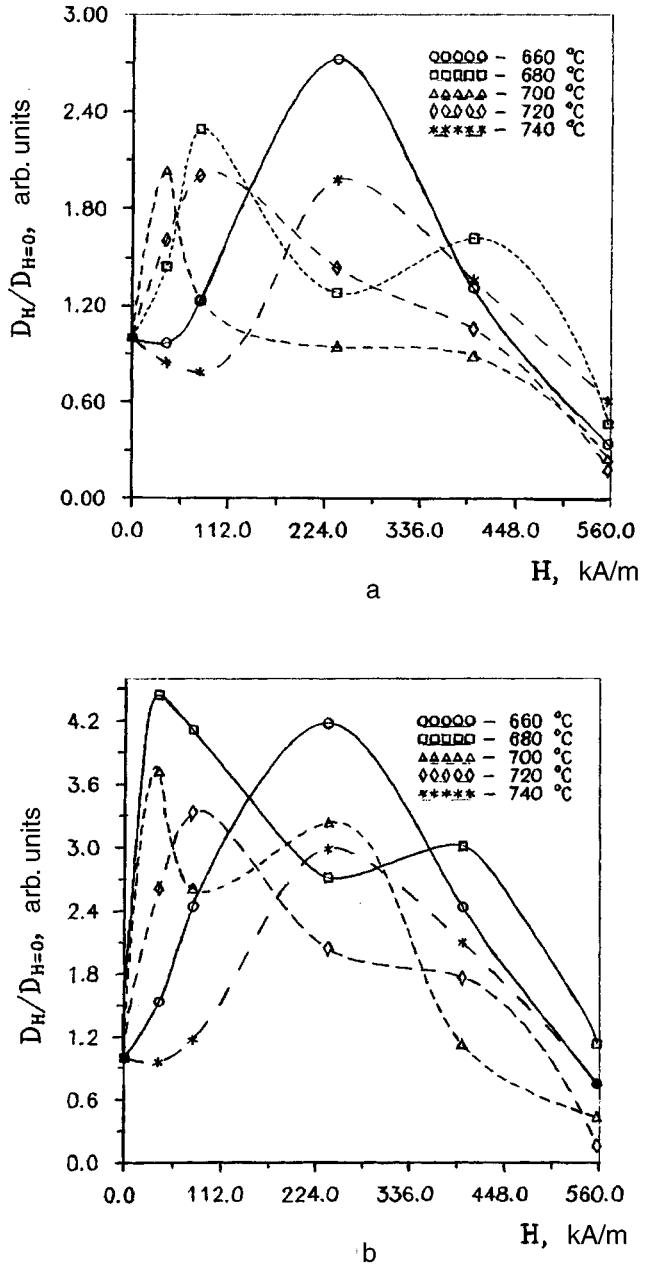

FIG. 1. Field dependences of the relative diffusion coefficient of ^{63}Ni in silicon iron: a — [100] orientation; b — [110] orientation.

ture, the static magnetic field strength, the direction of the Ni concentration gradient, and the crystallographic orientation of the sample, but does not depend on the direction of the external magnetic field. The effect is caused to a considerable extent by a change in the diffusion properties of the medium when the static magnetic field is applied. This supports our previously expressed opinion that a concentration magnetic mechanism is responsible for the diffusion of magnetically active impurities in ferromagnetic materials in the presence of a magnetic field.[13] The use of single crystals in this study allowed us to identify finer details of the behavior of the diffusion coefficient as a function of the field.

Variation of the diffusion coefficient in a static magnetic field may also be caused by changes in the magnetic ordering of the diffusion medium, changes in the defect concentration and their diffusion properties in the diffusion medium in a magnetic field, and by magnetostriction-induced deformations of the matrix and accompanying effects in a static magnetic field. These factors contribute to varying degrees and in different directions depending on the diffusion conditions, which is responsible for the nonmonotonic dependence of the diffusion coefficients on the static magnetic field. At temperatures above the Curie point, where these factors are absent or suppressed in ferromagnetic materials, the magnetic field ceases to influence the measured diffusion coefficient. Before a rigorous systematic analysis can be made of this effect, we need to construct and apply a model of the effective field in a ferromagnetic material which would allow fairly accurately and comprehensively for its temperature dependence, the impurity concentration, and the characteristics of the domain structure of a ferromagnetic material in a static magnetic field at elevated temperatures. Unfortunately no such models exist at present.[14] A detailed analysis of these problems and possible mechanisms for the influence of a static magnetic field on impurity diffusion in silicon iron requires separate consideration which is outside the scope of the present paper.

The authors are grateful to Dr. J. Kučera and Dr. Y. Iijima for kindly supplying reprints of their articles.

[1] J. Kučera and K. Stransky, Mater. Sci. Eng. **52**, 1 (1982).
[2] L. Ruch, D. R. Sain, H. L. Yen, and L. A. Girifalco, J. Phys. Chem. Solids **37**, 649 (1976).
[3] J. Kučera, Czech. J. Phys. **29**, 797 (1979).
[4] K. Hirano and Y Iijima, Defect Diff. Forum **66–69**, 1039 (1989).
[5] G. Hettich, H. Mehrer, and K. Maier, Scripta Metall. **11**, 795 (1977).
[6] A. V. Pokoev, D. I. Stepanov, I. S. Trofimov, and V. I. Mironov, Pis'ma Zh. Tekh. Fiz. **17**(8), 17 (1991) [Sov. Tech. Phys. Lett. **17**, 282 (1991)].
[7] A. V. Pokoev, D. I. Stepanov, I. S. Trofimov *et al.*, Phys. Status Solidi A **137**, K1 (1993).
[8] B. Jönsson, Z. Metallk. **83**, 349 (1992).
[9] K. Hirano, M. Cohen, and B. L. Averbach, Acta Metall. **9**, 440 (1961).
[10] A. V. Pokoev and D. I. Stepanov, Pis'ma Zh. Tekh. Fiz. **22**(6), 28 (1996) [Tech. Phys. Lett. **22**, 238 (1996)].
[11] P. L. Gruzin, Dokl. Akad. Nauk SSSR **86**, 289 (1952).
[12] *Handbook of Tables of Physical Quantities*, edited by I. K. Kikoin [in Russian], Atomizdat, Moscow (1976).
[13] V. M. Mironov and A. V. Pokoev, Defect Diff. Forum **66–69**, 401 (1989).
[14] S. V. Vonsovskiĭ, *Magnetism*, Vols. 1 and 2 (Wiley, New York, 1974) [Russ. original, Nauka, Moscow, 1971].

Translated by R. M. Durham

Deposition of thick $YBa_2Cu_3O_{7-x}$ films on sapphire with a sublayer of cerium oxide

E. K. Hollmann, V. I. Gol'drin, V. E. Loginov, D. A. Plotkin, S. V. Razumov, and A. V. Tumarkin

St. Petersburg State Electrical Engineering University
(Submitted December 6, 1996)
Pis'ma Zh. Tekh. Fiz. **23**, 39–43 (March 12, 1997)

A report is made on the results of experiments to prepare $YBa_2Cu_3O_{7-x}$ films up to 2.6 μm thick on Al_2O_3/CeO_2 with good structural perfection and electrophysical parameters. © *1997 American Institute of Physics.* [S1063-7850(97)00703-9]

Films of the high-temperature superconductor $YBa_2Cu_3O_{7-x}$ (YBCO) offer great promise for applications in microwave technology. However the fabrication of microwave electronics devices (such as filters and phase rotators) requires films of high structural perfection and superior critical parameters, while the film thickness should be greater than the London penetration depth, which increases as the structural perfection of the film deteriorates. According to estimates made in Ref. 1, the minimum thickness of YBCO films for microwave electronics is 0.5 μm. However an increase in thickness leads to the formation of a block structure in which, above a certain thickness, blocks with the crystal c axis perpendicular to the surface ($c_\perp$) are displaced by blocks with the c axis parallel to the surface ($c_\parallel$). Films oriented in the $c_\parallel$ direction have critical parameters inferior to those for films oriented in the $c_\perp$ direction, and the existence of blocks of different orientation leads to anisotropy of the film properties in the plane parallel to the surface and increases the surface resistance. For different substrates and methods of deposition the thickness at which preferentially $c_\perp$-oriented growth is replaced by $c_\parallel$ growth is in the range 0.3–1.5 μm (Refs. 1–3). This transition may be caused by cooling of the film surface as the thickness increases,[1,3] relaxation of mismatch stresses between the film and the substrate,[4] and also by the fact that $c_\parallel$ growth is kinetically preferred. A $c_\parallel$ nucleus generated on the substrate gradually covers the entire surface of the growing film, and at a thickness of $\sim 1\mu$m almost all the film is $c_\parallel$-oriented.[2] A factor common to all experimental observations and proposed approaches is that the concentration of the $c_\parallel$-oriented phase always increases with film thickness.

In the present paper we aim to examine the possibility of obtaining $YBa_2Cu_3O_{7-x}$ films of thickness greater than 0.5 μm with superior electrophysical characteristics and structural perfection, and we shall present results demonstrating the feasibility of obtaining entirely $c_\perp$-oriented films 2.6 μm thick.

The growth of multicomponent oxide films, especially YBCO superconductors, is accompanied by the formation of other compounds as well as the growth of the main phase. These compounds, which for YBCO are dielectric oxides of Y, Ba, and Cu, form island inclusions in the film of deposited material. These dielectric inclusions may well cause no deterioration and may even enhance the superconducting properties of the films,[5] depending on their dielectric properties, size, and concentration. In addition, these dielectric inclusions may have a beneficial effect on the structural perfection of the main phase by acting as sinks for defects and stoichiometrically excess atoms. It was shown in Ref. 6 that at the initial stages of film growth, the concentration of dielectric inclusions varies nonmonotonically in the range between $<10^7$ and 10^9 cm^{-2} and is determined by various deposition conditions.

The YBCO films were deposited on Al_2O_3 $[\bar{1}102]$ substrates with a CeO_2 sublayer of mixed (001)/(111) orientation in a planar dc magnetron in an O_2 (100 Pa) atmosphere.[7] The substrate temperature was maintained around 650 °C and did not increase with increasing film thickness. The discharge current was raised from 100 to 400 mA in the first 30 min and was then maintained at this level. The deposition time was between 5 and 40 h.

The thickness of the films measured with a Dektak-3030 profilometer was 0.29, 0.62, 0.94, 1.3, and 2.6 μm for films grown for 5, 10, 15, 20, and 40 h, respectively. Thus the rate of deposition of the films was estimated as 10.7 Å/min $\pm 5\%$.

The structural perfection of the samples was analyzed by x-ray diffraction analysis (Rigaku Geigerflex series D/max-RC using CuK_α radiation, $\lambda = 1.5418$ Å). The diffraction patterns of all the films indicate a fairly well-ordered $c_\perp$-oriented structure: all $(00l)$ peaks can be seen and the full width at half maximum ($\Delta\omega$) of the rocking curve of the (005) peak is less than 1.1°. Several $(h00)$ peaks are also observed (Fig. 1), which indicates that the film contains grains of the $c_\parallel$-oriented phase.

The relative volume of $c_\parallel$-oriented grains was estimated by a technique proposed in Ref. 1. The intensities of the (005) peak (for $c_\perp$) and (200) peak (for $c_\parallel$), normalized to the corresponding theoretical intensities measured for powder samples, are compared and the results are plotted in Fig. 2. A decrease in the relative intensity of the (200) peak with film thickness may be interpreted as a reduction in the relative volume of $c_\parallel$-oriented inclusions. It can be seen from the variation of the full width at half-maximum of the (005) peak (Fig. 2) that as the volume of $c_\parallel$-oriented inclusions decreases, the crystalline perfection of the $c_\perp$-oriented phase improves and for a film 2.6 μm thick the full width at half-maximum of the (005) peak is 0.47° with no $c_\parallel$-oriented inclusions.

It may be postulated that the relative volume of the $c_\parallel$-oriented phase decreases with film thickness (until it disappears entirely at 2.6 μm) because the growth of the film is

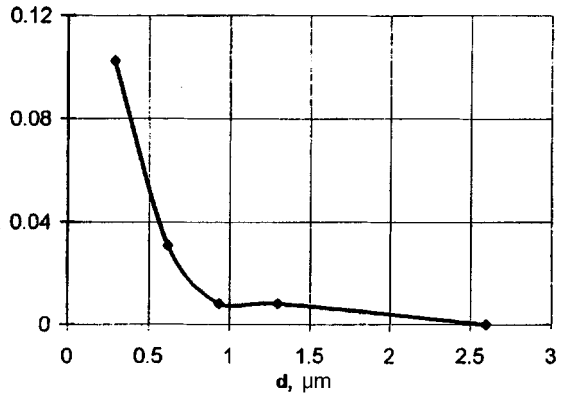

FIG. 1. Relative volume of $c_{\parallel}$-oriented phase versus film thickness d.

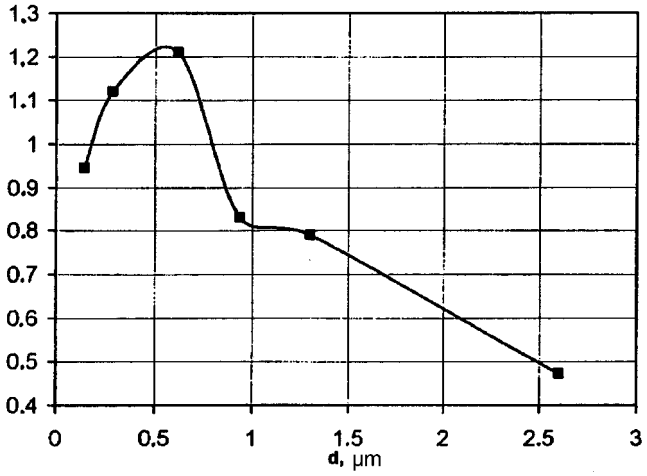

FIG. 2. Full width at half-maximum of the (005) peak from the rocking curve ($\Delta\omega$) versus film thickness d.

accompanied by annealing in an O_2 atmosphere and a component flux, and the process conditions ensure preferential growth of the $c_{\perp}$-oriented phase (possibly due to inclusions of foreign phases). It can therefore be concluded that under these process conditions the structural perfection of the films improves with thickness. It should be noted that the quality of the ''thin'' films (0.3 and 0.6 μm) was poor. However this stabilization of the $c_{\perp}$ orientation and improvement in the structural characteristics of the films with thickness is undoubtedly of interest and has not been observed before.

The microwave properties of these films were assessed by measuring the surface resistance R_s of the samples at a frequency of 60 GHz at 77 K using a copper cavity resonator. All the films showed $R_s < 50$ mΩ which is satisfactory for microwave applications and also indicates that the structure stabilizes during the growth of thick films.

In summary, it has been shown possible to grow YBCO films up to 2.6 μm thick, having good structural perfection and electrophysical characteristics, acceptable for applications in microwave electronics.

This work was supported by BMDF/VDI, Project No. 029850 (Germany).

[1] F. Vassenden, G. Linker, and J. Geerk, Physica C **175**, 566 (1991).
[2] C. W. Nieh, L. Anthony, J. Josefowicz *et al.*, Appl. Phys. Lett. **56**, 2138 (1990).
[3] S. Sievers, F. Mattheis, H. U. Krebs, and H. C. Freyhardt, J. Appl. Phys. **78**, 5545 (1995).
[4] A. H. Carim, S. N. Basu, and R. E. Muenchausen, Appl. Phys. Lett. **58**, 871 (1991).
[5] Y. J. Tian, L. P. Guo, L. Li *et al.*, Appl. Phys. Lett. **65**, 234 (1994).
[6] E. K. Hollmann, V. I. Gol'drin, D. A. Plotkin *et al.*, Fiz. Tverd. Tela (St. Petersburg) *in press* (1997) [Phys. Solid State].
[7] E. K. Hollmann, A. G. Zaitsev, V. E. Loginov, and Y. V. Likholetov, J. Phys D. **26**, 504 (1993).

Translated by R. M. Durham

Photodeflection and photoacoustic microscopy of cracks and residual stresses induced by Vickers indentation in silicon nitride ceramic

K. L. Muratikov, A. L. Glazov, D. N. Rose, J. E. Dumar, and G. H. Quay

A. F. Ioffe Physicotechnical Institute, Russian Academy of Sciences, St. Petersburg
(Submitted December 17, 1996)
Pis'ma Zh. Tekh. Fiz. **23**, 44–52 (March 12, 1997)

The feasibility of using photodeflection and photoacoustic microscopy to detect subsurface lateral and vertical cracks, as well as residual internal stresses induced by Vickers indentation in silicon nitride ceramic has been investigated. It is shown that the normal component of the photodeflection signal can be used to detect lateral subsurface cracks and the tangential component to detect vertical cracks. It is established that the sensitivity of the photoacoustic method to residual internal stresses arises from the dependence of the elastic parameters or the coefficient of thermal expansion of the silicon nitride ceramic on the internal stresses.
 [S1063-7850(97)00803-3]

Studies of the mechanical properties of ceramics are now attracting serious attention.[1] Interest in these materials stems from the extensive scope for using them in a wide range of practical applications.[2] One of the most effective approaches to the study of ceramics is based on the indentation method.[3] The system of radial and lateral cracks, as well as the internal stresses formed in the system may be utilized to determine the mechanical parameters of the material. In particular, the lengths of the growing radial cracks may be used to determine the fracture toughness of the material.[3,4]

It has now been established that optical methods are not always capable of providing accurate information on the lengths of vertical cracks,[4,5] and for ceramics in particular more reliable information may be obtained by photothermal methods. It was demonstrated in Refs. 4 and 5 that a photodeflection method can be effectively used to determine the lengths of vertical cracks. The detection of lateral subsurface cracks in nontransparent ceramics induced near the indentation zone presents serious difficulties, and it was shown in Ref. 6 that a photoacoustic gas-microphone method may be used for this purpose.

In addition to cracks, indentation generates residual internal stress fields. In transparent materials these internal stresses may be detected by polarization methods,[7] but in nontransparent materials this is a more complex problem. It was demonstrated in Refs. 8 and 9 that electron acoustic microscopy can be used to visualize residual stresses in SiC-based ceramics. However, the physical mechanism for visualization of these internal stresses was not explained. A photoacoustic method with a piezoelectric detection technique was used in Ref. 10 to detect internal stresses induced by Vickers indentation in Si_3N_4–5%Al_2O_3–5%Y_2O_3 ceramics. In this case it was assumed that the photoacoustic signal was related to the nonlinear elastic properties of the ceramic. In Ref. 11 however, the influence of the internal stresses on the photoacoustic signal was attributed to a dependence of the thermal conductivity on the internal stresses.

Unfortunately, the studies of cracks and thermal stresses in ceramics reported so far have usually been based on only one photothermal method. This considerably limits the scope for obtaining detailed information on the mechanisms of signal formation and for comparing the effectiveness of various methods. Only in Ref. 12 were several photothermal techniques used to study cracks near indentation zones as well as surface defects. However, the only results obtained were some preliminary results for zirconium-based (70%) and TiC-based (30%) ceramics and silicon-filled SiC ceramics.

In the present paper we therefore propose to study silicon nitride ceramics by means of a combined approach based on using both photodeflection microscopy and photoacoustic microscopy with a piezoelectric method of recording the signal. Such a combination of methods is expedient because their mechanisms of signal formation are different. In the photodeflection method the signal is formed by the thermal action of the exciting radiation on the object[13,14] whereas the photoacoustic method also records information on its elastic properties.[15]

An experimental investigation was made of the cracks and residual stress fields induced by Vickers indentation in silicon nitride ceramic made by hot pressing.[1)] Typical configurations of cracks and strains induced by Vickers indentation in ceramics are given in Refs. 1 and 6. The sample was indented using loads between 5 and 30 kg. An image of the area of the ceramic to be studied was obtained by scanning the sample along two coordinates. The size of the scanned region was 320×320 μm with a step of 5 μm along the two coordinates. Thermal waves and acoustic vibrations were excited in the sample by radiation from an LGN-503 argon laser modulated by an ML-201 acoustooptic modulator. Radiation from a Meles Griot 05-LHP-151 He–Ne laser was used for readout.

Thermal-wave images of the area near the indentation zone were obtained by a photodeflection technique using both the normal and tangential components of the signal. Figure 1 shows an image obtained from the normal component of the photodeflection signal for an area near the indentation zone in silicon nitride ceramic after a load of 20 kg. It can be seen that the image produced by the normal component accurately reproduces the structure of the subsurface lateral cracks and is fundamentally similar to the images obtained by the gas-microphone method.[5] However, unlike the gas-microphone method, the structure of the vertical cracks

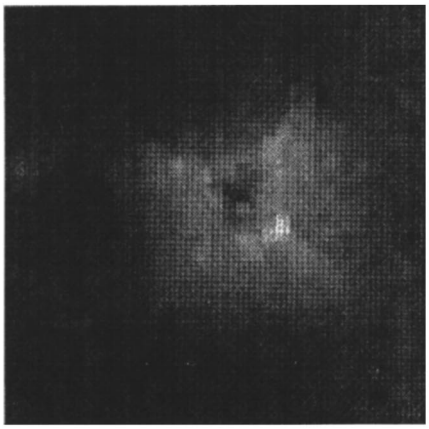

a

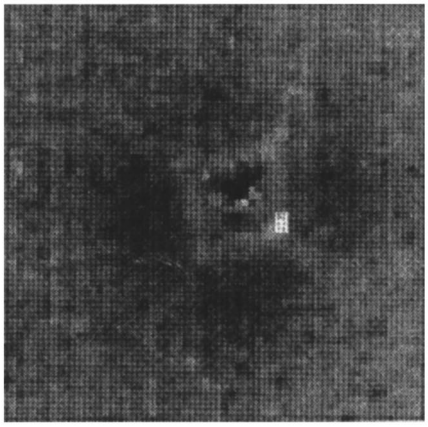

b

FIG. 1. Image of silicon nitride ceramic near Vickers indentation zone, obtained from the normal component of the photodeflection signal: a — signal amplitude, b — signal phase. The modulation frequency of the exciting radiation was 3.5 kHz and the distance between the laser beams was 22 μm.

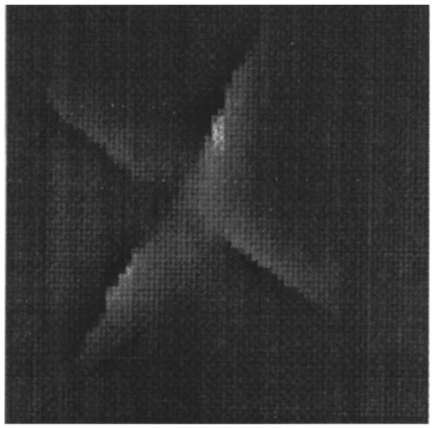

a

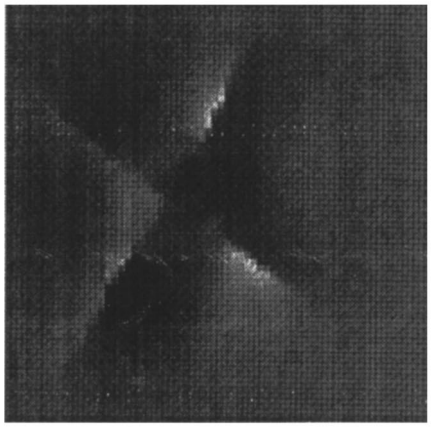

b

FIG. 2. Image of silicon nitride ceramic near Vickers indentation zone, obtained from the tangential component of the photodeflection signal: a — signal amplitude, b — signal phase. The modulation frequency of the exciting radiation was 3.5 kHz and the distance between the laser beams was 22 μm.

is also fairly well resolved on the normal photodeflection image.

Figure 2 shows an image of the same indentation zone recorded with the tangential component of the photodeflection signal under similar conditions. A distinguishing feature of these images is the considerably better contrast for the vertical cracks. For example, at a thermal wave frequency of 3.5 kHz, the contrast of the image of the vertical cracks obtained in the phase of the tangential component of the photodeflection signal is 30–50 times higher than that using the phase of the normal component. At the same time, in the images obtained using the tangential component of the photodeflection signal the sensitivity to the subsurface lateral cracks is retained. However both experimental and theoretical results show that this sensitivity is somewhat lower than that of the normal component of the photodeflection signal or the photoacoustic signal obtained with a gas-microphone cell.

Figure 3 shows an image of the area near the indentation zone obtained by the photoacoustic method, where the piezoelectric signal is recorded using PZT ceramic. A comparison between this image and those obtained previously by electron acoustic microscopy[8,9] shows that they are very similar. In particular, the bright regions near the ends of the vertical cracks correspond to zones of residual internal stresses.[9] However, the use of both the photodeflection and photoacoustic methods in the present case allows us to draw further conclusions. For instance, it can be seen from Figs. 1 and 2 that no characteristic features are observed near the ends of the vertical cracks on the photodeflection images. It can thus be stated that the thermophysical parameters of silicon nitride ceramic do not show any strong dependence on the internal stresses that might give rise to substantial changes in the photodeflection signal. Thus the photoacoustic signal in this material clearly cannot be formed by the mechanism proposed in Ref. 11, but is primarily associated with the dependences of the elastic parameters and the coefficient of thermal expansion on the residual internal stresses. However, further experiments are required to clarify the relation between the photoacoustic signal and the elastic parameters or the coefficient of thermal expansion.

At the same time, the strongly defined characteristics observed in Fig. 3 near the end of the vertical cracks may be

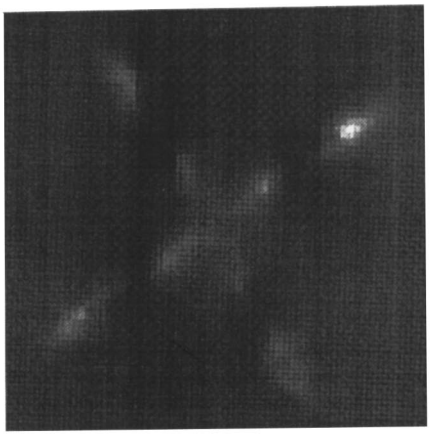

a

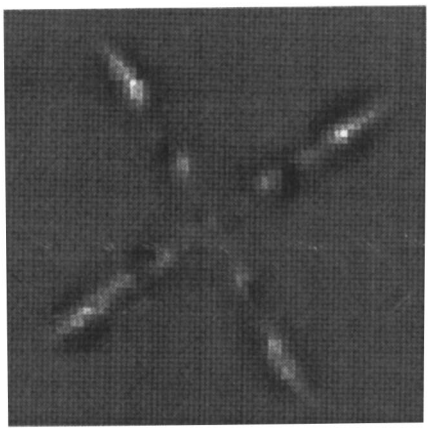

b

FIG. 3. Image of silicon nitride ceramic near Vickers indentation zone, obtained by the photoacoustic method with piezoelectric recording of the signal: a — signal amplitude, b — signal phase. The modulation frequency of the exciting radiation was 98.2 kHz.

used to pinpoint the exact position of their ends. An important advantage of the photoacoustic method over the photodeflection method and other thermal-wave techniques is that it can produce a significantly higher-contrast image of this region. However, an additional difficulty encountered when using the photoacoustic signal is that one must allow for the real distribution of the residual stresses at the surface of the sample near the ends of the cracks.

On the whole, these results show that a combination of the photodeflection and photoacoustic methods of studying indentation zones in silicon nitride ceramics can provide important information on the structure of subsurface lateral and radial cracks, and also on the residual internal stresses. To study the vertical cracks, it is best to use the tangential component of the photodeflection signal and for the subsurface lateral cracks it is best to use the normal component.

This work was partially supported by the United States Army European Research Center.

[1)]We used NC132 silicon nitride ceramic made by Norton Ceramics Corporation.

[1] R. F. Cook and G. M. Pharr, J. Am. Ceram. Soc. **73**, 787 (1990).
[2] D. O. Ajayi and K. C. Ludeme, Wear **124**, 237 (1988).
[3] P. Ostojic and R. MacPherson, Int. J. Fracture **33**, 297 (1987).
[4] J. Rantala, J. Hartikainen, and J. Jaarinen, Appl. Phys. A **50**, 465 (1990).
[5] L. J. Inglehart, *Optical Beam Deflection Detection of Thermal Waves in Opaque Solids*, Dissertation, Wayne State University, Detroit, MI (1984).
[6] D. N. Rose, D. C. Bryk, G. Arutunian, J. E. Dumar, and M. J. Slavin, J. Phys. (Paris), **4**, Colloq. C7, 599 (1994).
[7] A. Ya. Aleksandrov and M. Kh. Akhmetayanov, *Polarization Optical Methods in Mechanics of Deformable Bodies* [in Russian], Nauka, Moscow (1974).
[8] M. Urchulutegui, J. Piqueras, and J. Llopis, J. Appl. Phys. **65**, 2677 (1989).
[9] J. H. Cantrell, M. Qian, M. V. Ravichandran, and K. M. Knowles, Appl. Phys. Lett. **57**, 1870 (1990).
[10] R. M. Burbelo, A. L. Gulyaev, L. I. Robur, M. K. Zhabitenko, B. A. Atamanenko, and Ya. A. Kryl, J. Phys. (Paris) **4**, Colloq. C7, 311 (1994).
[11] M. Qian, in *Abstracts of Papers presented at Eighth International Topical Meeting on Photoacoustic and Photothermal Phenomena*, Guadeloupe (France) 1994, pp. 157–158.
[12] H. Zhang, S. Gissinger, G. Weides, and U. Netzelmann, J. Phys. (Paris) **4**, Colloq. C7, 603 (1994).
[13] W. B. Jackson, N. M. Amer, A. C. Boccara, and D. Fournier, Appl. Opt. **20**, 1333 (1981).
[14] L. C. Aamodt and J. C. Murphy, J. Appl. Phys. **52**, 4903 (1981).
[15] J. C. Rosencwaig, *Photoacoustics and Photoacoustic Spectroscopy* (Wiley, New York, 1980).

Translated by R. M. Durham

Electroluminescence induced by synchronous sinusoidal variations of the electric field and uniaxial mechanical stress in a lead magnesium niobate relaxor ferroelectric

N. N. Kraĭnik, S. A. Popov, S. A. Sushko, and S. A. Flerova

A. F. Ioffe Physicotechnical Institute, Russian Academy of Sciences, St. Petersburg; Dnepropetrovsk State University

(Submitted December 17, 1996)
Pis'ma Zh. Tekh. Fiz. **23**, 53–57 (March 12, 1997)

Changes in the electroluminescence intensity and kinetics are recorded in lead magnesium niobate crystals excited by a sinusoidal electric field and the synchronous action of uniaxial mechanical stresses in the frequency range of inelastic mechanical relaxation. The results are of interest for the development of optoelectronic tensometry and new lines of research on relaxor ferroelectrics. © *1997 American Institute of Physics.* [S1063-7850(97)00903-8]

Studies of the polarization states in inhomogeneous ferroelectric media exhibiting relaxor properties are attracting close attention among researchers because of the importance of the general problem of inhomogeneous states and the various technical applications of these materials, especially materials based on the model relaxor ferroelectric lead magnesium niobate, $PbMg_{1/3}Nb_{2/3}$ (PMN).

Particular interest is being directed toward studying the properties of these materials under applied electric fields and mechanical stresses at temperatures directly above those of the macrodomain ferroelectric state, since this is the range in which the strongest effects are observed, which are of technical importance and are caused by mechanisms of polarization switching similar to ferroelectric domain mechanisms (see, e.g., Ref. 1. These effects also include the elecctroluminescence generated as a result of adiabatic recmbination of nonequilibrium carriers whose formation is associated with changes in the domain and heterophase structures.[2,3]

In the present paper data are reported for the first time on the electroluminescence in PMN crystals exposed to the synchronous effect of sinusoidal variations of the electric field and mechanical stress.

The crystals were grown by a modified method of spontaneous crystallization.[4] An electric field $E=E_0\sin\omega t$ and the mechanical stress $\sigma=\sigma_1+\sigma_0\sin\omega t$ (the angular frequency is $\omega=2\pi f$) were applied in the [001] pseudocubic direction ($\sigma\|E$) and the optical radiation was recorded in a {100} direction. The electric field was applied by means of InGa electrodes and the mechanical stress was created by a method similar to that used in Ref. 5. The sample was clamped in a special sandwich-type crystal holder under the initial uniaxial stress σ_1 between two piezoelements to one of which was applied an electric voltage synchronous with the exciting electric field. The second piezoelement was used to determine the variable mechanical stresses developed in the crystal holder. The measurements were made at room temperature in fields below the critical value inducing the macrodomain state.[1] The field was applied to the crystal in an inhomogeneous state and containing local polar spontaneously deformed regions. The frequency f of variation of the electric field and the mechanical pressure was 3–10 kHz, i.e., in range of intensive rela ation of the dielectric polarization[6] and inelastic mechanical relaxation.[7]

Figure 1 shows oscilloscope traces of the time behavior of the exciting electric field and the luminescence intensity observed without (a) and with synchronous application (b, c) of a sinusoidal mechanical stress. A comparison of the electroluminescence intensity traces $A(t)$ without and with the

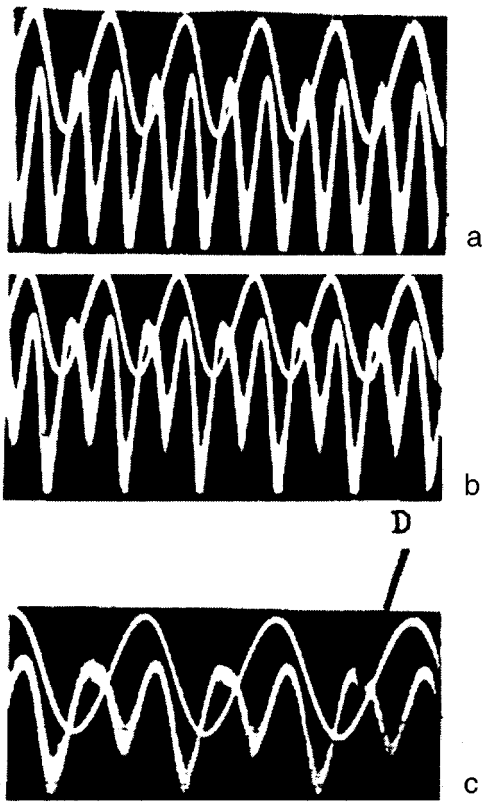

FIG. 1. Synchronous oscilloscope traces of the exciting electric field and electroluminescence of a PMN crystal under various excitation conditions. Excitation and recording conditions: peak intensity of electric field exciting luminescence, $E_0=12.7$ kV/cm (a, b, c); static uniaxial stress, $\sigma_1=70$ kg/cm^2 (a, b, c); peak value of ac component of mechanical stresses, $\sigma_0=65$ kg/cm^2 (b, c); frequency f of sinusoidal electric field, (a, b, c) and sinusoidal mechanical stresses in kHz: 5.0 (a, b) and 8.0 (c); the channels of the SI-77 oscilloscope recording the electric field and the luminescence have the same zero levels; the gain in the luminescence recording channel is 2.5 times higher for traces *a* and *b* compared with trace *c*; temperature $T=293$ K; D — section of depolarization luminescence.

application of static compression $\sigma = \sigma_1$ reveals that the photopulse parameters are almost the same as for excitation by a pulsed electric field.[8] When an ac stress of amplitude $\sigma_0 \cong \sigma_1$ is applied to the crystal, the luminescence amplitude $A_{\max}$ of every second (first) pulse is reduced by 25–30% and the kinetics of $A(t)$ changes (see Figs. 1b and 1c).

In the absence of the ac component of the mechanical stress, the repetition frequency of the luminescence pulses is twice the frequency of the exciting sinusoidal field and each individual pulse develops in the time intervals between the two closest values of the phase $n\pi \mp \Delta$ (n is an odd number, $\Delta \ll \pi$) (Ref. 3). If we disregard the negligible unipolarity of a real sample, the conditions for the generation and development of two neighboring pulses are identical. In the experiments reported in the present paper the ac mechanical stresses, which are compressive on the two nearest branches (for example, between $\pi/2$ and $3\pi/2$ and between $3\pi/2$ and $5\pi/2$), have first time derivatives of different sign. As the compression increases, the luminescence pulse remains almost constant but when the compression decreases, the depolarization of the crystal changes. A reduction in pressure (relative dilatation of the crystal) delays the decay of the polarized state (see Fig. 1c, part D), which determines the change in the photopulse development kinetics and the decrease in the luminescence amplitude. These changes exhibit clearly correlated amplitude-frequency dependences (see frames b and c in Fig. 1), which suggests that inelastic mechanical relaxation of domain-like formations plays an important role in this relaxor.

Thus, mechanical stresses varying synchronously with an electric field significantly influence the nature and intensity of domain-like collective reorientations of the polarization accompanied by various processes of nonequilibrium charge carrier formation. The luminescence recorded in this case cannot be considered to be the result of a simple summation of the electro- and tensoluminescence since these effects in PMN crystals are caused by strongly interacting processes of polarization switching in which the same crystal atomic groups participate. These domain-like processes caused by synchronous variations of the electric field and mechanical stresses are accompanied in an inhomogeneous medium by interacting changes in the local electric fields and macrodeformations, also including electrostrictive deformations.

Further studies of the electroluminescence induced by synchronous variations of the electric field and mechanical stress would be interesting in connection with advancing our ideas on the changes in the local electric fields and mechanical stresses and their mutual influence in inhomogeneous ferroelectric media. The strong interaction observed between these processes opens up the possibility of using electroluminescence for independent measurements of varying mechanical stresses.

This work was partially supported by the Russian Fund for Fundamental Research, Grant N 96-02-16893.

[1] A. E. Glazounov, A. K. Tagantsev, and A. J. Bell, Phys. Rev. B **53**, 11281 (1996).
[2] S. A. Flerova, S. A. Popov, N. N. Kraĭnik, O. E. Bochkov, and A. P. Lazarev, Fiz. Tverd. Tela (Leningrad) **27**, 3492 (1985) [Sov. Phys. Solid State **27**, 2108 (1985)].
[3] S. A. Flerova, A. Yu. Kudzin, O. E. Bochkov, and N. N. Kraĭnik, Fiz. Tverd. Tela (Leningrad) **31**, 123 (1989) [Sov. Phys. Solid State **31**, 243 (1989)].
[4] I. E. Myl'nikova and V. A. Bokov, *Crystal Growth* [in Russian], Vol. 3, Akad. Nauk SSSR, Moscow (1961), pp. 438–446.
[5] S. A. Flerova, A. Yu. Kudzin, O. E. Bochkov, and N. N. Kraĭnik, Pis'ma Zh. Tekh. Fiz. **14**, 1960 (1988) [Sov. Tech. Phys. Lett. **14**, 850 (1988)].
[6] *The Physics of Ferroelectric Effects*, edited by G. A. Smolenskiĭ [in Russian], Leningrad (1985).
[7] D. Viehland, S. J. Jang, E. Cross, and M. Wuttig, Philos. Mag. **64**, 835 (1991).
[8] N. N. Kraĭnik, S. A. Flerova and S. A. Popov, Fiz. Tverd. Tela (Leningrad) **29**, 2845 (1987) [Sov. Phys. Solid State **29**, 1636 (1987)].

Translated by R. M. Durham

High-power HF laser pumped by an electron-beam-initiated chemical nonchain reaction

É. N. Abdullin, A. M. Efremov, B. M. Koval'chuk, V. M. Orlovskiĭ, A. N. Panchenko, É. A. Sosnin, V. F. Tarasenko, and A. V. Fedenev

Institute of High-Current Electronics, Siberian Branch of the Russian Academy of Sciences, Tomsk
(Submitted December 4, 1996)
Pis'ma Zh. Tekh. Fiz. **23**, 58–64 (March 12, 1997)

The development of a high-power HF laser pumped by a chemical nonchain reaction initiated by a radially converging electron beam is reported. A radiation energy of ~115 J with an efficiency of ~8% in terms of deposited energy has been achieved in a mixture with an active volume of ~30 liters. It is shown that because of the high SF_6 density, the total pressure jump in SF_6–$H_2(D_2)$ mixtures caused by the electron beam injection and the chemical reactions is several times smaller than that in the active mixtures of exciplex lasers for the same input energies. This factor considerably facilitates the development of wide-aperture HF and DF lasers with an SF_6 fluorine donor pumped by an electron-beam-initiated chemical nonchain reaction. © *1997 American Institute of Physics.* [S1063-7850(97)01003-3]

1. Chemical lasers, especially the HF laser ($\lambda \approx 2.6$–3.2 μm), pumped by chain and nonchain reactions have been studied since 1965.[1] The most important results obtained up to 1982 are summarized in Refs. 2 and 3. Electron beams, discharges, optical radiation, and other methods are used to initiate the chemical reactions. The highest pulsed and specific output energies have been achieved for HF lasers pumped by chain reactions. However, HF and DF chemical lasers pumped by nonchain reactions are more suitable for many applications because they are simpler and safer to operate, although they have inferior energy characteristics. Recent years have seen a considerable upsurge in interest in the study of chemical lasers[4–9] because of new possibilities for using lasers with superior energy characteristics in the infrared.

In the present paper we report results of experimental investigations of a wide-aperture SF_6–H_2 laser pumped by a radially converging electron beam. A radiation energy of ~115 J has been obtained with an 8% efficiency relative to the electron beam energy deposited into the gas.

2. For the experiments we used a compact laser with an active volume of ~30 liters, which had previously delivered an output energy of ~100 J using XeCl* ($\lambda = 308$ nm) and KrF* ($\lambda = 249$ nm) molecules.[10] The electron accelerator with vacuum insulation used to generate a radially converging electron beam from four velvet cathodes was described in detail in Ref. 11. All the results presented below were obtained for the following parameters: charging voltage of the nine-stage pulse voltage generator 80 kV, voltage across the vacuum diode ~400 V, beam current ~40 kA, and length of beam power pulse at half-maximum ~500 ns. Unlike in Refs. 10 and 11, here the pulse voltage generator was positioned horizontally so that height of the optic axis could be reduced to 80 cm. The active volume of the laser chamber was ~100 cm long and 20 cm in diameter. The working mixtures consisting of hydrogen and SF_6 were prepared in the laser chamber. Several types of cavities were used. The opaque mirrors consisted of plane and concave spherical Al mirrors, as well as a gold-coated plane mirror. The exit mirrors were plane-parallel NaCl, KRS-5, and KRS-6 plates with reflection coefficients of 9%, 33%, and 27%, respectively in the ~3 μm range.

The energy ΔW transferred to the gas from the electron beam and from the chemical reaction was determined from the pressure rise in the laser chamber after injection of the beam.[10,11] The pressure jump ΔP was recorded with a 6MDKh-3B mechanotron. The values of ΔW were calculated using the relation

$$\Delta W = 0.36 \rho C V \Delta P. \tag{1}$$

Here ρ is the gas density at a temperature of 273 K and a pressure of 760 torr, C is the specific heat at constant volume, and V is the gas volume. For SF_6 we have $\rho = 6.5$ g/liter and the specific heat at constant pressure is $C_1 = 0.659$ J/g·deg (Ref. 12). Setting $C_1/C \approx 1.33$, we obtain from Eq. (1)

$$\Delta W = 1.15 V \Delta P, \tag{2}$$

where ΔW is in joules, V is in liters, and ΔP is in Torr.

The laser radiation energy was determined using two IMO-2 calorimeters positioned at different points in the laser output beam and TPI-2M calorimeters which were used to measure the energy distribution over the cross section of the output beam when studying lasing in XeCl and KrF lasers.[10] The radiation energy for an optimum SF_6:H_2 = 8:1 mixture was measured by two IMO-2 calorimeters simultaneously when the accelerator was first switched on, so that the distribution of the radiation energy over the cross section of the output beam could be determined.

3. The main results are plotted in Figs. 1 and 2. Figure 1a gives the energy deposited in the gas, which was determined from the pressure jump in an SF_6–H_2 working mixture and pure SF_6, plotted as a function of pressure up to 1 atm. In SF_6 the energy deposited in the gas stops increasing at ~0.6 atm (curve *2*) whereas in the SF_6–H_2 mixture (curve *1*), the deposited energy is higher at the same pressures and continues to increase with pressure. The energy difference (*3*) between curves *1* and *2* corresponds to the energy released by the chemical reaction. It can be seen that this en-

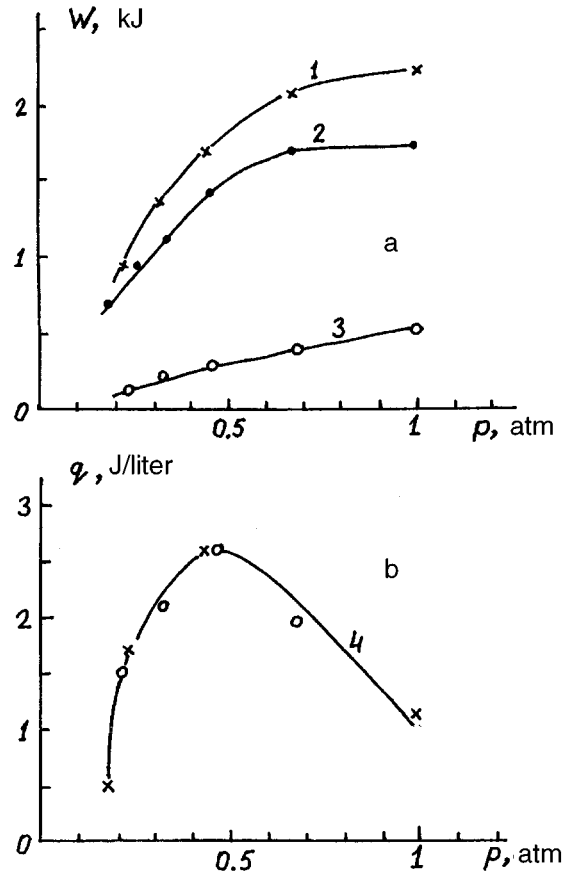

FIG. 1. Energy deposited in gas (a) and specific radiation energy on the axis of the laser chamber (b) versus pressure of SF_6:H_2 = 8:1 mixture (*1, 3, 4*) or SF_6 (*2*): *1* — total input energy of electron beam and chemical reaction; *2* — input energy from electron beam; *3* — input energy from chemical reaction.

ergy increases almost linearly with the pressure of the working mixture and at 0.45 atm accounts for ~20% of the energy deposited by the electron beam.

Figure 1b shows the specific laser radiation energy of an SF_6:H_2 = 8:1 mixture plotted versus pressure. The cavity, which was optimized for this experiment, was formed by a plane opaque gold-coated mirror and a plane-parallel KRS-5 plate, and the radiation energy was measured on the axis of the laser chamber. Our task was to obtain the highest specific radiation energy on the axis of the laser chamber. It can be seen from Fig. 1b that the highest specific radiation energy on the axis of the laser chamber is achieved at a mixture pressure of 0.45 atm. Under these conditions, the maximum specific laser radiation energy of ~5 J/liter was recorded at a distance of 1–3 cm from the foil and the total radiation energy was ~115 J. An increase in the pressure of the working mixture from 0.45 atm to 1 atm was accompanied by an increase in the energy deposited in the gas from the chemical reaction (it was approximately doubled) and also in the energy deposited by the electron beam (by ~20%). The total radiation energy and the specific radiation energy near the foil also showed an increase. However, the distribution of the radiation energy over the laser output beam became more nonuniform, and for some parts of the active volume (near

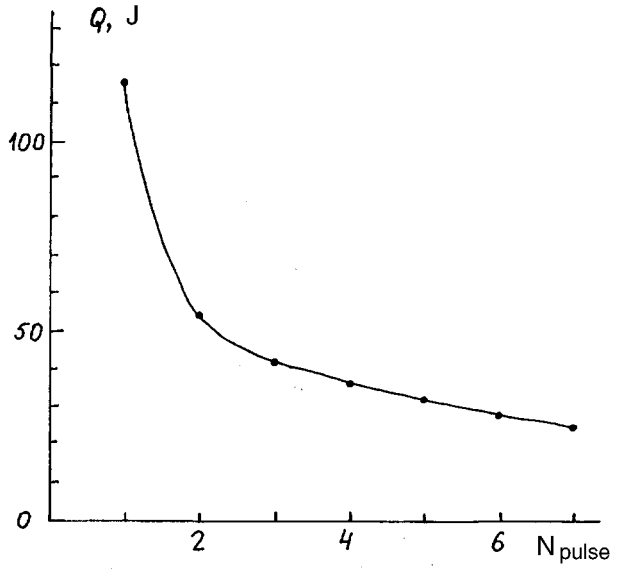

FIG. 2. Laser radiation energy versus pulse number in one portion of SF_6:H_2 = 8:1 mixture at a pressure of 0.45 atm.

the wall and the axis) we needed to use exit mirrors with widely differing reflection coefficients. Estimates indicate that then the working mixture pressure is ~1 atm and the radiation energy is distributed nonuniformly over the laser output beam, the total laser energy should be ~200 J.

Figure 2 gives the radiation energy in one portion of the working mixture as a function of the number of pulses. As expected, the maximum radiation energy and efficiency are achieved in the first pulse. In subsequent pulses from the third onward, the drop in the laser radiation energy from one pulse to another does not exceed 20%.

An important feature of the working mixture of HF and DF chemical lasers pumped by an electron-beam-initiated chemical nonchain reaction in SF_6 mixtures is the comparatively small pressure jump in the gas when the electron beam is injected and the chemical reaction takes place. For instance, when the pressure of the SF_6:H_2=8:1 mixture was ~1 atm, the pressure jump was only 0.046 atm, whereas for argon (used as the buffer gas in most electron-beam-pumped exciplex and excimer lasers: gas density $\rho = 1.78$ g/liter, specific heat $C = 0.519$ J/g·deg; Ref. 12) the pressure in the laser chamber increases substantially and may rupture the dividing foil. Assuming that $C_1/C \approx 1.67$ for argon, Eq. (1) yields for this laser

$$\Delta W = 0.2V\Delta P. \tag{3}$$

That is to say, the pressure jump for the same input energies in argon will be almost six times greater than that in SF_6.

4. In summary, we have investigated a wide-aperture HF laser pumped by a chemical nonchain reaction initiated by a radially converging electron beam. A pulse energy of ~15 J with an efficiency of ~8% in terms of deposited energy have been achieved with a no more than twofold difference in the radiation energy density over the cross section of the laser output beam. It has been shown that because of the high SF_6 density, the total pressure jump caused by injection of the electron beam and the chemical reaction is several times

less than that in the working mixtures of exciplex lasers. This factor considerably simplifies the development of wide-aperture HF and DF lasers with SF_6 fluorine donor pumped by an electron-beam-initiated chemical nonchain reaction. It may be predicted that with the wide-aperture laser with an active volume of 600 liter pumped by a radially converging electron beam[11,13] developed at the Institute of High-Current Electronics of the Siberian Branch of the Russian Academy of Sciences, it will be possible to achieve an infrared radiation energy higher than 1 kJ in SF_2–$H_2(D_2)$ mixtures.

[1] J. V. V. Kasper and G. C. Pimentel, Phys. Rev. Lett. **14**, 352 (1965).
[2] *Handbook of Chemical Lasers*, edited by R. W. Gross and J. F. Bott (Wiley, New York, 1976) [Russ. transl., Mir, Moscow, 1980].
[3] A. S. Bakshin, V. I. Igoshin, A. N. Oraevskiĭ, and V. A. Shcheglov, *Chemical Lasers* [in Russian], Nauka, Moscow (1982).
[4] B. D. Barmashenko, A. Elior, E. Lebiush, and S. Rosenwaks, J. Appl. Phys. **75**, 7653 (1994).
[5] I. I. Galaev, S. V. Konkin, A. D. Latyshev, M. V. Morov, V. K. Rebane, M. A. Rotynyan, N. N. Tomashevich, R. E. Tret'yakov, and I. A. Fedorov, Kvantovaya Electron. (Moscow) **23**, 217 (1996).
[6] M. Gastaud, J. Bouesc, and M. Autric, Technical Digest of Papers presented at 11th Intern. Symposium on Gas Flow and Chemical Lasers and High Power Laser Conference (GCL/HPL'96), Edinburgh, 1996, p. 62.
[7] V. P. Borisov, V. V. Burtsev, S. V. Velikanov, A. Ya. Dovgiĭ, A. M. Podavalov, S. N. Sin'kov, Yu. N. Frolov, Yu. N. Sheremet'ev, and V. V. Shchurov, Kvantovaya Electron. (Moscow) **23**, 119 (1996).
[8] A. S. Bashkin, A. S. Boreĭko, V. V. Lebachev, V. P. Moshkov, and I. A. Fedorov, Kvantovaya Electron. (Moscow) **23**, 428 (1996).
[9] B. P. Aleksandrov, A. A. Stepanov, and V. A. Shcheglov, Kvantovaya Electron. (Moscow) **23**, 490 (1996).
[10] É. N. Abdullin, S. P. Bugaev, A. M. Efremov, V. B. Zorin, B. M. Koval'chuk, V. V. Kremnev, S. V. Loginov, G. A. Mesyats, V. S. Tolkachev, and P. N. Shchanin, Prib. Tekh. Éksp. No. 5, 138 (1993).
[11] É. N. Abdullin, V. I. Gorbachev, A. M. Efremov, B. M. Koval'chuk, S. V. Loginov, V. S. Skakun, V. F. Tarasenko, V. S. Tolkachev, A. V. Fedenev, E. A. Fomin, and P. N. Shchanin, Kvantovaya Electron. (Moscow) **20**, 652 (1993) [Quantum. Electron. **23**, 564 (1993)].
[12] *Handbook of Tables of Physical Quantities*, edited by I. K. Kikoin [in Russian], Atomizdat, Moscow (1976).
[13] B. M. Koval'chuk, V. F. Tarasenko, and A. V. Fedenev, Kvantovaya Electron. (Moscow) **23**, 504 (1996).

Translated by R. M. Durham

Precipitation of mobile copper from $Cu_{2-x}Se$ samples under impact loading

M. A. Korzhuev

A. A. Baĭkov Institute of Metallurgy, Russian Academy of Sciences, Moscow
(Submitted November 20, 1996)
Pis'ma Zh. Tekh. Fiz. **23**, 65–69 (March 12, 1997)

It has been found that the rate of copper precipitation from samples of the superionic conductor copper selenide, $Cu_{2-x}Se$, exposed to impact loading is substantially higher than that under static pressure. This effect is attributed to the action of excess pressures and temperatures at crystal grain boundaries during the plastic deformation of the samples under impact.
 [S1063-7850(97)01103-8]

A characteristic feature of superionic conductors (solid electrolytes) is their high ionic mobility, and thus many of the effects observed in them are unusual for solids.[1,2] Precipitation of mobile copper from the solid solution ($Cu_{2-x}Se \rightarrow Cu_{2-x-\Delta x}Se + Cu$, $\Delta x > 0$) has been observed as a result of pressing[3] or plastic deformation[4] of the superionic conductor copper selenide $Cu_{2-x}Se$, which exhibits mixed electronic (p-type) and ionic (via the copper) conductivity.

In the present study it is observed that under impact loading the rate of copper precipitation from a $Cu_{2-x}Se$ solid solution may be increased substantially by the effects of excess pressure and temperature at crystal grain boundaries during the plastic deformation of the samples under impact.[5]

Polycrystalline samples of $Cu_{2-x}Se$ ($x=0.005$ and 0.01, which correspond to the boundaries of the range of homogeneity of the compound at the test temperatures) were obtained by ampoule synthesis.[6] Impact loads ($P=5\times10^7$ Pa) were applied to the samples ($h=8$ mm) in steel dies 5 mm in diameter (Fig. 1) at temperatures $T=300$ K ($T<T_C$) and 450 K ($T>T_C$) (here $T_C=413$ K is the temperature of the superionic phase transition). After each impact measurements of the thermoelectric power α^{300K} were used to determine the sample composition x' and $\Delta x = x' - x$ (to within ± 0.0015) (Ref. 7). The dies had either flat or conical ends (90° vertex angle).[8] In the former case the sample experienced pulsed uniaxial compression under impact, while in the second case, it also underwent additional plastic deformation with overpressing.

Figure 2 gives the matrix composition of $Cu_{2-x}Se$ alloys as a function of the number of impacts N accompanied by (*1*, *2*) and not accompanied by (*3*, *4*) overpressing of the samples. It can be seen from Fig. 2 that in the former case, the matrix composition of the $Cu_{2-x}Se$ alloys remained almost unchanged ($\Delta x \sim 0$) (curves *3* and *4*), which can be explained by the short duration of the impact loading $N\times t$ (N is the number of impacts and t is the effective impact time). In fact it requires a time $t^* \sim 10\tau$ to observe the escape of mobile copper from compact $Cu_{2-x}Se$ samples to the surface under the pressure,[3] where $\tau = d^2/(\pi^2 D)$ is the characteristic diffusion time of the mobile copper in the sample, $d \sim 1$ cm is the size of the sample, and D is the diffusion coefficient of the mobile copper. Since for $Cu_{2-x}Se$ the diffusion coefficient is $D^{300K(450K)} \sim 10^{-6(-3)}$ cm^2/s, we have $t^*_{300K(450K)} \sim 10$ days (20 min),[3] whereas the estimated total impact loading time ($N_{max} \sim 200$) for our samples did not exceed $t=0.2$–1 s.

When the samples were overpressed under impact, the matrix composition of the $Cu_{2-x}Se$ alloys changed significantly ($x \rightarrow 0.2$) (curves *1* and *2*, Fig. 2). The observed effect may be caused by the excess pressure and temperature at the Hertz points of instantaneous contact ($p^* \gg \overline{p}$, $T^* \gg T$, where $\overline{P}$ and T are the average pressure and temperature) generated when the crystal grains slip past each other because of overpressing (curve *5*, Fig. 2) (Refs. 9–11).

The condition of sample compactness ceases to hold during overpressing (the diffusion length d decreases in the limit to crystal grain sizes), which reduces the characteristic copper precipitation time τ. The copper precipitated from the samples under impact loading was observed as microprecipitates with $d \sim 1$–3 μm in intergranular spaces and not at the surface of the samples and the die, as under prolonged static loading (Fig. 1) (Ref. 3). The size of the crystal grains in these samples was $d \sim 100\mu$m so that the time needed for precipitation of copper from a grain is estimated as $t^*_{300(450)K} \sim 100(0.01)$ s.

The mechanism for precipitation of copper from $Cu_{2-x}Se$ under impact is therefore as follows. As the samples undergo overpressing under impact, the pressure and temperature are increased at the Hertz points of instantaneous contact (curve *5*, Fig. 2) and the mobile copper diffuses preferentially toward crystal grain boundaries where it is precipitated as a separate phase ($\Delta x > 0$). After a few minutes ($t \gg t^*$) the copper distribution over the grain equal-

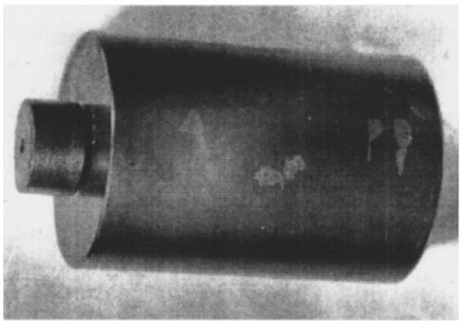

FIG. 1. Cylindrical die used to apply static or impact loads to $Cu_{2-x}Se$ samples. The light spots on the surface of the die are copper precipitated from the samples in prolonged static tests.

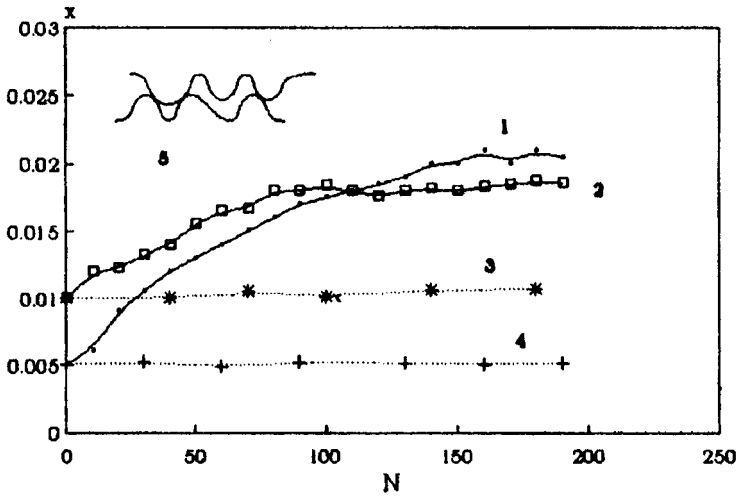

FIG. 2. Composition of $Cu_{2-x}Se$ versus number of impact loads accompanied by (*1*, *2*) and not accompanied by (*3*, *4*) overpressing of the samples. Initial composition of samples x: *1*, *4* — 0.005, *2*, *3* — 0.01; test temperature T, K: *1*, *4* — 300 K, *2*, *3* — 450 K; *5* — diagram showing formation of Hertz points of instantaneous contact.

izes and the cycle is repeated under the next impact. As the number N of impacts increases, the composition x' of the samples is shifted well into the homogeneous range of the compound[6] and the diffusion fluxes of mobile copper from the Hertz regions (curve *5*, Fig. 2) are redistributed from the surface into the crystal grain.

Curves *1* and *2* (Fig. 2) can be used to estimate the excess pressure P^* and temperature T^* in the $Cu_{2-x}Se$ samples at the Hertz points of instantaneous contact. Using the values $\Delta x/\Delta P \sim 0.01$/GPa (Ref. 3) and the phase diagram of Cu–Se near $Cu_{2-x}Se$ (Ref. 6), curves *1* and *2* (Fig. 2) for samples with $x=0.005$ ($\delta x=0.07$) and 0.01 ($\Delta x=0.09$) yield the estimates $p^* \sim 1.5$ and 0.8 GPa, $I^* \sim$ 1390 and 1380 K, either of which could produce the observed effect. However these values of T^* are highly exaggerated and the characteristics of the $Cu_{2-x}Se$ phase diagram[6] also show that the temperature factor is not dominant in this effect. In fact, the derivative $\Delta x/\Delta T$ has the positive sign needed to explain this effect only in the temperature range $T=300 \rightarrow 413$ K ($\Delta x=+0.005$) and $T>1380$ K, while in the range $T=413$–1380 K we find $\Delta x/\Delta T<0$ (Ref. 6).

From this it follows that the temperature factor can only be important for the sample with $x=0.05$ if the temperature at the Hertz points increases to $T^*>413$ K under impact. Assuming that an instantaneous temperature rise of 100–200 K at the Hertz points is quite feasible,[5] and subtracting the corresponding temperature contribution to Δx, for the sample with $x=0.005$ we finally obtain $p^* \sim 1$ GPa which is close to the estimate $P^* \sim 0.8$ GPa for the sample with $x=0.01$. This result can be explained if, other conditions being equal, the value of p^* is determined by the grain hardness H which for $Cu_{2-x}Se$ depends only weakly on composition and temperature.[12] Using these values of p^* we find that the pressure factor obviously makes the dominant contribution to the observed effect in $Cu_{2-x}Se$ and the efficacy of the pressure under impact is increased $p^*/p \sim 20$ times.

It has therefore been found that the rate of copper precipitation from the superionic conductor $Cu_{2-x}Se$ under impact loading may be increased substantially if the impact is accompanied by plastic deformation of the samples. The observed effect should be taken into account in the mechanical treatment of $Cu_{2-x}Se$ samples and may obviously be observed in other superionic conductors.

[1] *Physics of Superionic Conductors*, edited by M. B. Salamon (Springer-Verlag, New York, 1979) [Russ. transl. Zinatne, Riga, 1982].
[2] V. N. Gurevich, *Solid Electrolytes* [in Russian], Nauka, Moscow (1992).
[3] M. A. Korzhuev, N. Kh. Abrikosov, and I. V. Kuznetsova, Pis'ma Zh. Tekh. Fiz. **13**, 9 (1987) [Sov. Tech. Phys. Lett. **13**, 4 (1987)].
[4] M. A. Korzhuev, Fiz. Khim. Obrab. Mater. No. 5, 153 (1993).
[5] J.-P. Poirier, *Creep of Crystals* (Cambridge University Press, Cambridge, 1985).
[6] M. A. Korzhuev, V. V. Baranchikov, N. Kh. Abrikosov, and V. F. Bankina, Fiz. Tverd. Tela (Leningrad) **26**, 2209 (1984) [Sov. Phys. Solid State **26**, 1341 (1984)].
[7] M. A. Korzhuev, Pis'ma Zh. Tekh. Fiz. **15**(21), 24 (1989) [Sov. Tech. Phys. Lett. **15**, 839 (1989)].
[8] M. A. Korzhuev, V. F. Bankina, and N. Kh. Abrikosov, Pis'ma Zh. Tekh. Fiz. **11**, 656 (1985) [Sov. Tech. Phys. Lett. **11**, 272 (1985)].
[9] N. N. Sirota, M. A. Korzhuev, M. A. Lobzov, N. Kh. Abrikosov, and V. F. Bankina, Dokl. Akad. Nauk SSSR **281**, 75 (1985) [Sov. Phys. Dokl. **30**, 241 (1985)].
[10] N. Kh. Abrikosov, M. A. Korzhuev, V. F. Bankina, and I. V. Kuznetsov, Zh. Tekh. Fiz. **57**, 1406 (1987) [Sov. Phys. Tech. Phys. **32**, 835 (1987)].
[11] M. A. Korzhuev and L. M. Sergeeva, Pis'ma Zh. Tekh. Fiz. **14**, 301 (1988) [Sov. Tech. Phys. Lett. **14**, 133 (1988)].
[12] M. A. Korzhuev, I. G. Korol'kova, and N. Kh. Abrikosov, Izv. Akad. Nauk. SSSR Ser. Neorg. Mater. **23**, 1962 (1987).

Translated by R. M. Durham

Dynamics of field dislocations and disclinations in a few-mode fiber. IV. Formation of an optical vortex

A. V. Volyar, T. A. Fadeeva, and Kh. M. Reshitova

Simferopol State University
(Submitted November 11, 1996)
Pis'ma Zh. Tekh. Fiz. **23**, 70–75 (March 12, 1997)

The physical mechanisms responsible for the formation of an optical vortex in the field of a few-mode fiber have been investigated experimentally and theoretically. In an optical fiber with a parabolic refractive index profile an optical vortex is formed as a result of interaction between circularly polarized rotating pure edge dislocations of circularly polarized even and odd CP_{11} modes. In a stepped-index fiber the formation of an optical vortex is also related to the simultaneous propagation of even and odd modes. The fields of these modes alter their structure over the fiber length and are not manifested by rotating edge dislocations. It has been found experimentally that a stable vortex does not alter its degree of polarization of the field at fiber lengths greater than 10 m. An unstable vortex, for which the product of the spin and the topological charge is always less than zero, periodically decays and recovers at a beat length of 0.65 m. It is noted that a stable optical vortex cannot be formed by orthogonally polarized LP_{11} modes. This is because an optical vortex transfers additional angular momentum like the CP_{11} modes whereas the LP_{11} modes do not transfer additional angular momentum of the field. [S1063-7850(97)01203-2]

Smooth laser fields in free space cannot form stable vortices. An optical vortex may be formed in the active medium of a laser cavity[1] or when laser radiation propagates through a computer-synthesized hologram.[2] In Ref. 3 we showed that the fields of the natural modes of optical fibers are carriers of optical vortices of opposite topological charge. However, in the field of a multimode fiber optical vortices of opposite charge as well as pure edge or mixed types of dislocations coexist.[4]

The aim of the present investigation was to make an experimental and theoretical study of the physical mechanism responsible for the formation of single optical vortices in the field of a few-mode fiber.

1. In the fields of the natural modes of a fiber, the topological charge l and the spin σ_z of the corresponding photon basis defined by the basis vectors $\hat{e}^+$ and $\hat{e}^-$ of the circular polarization cannot be analyzed separately for pure screw dislocations.[3] The pair of states $(l=+1,\hat{e}^+)$ and $(l=1,\hat{e}^-)$ corresponds to stable CV_1 vortices with the azimuthal number $|l|=1$. The quantum states $(l=-1,\hat{e}^+)$ and $(l=+1,\hat{e}^-)$ are characteristic of the unstable vortices IV_1. In the inhomogeneous medium of a fiber a vortex is formed by the presence of two circularly polarized even and odd CP_{11}^{ev} and CP_{11}^{od} modes. In the third part of this study we showed that in a parabolic fiber circularly polarized CP_{11} modes are rotating pure edge dislocations of the field. The axis of this type of dislocation accomplishes a complete rotation about the fiber axis at the beat length. The CP_{11} modes are fourfold degenerate: twofold in the direction of circulation and twofold in parity. The summation of even and odd CP_{11} modes with the same circulation and the phase delay $\pm\pi/2$ generates a nondecaying vortex. The stability of the vortices in a parabolic fiber is determined by the equality of the polarization corrections for the TE_{01} and TM_{01} modes and for the even and odd HE_{21} mode.

The vortices of a stepped-index fiber have a slightly different mechanism of formation. In this fiber the polarization corrections of the TE_0 and TM_{01} modes differ and the optical vortices are divided into stable and unstable. We assume that the CP_{11} modes are not exactly circularly polarized. We shall express the deviation of the polarization state in terms of the phase difference Δ between the orthogonal linear LP_{11} fields.

The fields of the elliptically polarized EV_1 vortices may be written as:

$$\begin{aligned}\mathbf{e}_t=(&\hat{\mathbf{x}}[\cos\varphi[\cos\delta\beta z-\sin\delta\beta z\exp\{i\Delta\}]\\&+i\sin\varphi[\cos(\delta\beta+\Delta\beta)z-\sin(\delta\beta\\&+\Delta\beta)z\exp\{i\Delta\}]\exp\{i\Delta\beta z\}]+\hat{\mathbf{y}}[\cos\varphi[\cos(\delta\beta\\&+\Delta\beta)z\exp\{i\Delta\}+\sin(\delta\beta+\Delta\beta)z]\exp\{i\Delta\beta z\}\\&+i\sin\varphi[\sin\delta\beta z+\cos\delta\beta z\exp\{i\Delta\}])F_1(R),\end{aligned}\quad(1)$$

where $F_1(R)$ are the radial functions of the fields, $\delta\beta$ is the difference between the propagation constants of the HF_{21} and TM_{01} modes, and $\Delta\beta$ is the difference between the propagation constants of the LP_{11_y} and LP_{11_x} modes. For right circular polarization we have $\Delta=\pi/2$ and the field (1) is transformed into the stable vortex field:

$$\mathbf{e}_t(CV_{+1}^{+})=\mathbf{e}^{+}\exp\{+i\varphi\}F_1(R).\quad(2)$$

For left circular polarization we have $\Delta=-\pi/2$ and the field (1) is transformed into the unstable vortex IV_1:

$$\begin{aligned}\mathbf{e}_t(IV_{+1})=[&\hat{\mathbf{e}}\exp\{+i\varphi\}\cos\Delta\beta z-i\hat{\mathbf{e}}^{+}\\&\times\exp\{-i\varphi\}\sin\Delta\beta z]F_1(R).\end{aligned}\quad(3)$$

A family of curves giving the degree of polarization P as a function of the fiber length z is plotted in Fig. 1a for dif-

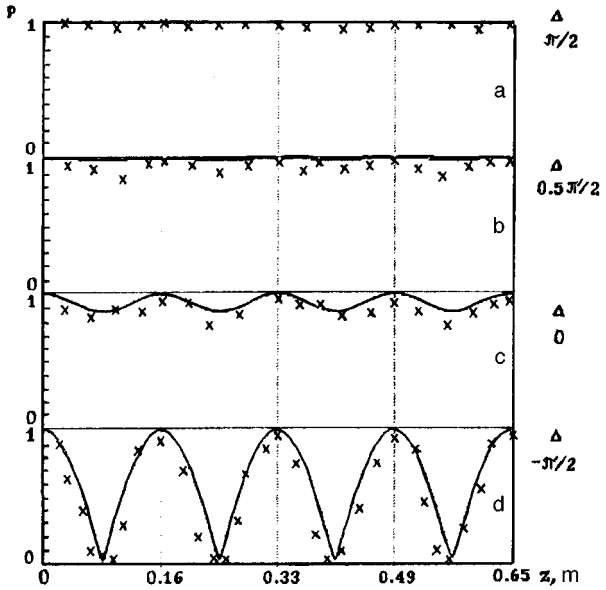

FIG. 1. Degree of polarization P of the field of $EP_{11}^{ev} \pm iEP_{11}^{od}$ modes as a function of the optical fiber length z: a — $\Delta = \pi/2$, b — $\Delta = 0.5\pi/2$, c — $\Delta = 0$, d — $\Delta = -\pi/2$. The solid curves give the theory and the crosses give the experimental points.

ferent values of the phase difference Δ. Weak perturbations of a circularly polarized field by elliptical polarization (curve *2*) typically cause small oscillations of the degree of polarization P and the vortex does not decay. The vortex becomes unstable for a linearly polarized pure screw dislocation of the exciting field, and for $\Delta = -\pi/2$ the optical vortex decays into two coupled orthogonal circularly polarized waves.

2. An experimental investigation was made of the degree of polarization P of an optical vortex as a function of the fiber length for various phase differences Δ. A few-mode optical fiber with the core radius $\rho_0 = 3.5\mu$m and the waveguiding parameter $V = 3.6$ (see Part I of this study) was excited by an optical vortex field. To produce the vortex, circularly polarized laser radiation was passed through a computer hologram of a screw dislocation with the topological charge $m = 1$ (Ref. 2), after which an optical vortex with the topological charge $+1$ became detached. The polarization state of the laser vortex was regulated by means of an acoustooptic polarization modulator by altering the control voltage on the lithium niobate crystal. The experimental points in Fig. 1 illustrate the dependence $P(z)$. For small phase differences Δ the degree of polarization is within experimental error and is close to 0.9. The largest variations of P are observed for the phase difference $\Delta = -\pi/2$, i.e., for the case $l = 1$ and a left circularly polarized field at the entrance. Note that the highest values of P are obtained for right circular polarization, and the lowest values for linear polarization. This quantum state is typical of the unstable vortex IV_1. Interference between the radiation field of a fiber 18 cm long ($\Delta\beta z = \pi/4$) and a linearly polarized reference beam for the case of a stable vortex produces a ''fork'' (Fig. 2a) with a topological charge the same as the charge of the incident vortex. For the case of an unstable vortex a pure edge dislocation is observed at this length (Fig. 2b).

A remarkable feature of the formation mechanism of a

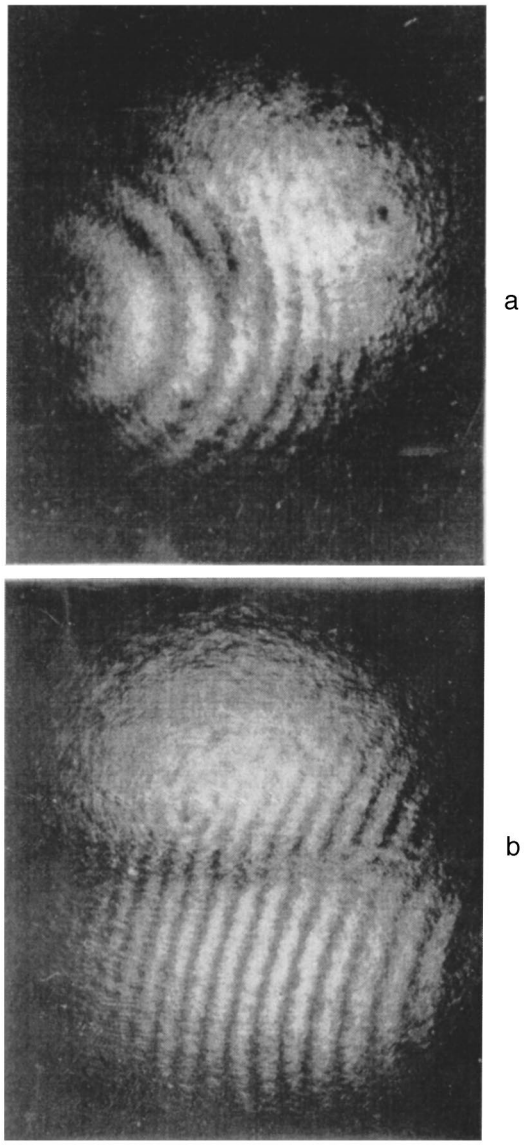

FIG. 2. Interference between an optical vortex field and a linearly polarized reference beam for $\Delta\beta z = \pi/4$: a — stable vortex, b — unstable vortex.

stable vortex is that the disclination processes in two like circularly polarized CP_{11} modes are synchronous. In the third part of this article it was noted that periodic transformations are observed in the CP_{11} mode of a stepped-index fiber. For instance, a right circularly polarized field with an edge dislocation is transformed into a field with a screw dislocation, the charge $l = 1$, and a cross-sectionally nonuniform linear polarization and back again. The angular momentum of the wave polarization is transferred to the angular momentum of the dislocation. Thus if the signs of the topological vortex and the circulation of the polarization are the same at the fiber entrance, the transfer taking place in the CP_{11} modes forming the vortex does not alter the polarization state or the sign of the topological charge, and the vortex remains stable as it propagates in the fiber. However, if the charge l and the circulation have opposite signs, the transformations in the CP_{11} modes forming the vortex lead to the formation of a vortex whose circulation and topological charge are orthogo-

nal to the incident vortex at half the beat length of the CP_{11} mode in the fiber cross section. This vortex is unstable.

We particularly note that a linearly polarized stable vortex cannot be formed from like polarized even and odd LP_{11} modes. This is first because pure edge dislocations of the field do not rotate and thus the field does not transfer additional angular momentum and second, the propagation constants of these modes are different. The CP_{11} modes transfer additional angular momentum and are capable of forming an optical vortex.

This work was partly supported by the International Soros Program for Promotion of Education in the Exact Sciences (ISSEP), Grant N PSU062108.

[1] M. Harris, C. A. Hill, and J. M. Vaughan, Opt. Commun. **106**, 161 (1994).
[2] I. V. Basistiy, M. S. Soskin, and M. V. Vasnetsov, Opt. Commun. **119**, 604 (1995).
[3] A. V. Volyar and T. A Fadeeva, Pis'ma Zh. Tekh. Fiz. **22**(8), 63 (1996) [Tech. Phys. Lett. **22**, 333 (1996)].
[4] B. Ya. Zel'dovich, N. F. Pilipetskiĭ, and V. V. Shkunov, *Phase Conjugation* [in Russian], Nauka, Moscow (1985).

Translated by R. M. Durham

Instability induced in a relativistic plasma flux by the excitation of surface waves

A. D. Kanareĭkin and I. L. Sheĭnman

St. Petersburg State Electrical Engineering University
(Submitted July 8, 1996)
Pis'ma Zh. Tekh. Fiz. **23**, 76–79 (March 12, 1997)

An analysis is made of the instability of a plasma flux caused by the excitation of a new type of cylindrical surface electromagnetic waves at the interface between the flux and a stationary plasma. It is shown that, unlike the conventional case $\varepsilon_1>0$ and $\varepsilon_2<0$, at the interface of a relativistic plasma beam there exist growing surface waves at frequencies corresponding to positive values of the permittivities on both sides of the discontinuity. For a given geometry and plasma density the critical parameter for the excitation of these waves is the wave radius of the flux. © *1997 American Institute of Physics.* [S1063-7850(97)01303-7]

In the present paper we examine one of the physical mechanisms for the hydrodynamic instabilities of relativistic electron beams caused by the formation of growing surface electromagnetic waves. The most interesting case, and one that has not been sufficiently well studied, is $\varepsilon_{1,2}>0$, i.e., when the permittivities of both adjacent media (the plasma and the flux) are positive. In this case, instability may be caused by the excitation of longitudinal charge-density waves[1] and also by the excitation of transverse surface electromagnetic waves at the interface between the moving and stationary plasma. It was shown in Ref. 2 that at a planar tangential velocity discontinuity in a dispersion-free medium, surface waves exist for $\varepsilon_1<0$ and $\varepsilon_2>0$ and calculations were made of the instability growth rates for a system comprising a plasma flux and a stationary plasma. The cylindrical geometry of the problem only results in discretization of the set of frequencies, without altering the conditions for the permittivities. However, the authors of Ref. 2 only considered the case where the wave vector $\mathbf{k}_\perp$ has the same direction as the flux velocity $\mathbf{V}$. However, when $\mathbf{k}_\perp$ and $\mathbf{V}$ are noncollinear and a certain critical angle between them is exceeded, surface waves may also exist at a tangential velocity discontinuity in a homogeneous medium: $\varepsilon_1=\varepsilon_2>0$ (Ref. 3). In cylindrical geometry the critical parameter for the existence of surface waves at frequencies corresponding to positive values of the permittivity on both sides of the interface is the index of the first allowed mode, as was shown in Ref. 4.

We shall analyze the stability of surface waves at the boundary of a relativistic plasma flux in a stationary medium having a permittivity ε_1. We shall assume that the flux is a cylinder of radius R containing a plasma of permittivity ε_2, propagating along its axis (z axis) at the velocity $V=\beta c$, where c is the velocity of light.

The instability growth rates of a plasma flux caused by the excitation of surface waves can be estimated analytically by using the dispersion equation obtained in Ref. 5 for the surface waves in a waveguide formed by a relativistic flux propagating through a plasma and substituting the following expressions for the permittivities of the stationary and moving plasmas:

$$\varepsilon_1=1-\frac{k_{p^1}^2}{k^2},\quad \varepsilon_2=1-\frac{k_{p^2}^2}{\gamma^3 k_*^2},$$

where

$$\gamma=(1-\beta^2)^{-1/2},\quad k=\omega/c,$$

$$k_*=k-\beta k_z,\quad k_{p[1,2]}^2=\frac{4\pi e^2 n_{[1,2]}}{mc^2},$$

n_1 and n_2 are the electron concentrations outside and inside the cylinder, respectively, and m and e are the electron mass and charge. The dispersion equation can then be written as

$$(\varepsilon_2 S_2-\varepsilon_1 S_1)(S_2-S_1)=\frac{\nu^2 k^2(k(1-\varepsilon_{2\perp})(k_z-k\varepsilon_1\beta)-k_z k_*(1-\varepsilon_1))^2}{k_*^2 T_1^4 T_2^4 R^4},\qquad (1)$$

where

$$S_1=\frac{K_\nu'(T_1R)}{K_\nu(T_1R)}\frac{1}{T_1R},\quad S_2=\frac{I_\nu'(T_2R)}{I_\nu(T_2R)}\frac{1}{T_2R},\qquad (2)$$

$I_\nu(x)$ is a modified Bessel function of order ν, $K_\nu(x)$ is a MacDonald function, and

$$\varepsilon_{2\perp}=1-\frac{k_{p^2}^2}{\gamma k^2},\quad T_1^2=k_z^2-k^2\varepsilon_1,$$

and $T_2^2=k_z^2-k^2\varepsilon_{2\perp}$.

We shall seek the complex solutions of Eq. (1) near the frequency of the longitudinal oscillations of the beam charge density (nonresonant instability occurs in the frequency range where $\varepsilon_2<0$ and is not considered here): $k=k_0+k_*$, $k_0=\beta k_z$, and $|k_*|\ll k_0$. In this case Eq. (1) is a quadratic equation for k_*:

$$k_*^2\left((S_2-\varepsilon_1 S_1)(S_2-S_1)-\frac{\nu^2}{R^2}\frac{(1-\varepsilon_1)^2 k_0^4}{T_1^4 T_2^4 \beta^2}\right)+2k_*\frac{\nu^2}{R^2}\frac{k_0^5(1-\varepsilon_{2\perp})(1-\varepsilon_1)(1-\varepsilon_1\beta^2)}{T_1^4 T_2^4 \beta^2}$$

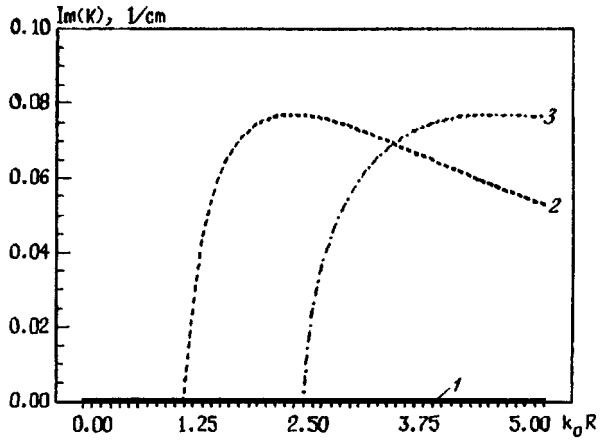

FIG. 1. Instability growth rate Im(k) versus transverse wave dimensions k_0R of waveguide for $\varepsilon_1=0.5$, $\gamma=22.2$, $n_0=10^{12}$ cm^{-3}: *1* — $\nu=0$, *2* — $\nu=1$, and *3* — $\nu=2$.

$$-\left(\frac{k_0^2(1-\varepsilon_{2\perp})}{\gamma^2}S_2(S_2-S_1)\right.$$

$$\left.+\frac{\nu^2}{R^2}\,\frac{k_0^6(1-\varepsilon_{2\perp})(1-\varepsilon_1\beta^2)}{T_1^4T_2^4\beta^2}\right)=0, \tag{3}$$

where $T_2^2=k_0^2(1-\varepsilon_{2\perp}\beta^2)/\beta^2$ and $T_1^2=k_0^2(1-\varepsilon_1\beta^2)/\beta^2$.

For $\nu=0$ we obtain

$$k_*^2=\frac{k_0^2(1-\varepsilon_{2\perp})}{\gamma^2}\,\frac{S_2}{S_2-\varepsilon_1S_1}, \tag{4}$$

i.e., the condition $S_2-\varepsilon_1S_1<0$ must be satisfied for the growth of surface waves in the zeroth-order mode. Assuming that $S_2>0$ and $S_1<0$, we obtain $\varepsilon_1<S_2/S_1<0$.

Figure 1 gives the growth rates Im(k) of the resonant instability of a relativistic flux caused by the excitation of surface waves at the interface between the flux and a stationary plasma, plotted versus the wave dimensions k_0R of the waveguide for $\varepsilon_1=0.5$, $\beta=0.999$ ($\gamma=22.2$), and $n_2=10^{12}$ cm^{-3}. It should be noted that for $\nu=0$ the dispersion equation (4) has no unstable solutions, which in planar geometry corresponds to surface waves propagating parallel to the velocity of the medium. For $\nu\neq 0$ the conditions for the excitation of waves are only satisfied for a finite set of modes, which is observed in the nonzero growth rates of the dispersion equation for $\nu\leqslant\nu_k$. For small flux radii, ν_k does not exist; i.e., no instability occurs in the moving-stationary plasma system. Thus, unlike the stable solutions the critical parameter for the unstable solutions is the cylinder radius for which the first oscillation mode is excited.

It has therefore been shown that growing surface electromagnetic waves may exist in a system formed by a relativistic plasma flux and a stationary plasma at frequencies corresponding to positive values of ε on both sides of the velocity discontinuity. It has been observed that for given β, ε, and ω the stability of the system is determined by a critical parameter — the transverse wave dimension of the flux — which in planar geometry corresponds to the angle between $\vec{\beta}$ and $k_\perp$.

The results of this study may be applied to the interaction between high-current relativistic beams and laboratory and astrophysical plasmas.

[1] A. N. Kondratenko and V. M. Kuklin, *Principles of Plasma Electronics* [in Russian], Énergoatomizdat, Moscow (1988).
[2] V. D. Pikulin and N. S. Stepanov, Zh. Tekh. Fiz. **45**, 2288 (1975) [Sov. Phys. Tech. Phys. **20**, 1429 (1975)].
[3] K. A. Barsukov and A. D. Kanareĭkin, Zh. Tekh. Fiz. **55**, 1847 (1985) [Sov. Phys. Tech. Phys. **30**, 1082 (1985)].
[4] A. D. Kanareĭkin and I. L. Sheĭnman, Pis'ma Zh. Tekh. Fiz. **22**(2), 61 (1996) [Tech. Phys. Lett. **22**, 74 (1996)].

Translated by R. M. Durham

Influence of phase and frequency modulation of a light beam on electron diffraction as a result of the Aharonov–Bohm effect

S. Yu. Davydov and A. N. Ageev

A. F. Ioffe Physicotechnical Institute, Russian Academy of Sciences, St. Petersburg
(Submitted December 4, 1996)
Pis'ma Zh. Tekh. Fiz. **23**, 80–83 (March 12, 1997)

It is shown that the phase and frequency modulation of the vector potential responsible for the Aharonov–Bohm effect causes changes in the interference pattern that may be used to study this effect under conditions of an ac magnetic flux.
[S1063-7850(97)01403-1]

In contrast to the Aharonov–Bohm effect in static magnetic fields,[1–3] studies of this effect in ac electromagnetic fields have only just begun. In Ref. 4 it was suggested that a coherent light source generating an evanescent light wave on the surface of a transparent dielectric during total internal reflection could be used for this purpose. A theoretical analysis was made of the diffraction pattern with allowance for the Aharonov–Bohm effect and a suitable experimental setup was proposed. As a further development of these ideas in Ref. 5 we calculated the correction to the broadening of the central diffraction peak and we proposed a modified e xxperimental setup which was easier to implement. In Ref. 6 we analyzed the contrast of the interference pattern and suggested that the Aharonov–Bohm effect as influenced by electromagnetic waves could be studied from the change in contrast.

Another method of investigating the effect of an electromagnetic field on the Aharonov–Bohm effect involves modulating this field. In Ref. 7 we examined how amplitude modulation of the light wave influences the diffraction pattern with allowance for the Aharonov–Bohm effect. It was shown that amplitude modulation narrows the central diffraction peak and alters the contrast (visibility) of the diffraction fringes. In the present paper we consider the influence of frequency and phase modulation on the two-slit electron diffraction pattern with allowance for the Aharonov–Bohm effect.

For both frequency and phase modulation[8] the variation of the vector potential A may be expressed in the form

$$A = A_0 \cos(\omega t + \gamma \cos \Omega t), \tag{1}$$

where A_0 is the amplitude, ω and Ω are the fundamental and the modulating frequencies, and γ determines the amplitude of the phase shift for phase modulation or the modulation index $\gamma \equiv \Delta\omega/\Omega$ for frequency modulation.

Using the results of Ref. 4, we can show (see Refs. 6–8) that the interference pattern is described by the probability P, where

$$P = \frac{1}{2}\left\{1 + \cos\left[R\Phi(t) + \frac{1}{2} R\Phi(\tau) - \omega_e \tau\right]\right\}, \tag{2}$$

$$\Phi(t) = J_0(\gamma)\sin \omega t + \omega \sum_{h=1}^{\infty} (-1)^n \left\{ J_{2n}(\gamma) \times \left[\frac{\sin(2n\Omega-\omega)t}{2n\Omega-\omega} + \frac{\sin(2n\Omega+\omega)t}{2n\Omega+\omega}\right] + J_n(\gamma) \times \left[\frac{1-\cos(n\Omega-\omega)t}{n\Omega-\omega} + \frac{1-\cos(n\Omega+\omega)t}{n\Omega+\omega}\right]\right\}, \tag{3}$$

$$R = 2e\nu A_0/\hbar c\omega, \tag{4}$$

where e is the positron charge, ν is the electron velocity, $\hbar$ is the reduced Planck's constant, c is the velocity of light, J_n is an nth-order Bessel function of the first kind, τ is the difference in the times of incidence on the screen for electrons diffracted from the first and second slits, and ω_e is the angular frequency of the electron wave.

In a first approximation we can confine our analysis to $n=0$ and $n=1$ in Eq. (3). Then assuming $\Omega \ll \omega$, we obtain:

$$\Phi(t) \simeq J_0(\gamma)\sin \omega t + 2J_1(\gamma) \times \left[\sin \omega t \sin \Omega t - \frac{\Omega}{\omega}(1 - \cos \omega t \cos \Omega t)\right]. \tag{5}$$

It was shown in Ref. 4 that the condition corresponding to the half-height of the central peak is

$$\omega_e \tau - \left[R\Phi(t) + \frac{1}{2} R\Phi(\tau)\right]_{\max} = \frac{\pi}{2}. \tag{6}$$

Assuming that

$$\Phi_{\max}(t) \simeq J_0(\gamma) - 2\left(-\frac{\pi}{2}\right)\frac{\Omega}{\omega} J_1(\gamma), \tag{7}$$

$$\Phi_{\max}(\tau) \simeq J_0(\gamma)\omega\tau, \tag{8}$$

and performing calculations similar to those in Refs. 4, 5, and 7 we obtain the following expression for the relative broadening $(\theta - \theta_0)/\theta_0$ of the interference maximum, where θ_0 is the half-width of the central peak (at half-height), in the absence of an ac electromagnetic field:

$$\frac{\theta-\theta_0}{\theta_0}=\frac{4e\nu A_0}{\pi\hbar c\omega}\left[J_0(\gamma)\left(1+\frac{\pi}{4}\frac{\omega}{\omega_e}\right)\right.$$
$$\left.-2\left(1-\frac{\pi}{2}\right)\frac{\Omega}{\omega}J_1(\gamma)\right]. \quad (9)$$

A comparison with the result obtained in Ref. 5 without any modulation ($\gamma=\Omega=0$) shows that the relative broadening $(\theta-\theta_0)/\theta_0$ is reduced. This effect is also typical of amplitude modulation.[7]

We shall now analyze the change in the contrast of the diffraction pattern when allowance is made for the Aharonov–Bohm effect caused by phase or frequency modulation of the optical signal. Adopting the approach developed in Ref. 6, we can show that the probability of incidence on a screen at a given point will be

$$P=\frac{1}{2}\{1+\cos(\tilde{\beta}\omega_e\tau)J_0[RJ_0(\gamma)]\}, \quad (10)$$

where $\tilde{\beta}=1-\omega RJ_0(\gamma)/2\omega_e$, and the contrast is

$$K=|J_0[RJ_0(\gamma)]|. \quad (11)$$

Since $J_0(\gamma)<1$, when the value of the parameter $RJ_0(\gamma)$ is less than 2.40 (this is the first zero of the Bessel function Y_0), an increase in the modulation index γ will enhance the contrast of the interference pattern. Conversely, in the range $2.40<RJ_0(\gamma)<3.84$, an increase in γ will reduce the contrast K, and so forth.

This effect stems from the oscillating behavior of the Bessel function; on the ascending sections of $|J_0|$ an increase of γ enhances the contrast K whereas on the descending sections $|J_0|$ the opposite effect occurs.

Thus like amplitude modulation, frequency and phase modulation of the light beam both narrow the central interference peak, and for ''small'' R (<2.40) enhance the contrast of the diffraction pattern when the Aharonov–Bohm effect is taken into account.

This work was supported by the Russian Fund for Fundamental Research (Grant RFFI 95-02-04064a).

[1] J. Aharonov and D. Bohm, Phys. Rev. **115**, 485 (1959).
[2] S. Olariu and I. I. Popescu, Rev. Mod. Phys. **57**, 339 (1985).
[3] M. Peskin and A. Tonomura, Lecture Notes Phys. **340**, 115 (1989).
[4] B. Lee, E. Yin, T. K. Gustafson, and R. Chiao, Phys. Rev. A **45**, 4319 (1992).
[5] A. N. Ageev and S. Yu. Davydov, Pis'ma Zh. Tekh. Fiz. **21**(23), 71 (1995) [Tech. Phys. Lett. **21**, 982 (1995)].
[6] A. N. Ageev and S. Yu. Davydov, Pis'ma Zh. Tekh. Fiz. **22**(4), 70 (1996) [Tech. Phys. Lett. **22**, 165 (1996)].
[7] A. N. Ageev and S. Yu. Davydov, Pis'ma Zh. Tekh. Fiz. in press (1997).
[8] V. V. Potemkin, *Radiophysics* [in Russian], Moscow State University, (1988).

Translated by R. M. Durham

Analysis of the kinetic equation for mass transport induced by short laser pulses

V. A. Putilin and A. V. Kamashev

Samara State Technical University
(Submitted September 9, 1996)
Pis'ma Zh. Tekh. Fiz. **23**, 84–87 (March 12, 1997)

The interaction between high-power short-pulse laser radiation and a metal target is considered. An analysis is made of the transport of material atoms from the surface layer into the bulk of a semi-infinite sample under the action of the stress field of a plane shock wave and a temperature gradient. The results of numerical calculations for a laser power density of 10^9 W/cm^2 and a pulse length of 30 ns show good agreement with the results of earlier experiments. © *1997 American Institute of Physics.* [S1063-7850(97)01503-6]

The high rate of energy input characteristic of the interaction between high-power short-pulse laser radiation and metals as well as the high rates of heating and cooling, of the order of 10^{10} K/s, create high-pressure shock waves and large temperature gradients inside the material. Experimental investigations of mass transport under the action of a laser-induced shock were reported in Refs. 1 and 2. A theoretical analysis of the kinetic equation for mass transport with allowance for pressure and thermal diffusion is now required.

Under certain assumptions and constraints,[3] one can consider a laser-induced shock wave to be planar. We shall analyze the transport of material atoms from the surface layer into the bulk of a semi-infinite metal sample under the action of the stress field of a planar shock wave and a temperature gradient.

The mass transport equation with allowance for pressure diffusion[4] and thermal diffusion may be written as

$$\frac{\partial C}{\partial t}=D\frac{\partial^2 C}{\partial x^2}+\frac{\partial}{\partial x}\left(D\frac{K_p}{P}\times\frac{\partial p}{\partial x}\right)+\frac{\partial}{\partial x}\left(D\frac{K_T}{T}\times\frac{\partial T}{\partial x}\right), \quad (1)$$

where C is the concentration, D is the diffusion coefficient, P is the pressure, $K_p\times D$ is the pressure diffusion coefficient, and $K_T\times D$ is the thermal diffusion coefficient.

In operator form this equation is

$$\hat{\mathscr{L}}c=0, \quad (2)$$

where

$$\hat{\mathscr{L}}=-\frac{\partial}{\partial t}+D\frac{\partial^2}{\partial x^2}+D_1\frac{\partial p}{\partial x}\frac{\partial}{\partial x}+D_1\frac{\partial^2 p}{\partial x^2}+D_2\frac{\partial T}{\partial x}\frac{\partial}{\partial x}+D_2\frac{\partial T}{\partial x^2},$$

$$D_1=\frac{DV_0}{kT_0}, \quad D_2=\frac{DQ_i}{kT_0^2}, \quad (3)$$

V_0 is the partial volume, k is the Boltzmann constant, T_0 is the absolute temperature of the sample surface at the instant when the laser pulse ceases, and Q_i is the heat flux.

Equation (3) is a linear parabolic equation with variable coefficients, which can be solved by the ''parametrix'' method.[4] In the first approximation the parametrix may be written as

$$\Gamma(x,t,\zeta,\tau)=Z_0(x,t,\zeta,\tau)+Z(x,t,\zeta,\tau),$$

$$Z_0(x,t,\zeta,\tau)=\frac{1}{\sqrt{4\pi D(t-\tau)}}\left\{\exp\left[-\frac{(x-\zeta)^2}{4D(t-\tau)}\right]+\exp\left[-\frac{(x+\zeta)^2}{2D(t-\tau)}\right]\right., \quad (4)$$

$$Z(x,t,\zeta,\tau)=\int_\tau^t\int_0^\infty Z_0(x,t,\eta,\sigma)\hat{\mathscr{L}}Z_0(\eta,\sigma,\zeta,\tau)\,d\eta\,d\sigma,$$

where $z_0(x,t,\zeta,\tau)$ is the fundamental solution of the Fick equation for a semi-infinite sample. Using the initial conditions:

$$c(x,0)=\begin{cases}c_0, & 0\leqslant x\leqslant d,\\ 0, & x>d,\end{cases} \quad (5)$$

where d is the thickness of the surface layer in which material of initial concentration c_0 is uniformly distributed, we can find its concentration distribution after the laser action as a functional dependence of the type $c=c(x,t)$:

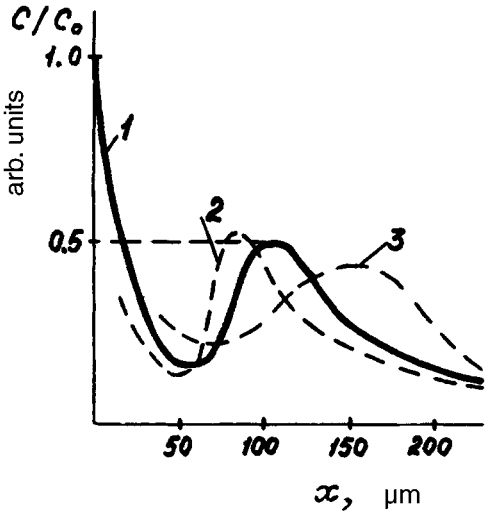

FIG. 1. Calculated concentration depth distribution of material transported by a laser-induced shock wave into a metal sample (curve *1*) and experimentally determined[2] concentration distributions: copper in nickel (curve *2*) and carbon in iron (curve *3*).

$$c(x,t)=\int \Gamma(x,t,\zeta,0)c(\zeta,0)d\zeta. \quad (6)$$

To obtain an explicit solution of Eq. (6), the pressure pulse was assumed to be a soliton and the thermal wave was described by the Heaviside step function:

$$P(x,t)=P_0\ \cosh^{-2}\left(\frac{x-\nu t-x_s}{x_0}\right), \quad (7)$$

$$T(x,t)=T_0\theta(\nu_{\mathrm{T}}\times t-x), \quad (8)$$

where ν and ν_T are the propagation velocities of the shock and thermal waves.

The results of numerical calculations using Eq. (6) for a laser power density of 10^9 W/cm^2 and a pulse length of 30 ns are plotted in Fig. 1. A concentration peak is observed at a depth of around 100 μm and the total depth of penetration of the atoms is around 300 μm. This agrees well with the results of our earlier[2] experimental investigations of the mass transport of copper in nickel and also of carbon in iron exposed to a laser-induced shock wave.

[1] V. F. Mazanko and A. E. Pogorelov, Metallofizika **6**(4), 108 (1986).
[2] A. N. Bekrenev, A. V. Kamashev, and V. A. Putilin, Pis'ma Zh. Tekh. Fiz. **19**(13), 14 (1993) [Tech. Phys. Lett. **19**, 403 (1993)].
[3] S. I. Anisimov and V. A. Kravchenko, Preprint [in Russian], ITF, Academy of Sciences of the USSR (1984)
[4] A. I. Krestelev and A. N. Bekrenev, Fiz. Khim. Obrab. Mater. No. 2, 58 (1985).

Translated by R. M. Durham

Protection of organic thin-film light-emitting diodes

B. A. Chayanov, G. M. Pleshkov, P. P. Kisilitsa, V. N. Bochenkov, Yu. O. Yakovlev, and V. F. Zolin

Institute of Radio Engineering and Electronics, Russian Academy of Sciences, Moscow
(Submitted December 5, 1996)
Pis'ma Zh. Tekh. Fiz. **23**, 88–90 (March 12, 1997)

It is demonstrated that the lifetime of organic thin-film electroluminescent light-emitting diodes can be increased many times by the deposition of protective coatings during the fabrication cycle. © *1997 American Institute of Physics.* [S1063-7850(97)01603-0]

Thin-film multilayer organic light-emitting diodes have been studied intensively following the publication of a pioneering work on the development of polymer light-emitting diodes.[1] We investigated two-layer devices with a transparent electrode formed by a mixture of indium and tin oxides (ITO), which functioned as the anode, and an aluminum cathode. The first layer of organic material is used for transport of holes and the second for transport of electrons, and this also serves as the layer in which radiative recombination takes place. We sought to solve the following problems:

1. To overcome the tendency of organic materials to oxidize and hydrolyze.

2. To reduce the sensitivity to the external temperature caused by the instability of the amorphous state of the layers.

In our attempt to select chemically stable materials, we used aluminum as the cathode material even though this choice significantly raises the barrier to electron injection for most known materials and lowers the efficiency because the device becomes ''hole-only.''[2]

As comparatively stable materials for the layer into which holes are injected, we used, in addition to oligomers of the polyarylacetylene series such as polyphenylacetylene and polyolane[3,4], also heterocyclic compounds with a finite system of conjugated bonds, including various polyvinylcarbazoles and carboranes, to fabricate a *p*-type layer. These materials somewhat improved the stability of the cells and substantially increased the breakdown voltage, but also increased the barrier to hole injection. Films of metal 8-hydroxyquinolinate were used as the *n*-type layer, which also functioned as the radiative recombination layer.

The layers were prepared by evaporation in vacuum. The thickness of the layers was between 40 and 800 nm and was monitored by the quartz-crystal oscillator method. The quality of the layers was checked with polarizing optical microscopes or electron microscopes. The electrophysical and optical properties of the diodes were investigated. The diodes had a luminence of around 500 cd/m^2, and when calcium was used as the cathode, this was increased to 1000 cd/m^2. This luminence was achieved with two-layer diodes formed by carbazole-containing polymers or complexes of phthalocyanine with aluminum hydroxyquinoline, with ITO and aluminum electrodes. The temporal stability of these diodes was poor: the luminescence intensity was approximately halved within a few minutes.

Some of the materials used by us are photoresistors. It was found that one of them, a polymer based on 1(9-carboxy-anthracene)-4(furan)-divinyl, containing 9-carboxy-anthracene radicals in the side chain,[5] functions successfully as a *p*-type layer. When deposited on the aluminum electrode, this material also provides efficient protection against corrosive components of the atmosphere, such as oxygen and water vapor. As a result, the operating life of the diodes without any additional measures of protection against the atmosphere was increased from a few minutes to tens of hours and the storage time was increased from one week to six months. With this protective layer, laboratory investigations can be carried out without using an inert atmosphere.

The hermetic sealing may also solve the problem of chemical instability.[6] Our proposed method is technologically simpler and also yields satisfactory results.

This work was supported by the Los Alamos National Laboratory under Agreement N 8990Q0004-35 with the Institute of Radio Engineering and Electronics of the Russian Academy of Sciences and by the Russian Fund for Fundamental Research under Grants N 94-02-04019a and No. 96-02-17663. This work also forms part of the A. M. Prokhorov Program on Laser Physics.

[1] J. H. Burroughes, D. D. C. Bradley, A. R. Brown *et al.*, Nature (London) **347**, 539 (1990).
[2] I. D. Parker, J. Appl. Phys. **75**, 1656 (1994).
[3] A. A. Berlin *et al.*, Izv. Akad Nauk SSSR Ser Khim. No. 10, 1875 (1965).
[4] P. P. Kisilitsa *et al.*, Izv. Akad Nauk SSSR Ser Khim. No. 11, 2453 (1967).
[5] T. Ishii, Y. Tezuka, S. Kawamoto *et al.*, J. Photochem. Photobiol. A **83**, 55 (1994).
[6] P. E. Burrows, V. Bulovic, S. R. Forrest *et al.*, Appl. Phys. Lett. **65**, 2922 (1994).

Translated by R. M. Durham

Conversion of heat into work using thermally inhomogeneous systems (revised)

G. V. Skornyakov

A. F. Ioffe Physicotechnical Institute, Russian Academy of Sciences, St. Petersburg
(Submitted January 31, 1997)
Pis'ma Zh. Tekh. Fiz. **23**, 91–95 (March 12, 1997)

An error, made when constructing an example of a quasistatic cyclic process for the complete conversion of heat into work using a nonintegrable thermodynamic system with controllable thermodynamic characteristics, is eliminated. [S1063-7850(97)01703-5]

A fundamentally new cycle for conversion of heat into work using thermally inhomogeneous systems as an intermediate heat reservoir was proposed by the author in Ref. 1. The intermediate heat reservoir is a closed cylinder whose volume is divided into two parts by a freely-sliding adiabatic piston, one part being filled with gas and the other with a two-phase gas-liquid system. The presence of the adiabatic piston in the intermediate heat reservoir ensures that the system is nonintegrable (nonholonomic). The working medium of the engine is a gas.

However, an error was made in Ref. 1 when analyzing the behavior of the thermodynamic curve of the engine because it escaped the author's attention that as the mass of gas increases in the intermediate heat reservoir, the range of variation of its volume is reduced in the first stage of the cycle and consequently the temperature drop at this stage is smaller. As a result, when the working medium in thermal contact with the gas in the intermediate heat reservoir is compressed to the initial volume, its temperature is always higher than the initial temperature and the work produced per cycle is negative.

Only one part of the intermediate heat reservoir was used to cool the working medium during its compression. Although this part is cooled at the first stage of the process to temperatures considerably lower than that of the two-phase system, its stored cold is comparatively small and is mainly concentrated in the other part. In addition, the use of parts of a system separated by an adiabatic barrier exclusively as a heat reservoir restricts their possible application in the process.

With the aim of utilizing more efficiently all the cold stored at the first stage of the process and all the scope offered by a nonintegrable system with controllable thermodynamic characteristics for the complete conversion of heat into work, both the conversion system itself and the cycle performed should be modified as follows.

Let us consider a system in which all three parts contain arbitrary quantities of material. The only constraint imposed on the parameters of the two-phase system and the gas filling the intermediate heat reservoir is

$$\frac{\gamma_2-1}{\gamma_2}\cdot\frac{q_p}{T_0}>1. \tag{1}$$

The design of the system may be represented as a cylinder with a working piston connected to an external load, where the volume of the cylinder is divided into three parts by two heat-insulating pistons. One of these pistons is a moving adiabatic barrier separating the two-phase system and the gas in the intermediate heat reservoir, and the other, located close to the working piston, may be fixed. The gas enclosed between these two pistons, identical to the gas in the heat reservoir, may be considered to be the working medium of the engine. Thermal contact may be established and broken between all three parts of the system. Thermal contact may also be established and broken between the system as a whole and a heater.

In the initial state, the system is in thermal contact with the heater, both pistons dividing the cylinder volume are free, and the pressure in all three parts of the system is the same, P_0. At the heater temperature T_0, the liquid phase is completely vaporized and the corresponding volume V_1 is filled with saturated vapor. At the first stage of the process, the position of the piston separating the intermediate heat reservoir from the engine is fixed, the system is thermally insulated from the heater, and thermal contact is established between the saturated vapor and the engine gas enclosed between the fixed and working pistons. As a result of the expansion of this gas accompanied by the production of work by means of the working piston, the vapor is cooled and completely condenses. The temperature of the gas and the liquid is T_1. As a result of adiabatic expansion of the gas filling the other part of the intermediate heat reservoir, its volume is increased almost to the entire volume of the reservoir and the temperature drops to $T_2<T_1$. At the second stage of the process, thermal contact between the engine and the reservoir is broken and the subsequent production of work and expansion of the engine gas proceeds adiabatically as far as temperature T_2. Then, at the third stage thermal contact is established between the engine and the gas part of the heat reservoir, and the engine gas is compressed with the expenditure of work. However, the gas is not compressed to the initial volume, as was assumed in Ref. 1, but as far as the temperature T_1, after which thermal contact is established between all parts of the system, and at the fourth and final stage, compression continues as far as the initial volume. As a result, all the stored cold created at the first stage of the process is utilized to cool the engine gas.

Since the gas fills the entire volume of the heat reservoir at the end of the first stage, its heating to temperature T_1 takes place at constant volume. Thus the influence of thermal contact with this gas on the compression behavior of the engine gas amounts to a corresponding increase in the spe-

cific heat of this gas at constant volume. As a result of the establishment of thermal contact between all parts of the system at temperature T_1, the specific heat of the liquid is also added to that of the gas. Since the saturated vapor pressure at temperature T_1 is equal to the pressure of the gas filling the entire volume of the heat reservoir at temperature T_2, the compression of the gas following the establishment of thermal contact between all parts of the system will initially take place with the quantity of liquid phase kept constant. However, heating causes the saturated vapor pressure to increase more rapidly than the gas pressure at constant volume. Thus the liquid phase begins to vaporize soon after reaching the temperature T_1. For $q_q/T_0 \gg 1$ and comparable masses of gas and two-phase system in the intermediate heat reservoir, most of the stored cold is concentrated in the liquid phase and is released as the latter vaporizes. This is observed particularly clearly if the number N_2 of gas molecules in the reservoir is considerably lower than the number N_1 of molecules in the two-phase system.

However, for any mass ratios in all three parts of the converter, return of the engine gas to the initial volume causes the temperature of all the parts to return to its initial value. This is because all the stages of the process are reversible and heat exchange between the different parts of the system takes place under equilibrium conditions. Although we cannot talk of the entropy of a nonintegrable system, each part of the system possesses its own entropy. At the final stage of the process and in the initial state, the system is thermally uniform and its entropy is equal to the sum of the entropies of its parts. Since the sum of the entropies of all the parts of the system is conserved in a reversible adiabatic process, when the volume of the engine returns to its initial value the temperature also returns to its initial value.

The work done when the engine gas expands is obviously exactly equal to the work expended on its compression. Any reduction in the work expended on compression reduces the energy and final temperature of the system. The work expended on returning the working piston to its initial state may be reduced by decreasing the volume of the intermediate heat reservoir and thus increasing the volume of the engine as a result of compression.

After equal pressures have been achieved in all parts of the system by compression of the engine gas, the previously fixed piston separating the intermediate heat reservoir from the engine may be released. As a result, the compressibility of the system is increased, and when the working piston returns to its initial position, the volume of the engine will be greater than its initial value and the volume of the reservoir will be smaller. In this case, conservation of the total entropy of the system parts does not result in the system temperature being equal to its initial value. The work expended on compression is necessarily reduced and return of the working piston to its initial state will cause the temperature and pressure in the system to be lower than their initial values. The initial volumes of the system parts and the temperature and pressure therein are restored by the establishment of thermal contact between all parts of the system and a constant temperature bath.

However, whereas the previously analyzed cycle with a fixed volume of intermediate heat reservoir and return to the initial temperature can be achieved for any ratios of material mass in the different parts of the system, a cycle with cooling of the system achieved by return of the working piston to its initial state imposes constraints on the system parameters. Although total condensation of the vapor at the first stage of the process can be achieved for an arbitrarily small mass of gas in the engine by means of a sufficiently large increase in its volume, in this case the gas pressure in the engine will be so low that equalization of the pressures in the system to attain the initial volume of the engine will prove impossible. However subject to the condition

$$P(T_1,N,N_1,N_2) > \frac{N_2 T_1}{V_1}, \tag{2}$$

which is certainly satisfied for fairly large N ($N_2 \ll N_1 \ll N$), the pressures in the system are equalized at the third stage of the cycle. Here $P(T_1,N,N_1,N_2)$ is the pressure in the engine at the end of the first stage and N is the number of molecules in the engine. Return of the system to the initial state is accompanied by redetermination of the entropy.

If the volume of the intermediate heat reservoir changes during the conversion of heat into work, the engine cannot be clearly separated from that part of the system involved only in the heat exchange process. Not only the parameters of the individual parts of the system but also its overall structure change in the course of the process. Thus a graphical plot of the thermodynamic diagram in terms of two variables is not strictly speaking permissible.

The author would like to thank V. I. Perel' for stimulating discussions.

[1] G. V. Skornyakov, Pis'ma Zh. Tekh. Fiz. **21**(23), 1 (1995) [Tech. Phys. Lett. **22**, 949 (1995)].

Translated by R. M. Durham

Electrical characteristics of thin-film emitters with excitation of electroluminescence by an ac voltage

M. K. Samokhvalov

Ulyanovsk State Technical University
(Submitted October 22, 1996)
Pis'ma Zh. Tekh. Fiz. **23**, 1–4 (March 26, 1997)

A study is made of the electrical characteristics of multilayer structures and the effect on them due to the properties of the materials, the design of the device, and the parameters of the excitation voltage. Expressions are derived from which one can estimate the dependence of the electrical characteristics of thin-film electroluminescent emitters on the excitation conditions, the construction of the capacitor, and the properties of the phosphor–insulator interface. © *1997 American Institute of Physics.* [S1063-7850(97)01803-X]

Thin-film electroluminescent metal–insulator–phosphor–insulator structures with a transparent electrode, operating with an ac voltage, are among the most promising display devices. To discover the best conditions for excitation of the electroluminescence and work out circuits for controlling display devices it is necessary to study the electrical characteristics of multilayer structures, and the effect on them due to the properties of the material and construction of the device, and the parameters of the excitation voltage.

The field-effect mechanism for generating free charge carriers in the phosphor layer (ordinarily a high-resistivity wide-gap semiconductor) in a strong electric field makes for a high rate of the electronic processes.[1] Experimental investigations have shown that the rate of change of the characteristics of the electroluminescent capacitors is determined by the rate of change of the external voltage.[2] An electric field is generated in the phosphor higher than that for the onset of field emission. The cause is the self-screening effect, which produces quasi-steady-state conditions.[3] The self-screening effect involves a reduction of the electric field in the region of generation as a result of its screening by the charge created by field emission. The quasi-steady-state screening occurs when the rate of change of the external field equilibrates with the rate of generation of free carriers. To study the general behavior of the quasi-steady-state electronic processes it is necessary to determine the dependence of the electron flux and of the field in the phosphor on the form of the excitation voltage.

Charge carriers are generated in the phosphor layer by tunneling field emission of electrons from states of the phosphor–insulator interface into the conduction band of the semiconductor.[4] Therefore the current flowing in the phosphor layer at voltages corresponding to the excitation of the electroluminescence can be expressed as

$$j_L = \frac{Q_n}{\tau}\exp\left(-\frac{\gamma}{E_{LT}}\right), \tag{1}$$

where Q_n is the charge density of the states at the phosphor–insulator interface, τ is the time constant for recharging of the interface states, E_{LT} is the steady-state electric field in the phosphor for given conditions of electroluminescence excitation, $\gamma=(4\sqrt{2m^*\varphi_t})/3eh$ is the transmission coefficient of the (triangular) potential barrier,[1] e and m^* are the electron charge and effective mass, φ_t is the distance of the surface traps below the bottom of the conduction band of the semiconductor, and h is Planck's constant.

Under operating conditions the total current through the thin-film structure is equal to the conduction current in the phosphor layer under quasi-steady-state conditions of self-screening plus the charge current associated with the capacitance of the insulating layers:[2]

$$J_L = C_D\frac{dV}{dt}, \tag{2}$$

where C_D is the capacitance of the insulating layer and V is the applied voltage.

From relations (1) and (2) we can derive an expression for the threshold electric field in the luminescent layer:

$$E_{LT} = \frac{\gamma}{\ln[Q_n/(\tau C_D dV/dt)]}. \tag{3}$$

It follows that a high rate of change of the voltage corresponds to higher electric fields in the phosphor film. As the frequency of the excitation voltage increases, the threshold voltage corresponding to the onset of emission from the thin film emitter also increases.

In an analysis of the equivalent circuit of the thin-film electroluminescent emitter the electrical properties of the phosphor, which for low voltages are characterized by the capacitance, which is the geometric capacitance of the luminescent film, and at high voltages by an active resistance R_L (Ref. 4). From relations (2) and (3) we can derive an expression to calculate the resistance of the phosphor in the equivalent circuit for a voltage above the threshold value:

$$R_L = \frac{E_{LT}d_L}{C_d(dV/dt)} = \frac{\gamma d_L}{C_D(dV/dt)\ln[Q_n/(C_D dV/dt)]}. \tag{4}$$

For a linearly varying voltage the resistance R_L for a constant rate of sweep will be constant, while for a sinusoidal sweep the resistance will increases with increasing voltage from the threshold to the peak value. The resistances

R_L determined from the experimental measurements varied from 100 to 10 kΩ for an increase in the rate of linear sweep from 10^5 to 10^7 V/s.

The expression for the electrical power dissipated in the phosphor film of the electroluminescent capacitor due to a conduction current under the operating conditions can be written as

$$P_L = J_L \cdot E_{LT} \cdot d_L = \frac{\gamma \cdot d_L \cdot C_D \cdot dV/dt}{\ln[Q_n/(\tau \cdot C_D \cdot dV/dt)]}. \quad (5)$$

Since the electric field is constant under quasi-steady-state conditions of self-screening of the phosphor in a thin-film electroluminescent capacitor, the kinetics of the change of the dissipated power is mainly determined by the time dependence of the conduction current in the phosphor.

The relations derived here allow one to determine how the electrical characteristics (j_L, E_{LT}, R_L, and P_L) of thin-film electroluminescent radiation sources depend on the excitation conditions (dV/dt), the construction of the multilayer capacitor (C_D, d_L), and the properties of the phosphor–insulator interface (γ, τ, and Q_n).

[1] D. H. Smith, J. Lumin. **23**, 209 (1981).
[2] M. K. Samokhvalov, Pis'ma Zh. Tekh. Fiz. **20**(6), 67 (1994) [Tech. Phys. Lett. **20**, 246 (1994)].
[3] N. F. Kovtonyuk, *Electronic Elements Based on Semiconductor–Insulator Structures* [in Russian] (Énergiya, Moscow, 1976).
[4] M. K. Samokhvalov, Pis'ma Zh. Tekh. Fiz. **19**(9), 14 (1993) [Tech. Phys. Lett. **19**, 264 (1993)].

Translated by J. R. Anderson

Attenuation of x rays by ultradisperse media

V. A. Artem'ev

State Scientific Research Center for Materials Technology
(Submitted July 25, 1996)
Pis'ma Zh. Tekh. Fiz. **23**, 5–9 (March 26, 1997)

Theoretical estimates are made for the enhancement of the absorption of x rays by ultradisperse media over that by ordinary polycrystalline materials of the same mass thickness. It is concluded that the use of materials based on ultradisperse powders can improve the characteristics of shielding against x rays and thermal neutrons. © *1997 American Institute of Physics.* [S1063-7850(97)01903-4]

1. A new class of materials — ultradisperse media — consisting of an ensemble of particles smaller than 0.1 μm in size have unique thermal, mechanical, magnetic, and other properties.[1] However, the interaction of ionizing radiation with ultradisperse media has scarcely been studied.[2]

In the description of the propagation of x rays in matter three main mechanisms are taken into account: photoelectric absorption and coherent and incoherent scattering by atoms.[3] Because the particle size in ultradisperse media ($\sim$ 2–10 nm) (Refs. 1 and 2) is commensurate with the wavelength λ of the ionizing radiation ($\sim$ 0.1 nm), coherent scattering of the x rays by the ultradisperse particles is possible, which can be considered as a distinct mechanism for the interaction of x rays with ultradisperse media in addition to the three mentioned above. The effective single-scattering angle θ_1 of photons by irregularities of size a is $\theta_1 \sim \lambda/a \ll 1$ (Ref. 4). After being scattered by N randomly located irregularities the angle of inclination of the radiation from the initial direction, $\theta_N \sim \theta_1 N^{1/2}$, can become large if there is a high concentration of scatterers. Coherent scattering of x rays by ultradisperse particles increases the optical path length of photons in the ultradisperse medium and results in additional absorption over that for ordinary polycrystalline samples.

The present work gives a theoretical estimate of the difference between the attenuation of x rays by an ultradisperse medium and by the ordinary polycrystalline material in which the size of the individual grains is $\sim 10^2$ μm (Ref. 5).

2. For clarity we shall make some simplifying assumptions. It is assumed that the ultradisperse medium is in the form of a plane-parallel plate with a thickness L, which contains identical spherical particles of radius a, held in place by a nonabsorbing and nonscattering binder (Fig. 1). This model realistically describes various ultradisperse media such as bulk ultradisperse powder, powder of a heavy metal (W, Pb, etc.) compacted by a polymer binder, or an aerosol in the atmosphere. A radiation flux with a wavelength λ impinges perpendicularly on the surface of the plate. We shall consider only two mechanisms of interaction of the photons with matter: atomic photoabsorption and small-angle elastic coherent scattering of photons by the ultradisperse particles (this will give a lower estimate for the difference). We denote by N_{scat} the concentration of particles in the ultradisperse media. Using the fact that θ_1 is small, we write the transport equation for the radiation in differential form[4]

$$\mu \frac{\partial I(z,\mu)}{\partial z} = -\sum_{\Phi} I(z,\mu) + \frac{\langle \theta_s^2 \rangle}{4} \left\{ \frac{\partial}{\partial \mu}(1-\mu^2) \frac{\partial I(z,\mu)}{\partial \mu} \right\}, \tag{1}$$

where $I(z,\mu)$ is the flux density of photons with a direction of propagation Ω at a given depth z; $\mu = \mathbf{\Omega} \cdot \mathbf{\Omega} = \cos\theta$; $\mathbf{\Omega}'$ and $\mathbf{\Omega}$ are the unit vectors of the photon velocity before and after scattering, Σ_Φ is the attenuation coefficient due to photoabsorption, $\langle \theta_s^2 \rangle = 2\pi \int_0^\pi \theta'^3 w(\theta') d\theta'$, and $w(\theta') = N_{\text{scat}} d\sigma(\theta')$ is the probability of scattering a photon by an angle $\theta' = \cos^{-1}(\mathbf{\Omega}' \cdot \mathbf{\Omega})$ per unit path length, $d\sigma = 0.5(e^2 n/mc^2)^2 (1+\cos^2\theta') |\int dV' \exp(-i\mathbf{q}\cdot\mathbf{r}')|^2 d\Omega$ is the cross section for coherent elastic scattering of a photon by an ultradisperse particle, e and m are the electron charge and mass, c is the speed of light, n is the total electron density of the material, $\mathbf{q} = \mathbf{k} - \mathbf{k}'$, and $\mathbf{k}'$ and $\mathbf{k}$ are the wave vectors of the photon before and after scattering and the integration is carried out over the volume of the ultradisperse particle. Using the relation $ka \gg 1$, we find

$$\langle \theta_S^2 \rangle \cong \pi N_{\text{scat}} (ka)^{-4} \times (4\pi r_e Z n_{at} a^3)^2 \times [\ln(4ka) + \gamma - 1],$$

where $k = 2\pi/\lambda$, $r_e = e^2/mc^2 \simeq 2.82 \times 10^{-13}$ cm is the classical electron radius, Z and n_{at} are the atomic number and the concentration of atoms of the ultradisperse particle material, and $\gamma = 0.5772\ldots$.

Assuming that the thickness L is such that the probability that a photon will be deflected by a large angle θ is small, we obtain[4] the solution of Eq. (1) in the diffusion approximation

$$I(z,\theta) \cong I_0 \exp\left(-\sum_{\Phi} z \right) (\pi z \langle \theta_s^2 \rangle)^{-1} \times \exp\left\{ -\left[0.5 \sum_{\Phi} z + (z\langle \theta_s^2 \rangle)^{-1} \right] \theta^2 \right\}.$$

Integrating $I(z,\theta)$ over all angles to determine the photon flux density at depth z regardless of the direction of motion, we find $I(z) - I_0 \exp(-\Sigma_\Phi z)(1 + 0.5\langle \theta_s^2 \rangle \Sigma_\Phi z^2)^{-1}$.

We now introduce the coefficient β, which denotes the excess factor by which the x-ray beam is attenuated after passing through the ultradisperse media as compared with an ordinary polycrystalline sample of the same thickness. In this model the attenuation of the x rays by the ordinary sample

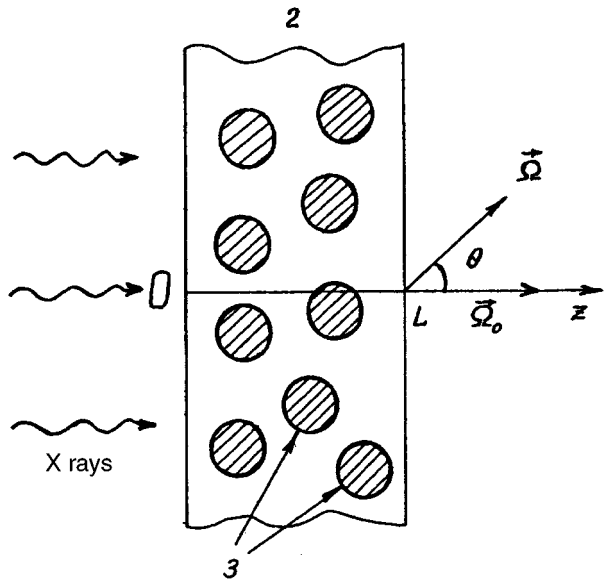

FIG. 1. *1*—x rays, *2*—ultradisperse media, *3*—ultradisperse particles.

will be $I^*(z)=I_0\exp(-\Sigma_\Phi z)$, so that $\beta=I^*(z)/I(z)=1+0.5\langle\theta_s^2\rangle\Sigma_\Phi z^2$. Again it should be noted: our approximation gives a lower limit on β.

3. Let us make a numerical estimate of β for $\lambda = 0.1$ nm as a function of the size of the ultradisperse tungsten particles. We assume a monodisperse powder compacted in a plate of thickness $L=1$ mm (Fig. 1), which has as mass thickness equivalent to a 0.5 mm plate of ordinary polycrystalline tungsten. For 10 nm particles we have a concentration $N_{\text{scat}}=10^{18}$ cm^{-3}; for 6 nm particles $N_{\text{scat}}=4.6\times10^{18}$ cm^{-3}, and for 3 nm particles $N_{\text{scat}}=3.7\times10^{18}$ cm^{-3}. Using the photoabsorption data from Ref. 6, we obtain $\beta = 1.2$, 1.3, and 1.5, respectively, for the three ultradisperse particle sizes. Thus the use of materials in an ultradisperse state increases their shielding properties by tens of per cent and more, which is in accord with experimental data.[7–9]

4. The attenuation of *x* rays in ultradisperse media by the mechanism of coherent scattering of photons by the ultradisperse particles is in addition to all the existing mechanisms of coherent and incoherent scattering of radiation by atoms of the material, and all the foregoing discussion also applies to ordinary polycrystalline materials. However, since the average grain size D in a polycrystalline sample is $\sim10^2$ μm (for example, D in Al and W are 80 and 60 μm, respectively),[5] and the angle of coherent scattering of photons from individual grains ($\sim\lambda/D$), and the concentration of grains (N_{scat}) are much smaller than in an ultradisperse medium (for samples with the same mass thickness). Therefore β for ordinary polycrystalline materials is essentially unity compared to material having a completely disordered (amorphous) structure.

In conclusion it should be mentioned that ultradisperse media may also be more effective shields for thermal neutrons with wavelengths ~0.1 nm and greater.

[1] I. D. Morokhov, L. I. Trusov, and S. P. Chizhik, *Ultradisperse Metal Media* [in Russian] (Atomizdat, Moscow, 1979).
[2] I. D. Morokhov, L. I. Trusov, and V. N. Lapovok, *Physical Phenomena in Ultradisperse Media* [in Russian] (Énergoatomizdat, Moscow, 1984).
[3] K. N. Mukhin, *Experimental Nuclear Physics*, Vol. 1 (Énergoatomizdat, Moscow, 1983).
[4] N. P. Kalashnikov, V. S. Remizovich, and M. I. Ryazanov, *Collisions of Fast Charged Particles in Solids* [in Russian] (Énergoatomizdat, Moscow, 1980).
[5] Ya. S. Umanskiĭ, B. N. Finkel'shteĭn, M. E. Blanter *et al.*, in *Physical Metallurgy* [in Russian] (Metallurgizdat, Moscow, 1955).
[6] *Handbook of Physical Quantities* [in Russian] edited by I. S. Grigor'ev and E. Z. Meĭlikhov (Énergoatomizdat, Moscow, 1991).
[7] V. I. Tkachenko, V. A. Yupenkov, Yu. A. Krikin *et al.*, Bulletin VAK, Russian Federation, 1994, Nos. 5,6, p. 44.
[8] V. A. Artem'ev, S. V. Chuklyaev, Yu. A. Kurakin *et al.*, At. Énerg. **78**(3), 186 (1995).
[9] S. V. Chuklyaev, M. Ya. Grudskiĭ, and V. A. Artem'ev, *Secondary-Emission Detectors of Ionizing Radiation* [in Russian] (Énergoatomizdat, Moscow, 1995).

Translated by J. R. Anderson

Two-section InGaAsP/InP Fabry-Perot laser with a 12 nm tuning range

N. A. Pikhtin, A. Yu. Leshko, A. V. Lyutetskiĭ, V. B. Khalfin, N. V. Shuvalova, Yu. V. Il'in, and I. S. Tarasov

A. F. Ioffe Physicotechnical Institute, Russian Academy of Sciences, St. Petersburg
(Submitted December 17, 1996)
Pis'ma Zh. Tekh. Fiz. **23**, 10–15 (March 26, 1997)

Wavelength tuning over a 12 nm range is obtained for a two-section InGaAsP/InP Fabry-Perot laser ($\lambda=1.55$ μm). The method used to vary the gain profile of the laser allows one to predict the range of possible wavelength tuning. © *1997 American Institute of Physics.* [S1063-7850(97)02003-X]

Tunable semiconductor lasers that lase in the wavelength range 1.3–1.55 μm are irreplaceable sources of coherent optical communication lines, optical frequency-division multiplexing systems, and also for gas-analysis devices. Moreover, the absorption wavelength of many molecules lies near 1.55 μm.

There are several methods of tuning the wavelength of a semiconductor laser. Electrical tuning is one of the most simple and reliable. In most cases a multisection laser is used for this purpose.[1] The possibility of wavelength tuning of a multisection Fabry-Perot laser having a high optical power is of definite interest.

In this investigation we have studied the wavelength tuning of the radiation from a two-section Fabry-Perot heterolaser fabricated on the basis of InGaAsP/InP quantum-well separate-confinement double heterostructure ($\lambda=1.55$ μm). The use of this type of heterostructure with an active layer thickness 100–20 Å in lasers of the ''small-mesa'' type provides highly reliable single-mode lasers with a high output power.[2] As mentioned previously,[3] lasers of this design have an anomalously wide lasing and spontaneous emission spectrum. A wide gain profile permits tuning of the wavelength in these lasers over a wide range.[4]

To prepare the two-section laser, an isolating groove was formed on the heterostructures by means of photolithography and plasmachemical etching. The width and depth of the groove were 5 and 3 μm, respectively. The resistance between the sections of the laser was 0.5 kΩ. The lasers were mounted on a heat sink with the flat side up, and were measured in pulsed and cw operation. Figure 1 shows a diagram of the two-section laser.

In Fig. 2 we show the lasing spectrum of the InGaAsP/InP two-section laser ($\lambda=1.55$ μm) for various ratios of the pump currents through sections *1* and *2*, of length $L_1=300$ μm and $L_2=100$ μm, respectively. The maximum wavelength shift was found to be 12 nm for the maximum attainable current density J_1 through section *1* and correspondingly the minimum current through section *2*. It must be emphasized that the radiated power of the two-section laser was maintained constant at 5 mW. At this power the laser lases on one longitudinal mode, corresponding in wavelength with the threshold value. This amount of tuning can be explained by a change in the position of the maximum total gain ($G(\lambda)$) of the two-section laser when the pump current ratio of its sections is varied.

To account for the experiment and to estimate the maximum tuning range in the two-section laser, we measured the gain spectrum $g(\lambda)$ as a function of the current density. For this purpose we used a method we have modified for determining the gain from the spontaneous emission spectrum. Measurements were carried out for the spontaneous emission spectrum of the two sections of the two-section laser for various pump currents. The two sections were of quite quite different lengths. The spontaneous emission was observed at the outputs from the end of one of the sections, while the other section of the laser was operated back-biased. Naturally, the emission intensity did not depend on the reverse bias on the other section of the laser. In this case the emission intensity $I(\lambda)$ from the end of the section of length L is given by the following expression

$$I(\lambda)\sim\frac{\{\exp[g(\lambda)*L]-1\}*R(J,\lambda)}{g(\lambda)} \tag{1}$$

where $R(J,\lambda)$ is the local intensity of spontaneous emission, which we shall assume is uniform over the length of the section.

The ratio of the emission intensities for the two ends, $I_1(\lambda)$ and $I_2(\lambda)$, takes the form

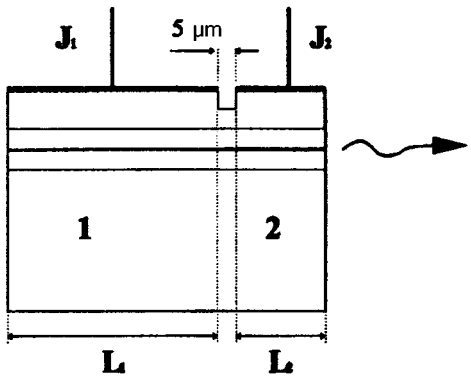

FIG. 1. Diagram of the two-section Fabry-Perot InGaAsP/InP laser ($\lambda=1.55$ μm).

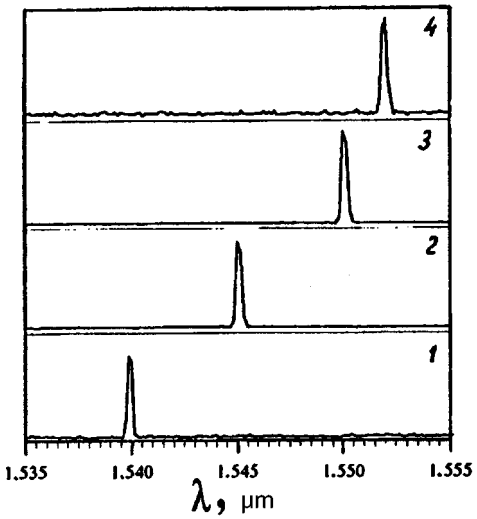

FIG. 2. Emission spectrum of the two-section InGaAsP/InP laser for a constant emission power $P=$ 5 mW and various current densities J_1 and J_2 through sections *1* and *2*, respectively: *1* — J_1=3 kA/cm^2, J_2=3 kA/cm^2; *2* — J_1=5 kA/cm^2, J_2=2 kA/cm^2; *3* — J_1=7 kA/cm^2, J_2=1.5 kA/cm^2; *4* – J_1=10 kA/cm^2, J_2=1 kA/cm^2.

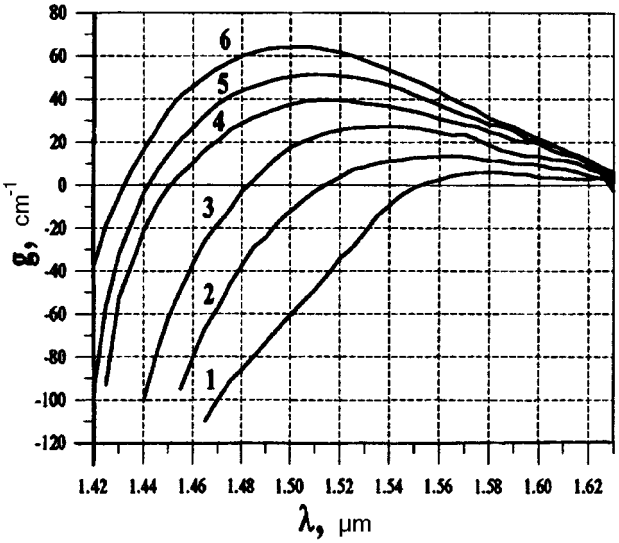

FIG. 3. Measured gain spectrum of an InGaAsP/InP laser diode for various pump current densities: *1* — J=1 kA/cm^2; *2* — J=2 kA/cm^2; *3* — J=3 kA/cm^2; *4* — J=5 kA/cm^2; *5* — J=7 kA/cm^2; *6* — J=10 kA/cm^2.

$$r(\lambda)=\frac{I_1(\lambda)}{I_2(\lambda)}=\frac{\exp[g(\lambda)L_1]-1}{\exp[g(\lambda)L_2]-1}. \qquad (2)$$

For normalizing $I_1(\lambda)$ and $I_2(\lambda)$ the spontaneous emission spectra were matched at short wavelengths, where $\exp(g(\lambda)L)\ll 1$, and consequently $I_1(\lambda)=I_2(\lambda)$.

The gain spectra calculated from formula (2) from the measured spontaneous emission spectra for various pump current densities J in the wavelength range important for tuning are shown in Fig. 3. The experiments carried out with samples with a different ratio of the lengths of the sections give the same results. The error in the determination of the gain is not higher than 10%.

Since the measurements were made for pump currents not much above threshold, we did not take into account the effect of the optical power on the gain spectrum. Therefore the net gain profile $G(\lambda)$ of a two-section laser is given by the expression

$$G(\lambda)\sim\exp[g_1(\lambda)L_1+g_2(\lambda)L_2], \qquad (3)$$

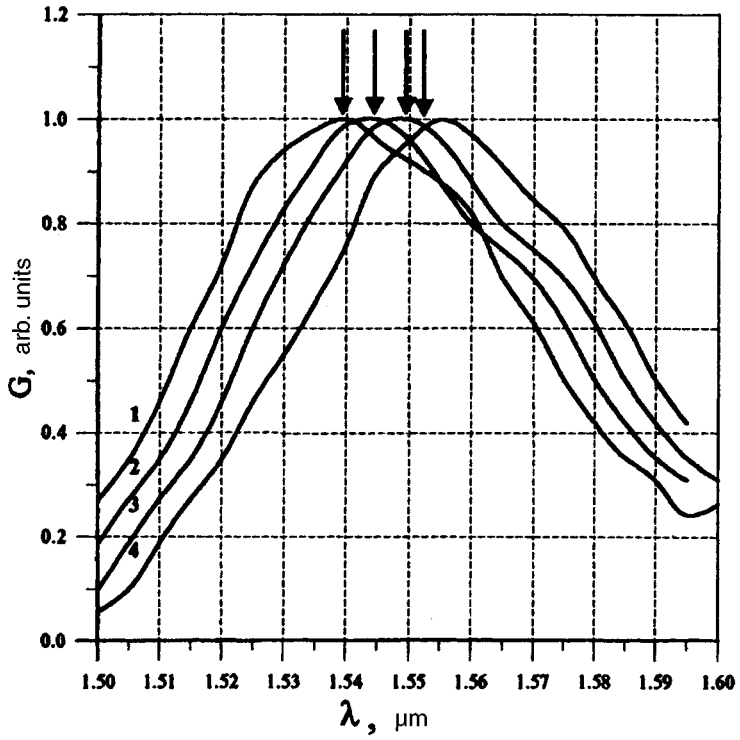

FIG. 4. Total gain profile of a two-section InGaAsP/InP laser with the pump current densities listed in Fig. 2. The arrows show the measured lasing wavelength for each combination of currents: *1* — J_1=3 kA/cm^2, J_2=3 kA/cm^2; *2* — J_1=5 kA/cm^2, J_2=2 kA/cm^2; *3* — J_1=7 kA/cm^2, J_2=1.5 kA/cm^2; *4* — J_1=10 kA/cm^2, J_2=1 kA/cm^2.

where $g_1(\lambda)$ is the gain for a current density J_1 through section *1* and $g_2(\lambda)$ is the gain for a current density J_2 through section *2*.

In Fig. 4 we show the calculated dependence of the total gain for the InGaAsP/InP two-section heterolaser with section lengths $L_1=300$ μm and $L_2=100$ μm for the current densities through the laser sections as listed in Fig. 2. It can be seen that the maximum in the total gain curve is in good agreement with the experimentally determined lasing wavelengths for those current densities through the section.

To summarize, we have obtained a tuning range of 12 nm while maintaining the radiated optical power in a two-section Fabry-Perot InGaAsP/InP laser ($\lambda=1.55$ μm) based on a single-mode InGaAsP/InP structure with a thin active region. The proposed method of measuring the gain profile in the two-section laser is well-justified by experiment. The measured $g(J,\lambda)$ curve will be used in the future for calculating the optimal ratios of the section lengths and of the pump currents in order to broaden the tuning range.

In conclusion, the authors would like to thank N. D. Il'inskaya, T. N. Drokina, and E. I. Kukhareva, for assistance in preparing the samples, and also S. F. Kharlapenko for assistance in the computer analysis of the results, and Zh. I. Alferov for his steady interest in this work.

[1] H. Hillmer, A. Grabmaier, S. Hansmann, H. -L. Zhu, H. Burkhard, and K. Mazagi, IEEE J. of Selected Topics in Quant. Electr. **1**, 356 (1995).
[2] M. A. Ivanov, Yu. V. Il'in, N. D. Il'inskaya, Yu. A. Korsakova, A. Yu. Leshko, A. V. Lunev, A. V. Lyuteskiĭ, A. V. Murashova, N. A. Pikhtin, and I. S. Tarasov, Pis'ma Zh. Tekh. Fiz. **21**(5), 70 (1995) [Tech. Phys. Lett. **21**, 198 (1995)].
[3] N. A. Pikhtin, I. S. Tarasov, and M. A. Ivanov, Fiz. Tekh. Poluprovodn. **28**, 1983 (1994) [Semiconductors **28**, 1094 (1994)].
[4] D. Huhse, M. Schell, J. Kaessner, D. Bimberg, I. S. Tarasov, A. V. Gorbachov, and D. Z. Garbuzov, Electron. Lett. **30**, 157 (1994).

Translated by J. R. Anderson

Degenerate four-wave mixing spectroscopy excited by ultrashort laser pulses

A. O. Morozov, Yu. A. Golikov, and I. E. Mazets

M. V. Lomonosov St. Petersburg State Technical University
A. F. Ioffe Physicotechnical Institute, Russian Academy of Sciences, St. Petersburg
(Submitted December 17, 1996)
Pis'ma Zh. Tekh. Fiz. **23**, 16–19 (March 26, 1997)

A new method is described for spectroscopic diagnostics of combustion and explosion products, which makes it possible to study processes occurring at short times in hot and dense molecular gases. [S1063-7850(97)02103-4]

The physics of processes associated with degenerate four-wave mixing (DFWM) in nonlinear media has been actively studied in connection with the potential diagnostics capabilities inherent in this interaction. These capabilities stem from the resonance nature of the interaction, which makes possible highly sensitive and selective measurements, and also from the conjugate nature of the signal wave, which opens up new possibilities for obtaining images of objects and spatial measurements without scanning.[1,2] These capabilities of DFWM in a number of cases allows this method to compete with and even surpass such powerful spectroscopic methods as coherent anti-Stokes scattering (CARS) and laser-induced fluorescence, which allows measurements in the region of high pressures and temperatures.[2] In addition, the useful information on the sample with DFWM is extracted from the spectrum of the signal wave, which is usually obtained by scanning the narrow line of a tunable laser. This circumstance inhibits the study of highly transient objects, for example, processes associated with combustion and explosions at comparatively high pressures. To record the spectra of the signal wave in a single laser pulse, it has been proposed[3,4] that a ''broad-band modeless laser'' be used, or more precisely, a pulse of radiation amplified in a homogeneously broadened inversion medium. However, the amplitude and phase distribution in the spectrum of a single pulse of this sort of radiation has a random nature, and is not reproducible from pulse to pulse, which adds difficulties to the interpretation of the results.

In this paper we propose a new method of spectroscopic diagnostics of combustion and explosion products, based on the use of ultrashort picosecond and femtosecond laser pulses with DFWM to generate the spectrum of the signal wave. These pulses by their nature have a regular amplitude and phase distribution in the spectrum, which simplifies the theoretical model and makes it possible to take an instantaneous ''snapshot'' of the population distribution over the vibrational-rotational states of the molecules at selected points within the sample (for example the flame of a burner). Reliable data are also provided by individual measurements in a single laser pulse, without averaging over a statistical ensemble of such spectra. Another advantage in the use of these pulses with DFWM may be separation of the contributions to the signal wave at the primary and secondary gratings, and the related possibility of studying relaxation processes, energy transport processes, molecular kinetics, etc. This favorable property is due to the fact that the duration of a picosecond pulse, and even more so, a femtosecond pulse, is considerably shorter than the phase and energy relaxation times in the gases, even at high pressures and temperatures.

Experiments on four-wave phase conjugation and DFWM in the picosecond range have been carried out previously for condensed media[5–7] and were limited to the observation of the conjugated signal wave and measurements of its energy and time parameters. No measurements or calculations have been carried out regarding the spectral aspects of the interaction of ultrashort laser pulses with molecular gases with DFWM. However, the solution of this problem will promote considerable progress in the spectroscopic diagnostics of flames and will contribute to the understanding of the physical nature of the fast nonequilibrium kinetic processes occurring in them.

For a theoretical analysis, the most simple case is that of unsaturated transitions, where the product of the maximum Rabi frequency, which characterizes the interaction of the molecule with the laser pulse, times the pulse length is much less than unity, i. e., when perturbation theory is applicable. Moreover, at short times we may neglect relaxation processes, i. e., the vector states formalism can be used.

We denote by the numbers 1 and 2 the pump pulses, and 3 is the probe pulse, which initiates the DFWM signal (the fourth wave). The relation between the wave vectors of the waves has the form[1]

$$\mathbf{k}_1+\mathbf{k}_3=\mathbf{k}_2+\mathbf{k}_4\,. \tag{1}$$

We assume that the wave vectors lie in a common plane and the light is linearly polarized perpendicular to that plane. The simplest spectra to interpret are obtained if the pulses 1, 2, and 3 do not overlap in time, but act sequentially. All three pulses are obtained from a single initial pulse by means of beam splitters, while the required time delay in the picosecond range is produced by small path differences. Of course, the time intervals between the pulses must be short compared to the relaxation times T_1 and T_2 of the medium.

By way of example, we calculated the relative intensities $I_J^{(Q)}$ of the lines of the Q branch of the vibrational band of the transition between the ground state $^1\Sigma^+$ and the excited state $^1\Pi$ of the heteronuclear diatomic molecule

$$J_J^{(Q)} = \text{const} \cdot w_J \cdot \frac{1}{[J(J+1)]^4} \times \sum_{M=1}^{J} M^8 \cdot S_1(\omega_J) S_2(\omega_J) S_3(\omega_J), \quad (2)$$

where $S_i(\omega_J)$ is the spectral intensity of the ith mode at the frequency ω_J of this transition, J is the rotational quantum number (identical for the initial and final states), w_J is the population of the Zeemann sublevels of the initial state (it is assumed that the medium is isotropic and that w_J does not depend on the projection of the angular momentum). The expressions for the dipole moments of the transitions were taken from Ref. 8. In the derivation of Eq. (2) it was assumed that the width of the spectrum $S_i(\omega_J)$ is much smaller than the vibration frequency of the molecule, so that we can neglect interference of the channels of excitation of DFWN with different intermediate vibrational states.

It should be emphasized that in Eq. (2) all the values of w_j refer to the same instant of time, when an instantaneous snapshot of the state of the medium is taken with a single ultrashort pulse. This is how our method differs from the method of slow scanning of the frequency of a laser with a narrow spectrum. Moreover, methods exist whereby one can obtain nearly 100% reproducibility in the spectra of the ultrashort pulses.[9] Consequently in our case the instantaneous populations of the rotational states can in principle be found from the results of individual measurements corresponding to the same laser pulse.

The authors wish to expression their gratitude to Prof. Yu. A. Tolmanchev and Prof. T. Neger for helpful discussions.

[1] H. J. Eicher, P. Gunter, and D. W. Pohe, in *Laser-Induced Dynamic Gratings*, Springer-Series in Optical Sciences (Springer-Verlag Berlin, 1986).
[2] R. L. Farow and D. J. Rakestraw, Science **256**, 1894 (1992).
[3] D. R. Meacher, P. G. R. Smith, P. Ewart, and J. Cooper, Phys. Rev. A **46**, 2718 (1992).
[4] P. G. R. Smith and P. Ewart, Phys. Rev. A **54**, 2347 (1996).
[5] J. L. Ferrier, Z. Wu, X. Nguyen Phu, and G. Rivoire, Opt. Commun. **41**, 207 (1982).
[6] N. S. Vorobiev, I. S. Ruddock, and R. Illingworth, Opt. Commun. **41**, 216 (1982).
[7] H, Coic, M. L. Roblin, F. Gires, and R. Grousson, J. Opt. Soc. Amer. B **11**, 2232 (1994).
[8] L. D. Landau and E. M. Lifshitz, *Quantum Mechanics: Non-Relativisic Theory*, 3rd ed. (Pergamon Press, Oxford, 1977) [Russ. original 4th ed., Nauka, Moscow, 1989].
[9] K. J. Choi and M. R. Topp, in *Proceedings of the 2nd International Conference on Picosecond Phenomena* (Springer-Verlag, Berlin, 1980), pp. 12–16.

The ''negative trapping'' effect in the magnetic-field dependence of absorption in high-temperature superconductors

G. V. Golubnichaya, A. Ya. Kirichenko, and N. T. Cherpak

Institute of Radiophysics and Electronics, Ukrainian National Academy of Sciences, Kharkhov
(Submitted November 21, 1996)
Pis'ma Zh. Tekh. Fiz. **23**, 20–25 (March 26, 1997)

This paper reports the first study of the absorption of an rf electromagnetic field in high-temperature superconducting samples of $YBa_2Cu_3O_{7-x}$ in the range of magnetic fields corresponding to the onset of the ''negative trapping'' effect. It is shown how additional annealing and degradation of the sample influence the onset of the effect. A modification of the model of dynamic interaction of superconducting loops is used to explain the observed phenomena. © *1997 American Institute of Physics.* [S1063-7850(97)02203-9]

The ''negative trapping'' of a magnetic field in $YBa_2Cu_3O_{7-x}$ ceramics observed by Rostami *et al.*[1] appears as a nonmonotonic field dependence of the trapped magnetic flux. It is observed in magnetizing fields H_m below the lower critical magnetic field for the granules, H_{c1g}. Because of the high sensitivity of rf absorption in YBCO ceramics to an external magnetic field, it is a matter of interest to explain how the negative trapping effect affects the rf absorption.

It is well known that qualitatively the magnetic field dependence of the rf absorption $P(H_m)$ in samples with magnetic flux trapping[2,3] correlates fully with the field dependence of the trapped magnetic flux $H_{tr}(H_m)$.[4,5] The plateaus on the curves of $P(H_m)$ are separated by segments where the absorption increases, while on the $H_{tr}(H_m)$ curves the plateaus are separated by segments where H_{tr} increases. The values of H_m corresponding to the end points of the plateau on the two curves coincide, and correspond to the critical fields of the sample.

A typical curve of the magnetic field dependence of the rf absorption measured by the induction method[3] at 2.5 MHz at the boiling point of liquid nitrogen, $T=77$ K, is shown in Fig. 1 (curve *1*). The power P absorbed in the sample normalized to the power P_0 absorbed in the sample without the magnetic field is plotted along the vertical axis. The curve was measured for a ceramic sample prepared from high-quality powder containing at least 95–97% $YBa_2Cu_3O_{7-x}$ by standard hot pressing at $T=580$ °C with annealing in air at $T=930$ °C for 5–6 h. The sample density was $\rho=4.6$ g/cm^3, and the critical current density was $J_c=120$ A/cm^2 at $T=77$ K.

To observe the negative trapping effect, the work reported in Ref. 1 used a special technology. In our case, we used the ordinary technology with higher pressures or longer annealing times and found that the magnetic field dependence of the rf absorption $P(H_m)$ also was nonmonotonic over the regions of magnetizing fields $H_{c1j}\leqslant H_m\leqslant H_{c1g}$ (where H_{c1j} is the lower critical field for the intergranular medium). For example, in Fig. 1 (curve *1*) we show the curve $P(H_m)$ for a higher-density sample, $\rho=5.4$ g/cm^3. The magnetizing field at which the Abrikosov vortices begin to penetrate the granule is the same for both samples, $H_{c1g}=31$ Oe. However, curve *1* (Fig. 2) has a prominent absorption peak in the region $H_{c1j}\leqslant H_m\leqslant H_{c1g}$ and an extended region of reduced loss in the sample from 12 to 30 Oe.

When the sample with the initial density $\rho=4.6$ g/cm^3 was annealed again at $T=930$ °C for 6 h (Fig. 1, curve *2*) and then one more time for 26 h (curve *3*) the magnetic field dependence became nonmonotonic. A noteworthy aspect of these curves is the wide plateau following the absorption peak with increasing H_m, on which the rf loss is essentially the same as the absorption on the plateau before the additional annealing.

Since contact with water or water vapor degrades mainly the intergranular medium,[6] it was important to observe how degradation of the high-T_c ceramic affects the characteristics of the rf absorption $P(H_m)$. When the sample with the initial density $\rho=5.4$ g/cm^3 was exposed to water the rf absorption increased over the entire range of magnetic fields. The nonmonotonic variation of $P(H_m)$ in the range $H_{c1j}\leqslant H_m\leqslant H_{c1g}$ is flattened out. For an example, we have shown in Fig. 2 (curve *2*) the results of measurements of the rf absorption after exposure of the sample to water for 185 h. It can be seen that curve *2* is qualitatively similar to curve *1* in Fig. 1. However, with a regenerating annealing of this sample at $T=930$ °C for 6 h the curve is no longer monotonic (see curve *3* in Fig. 2). It is noteworthy that these operations have a large effect on the value of H_{c1j}, whereas H_{c1g} is scarcely changed.

Hence the segment of the curve $P(H_m)$ corresponding to the onset of the magnetic-field negative trapping effect, which occurs between the magnetizing fields $H_{c1j}\leqslant H_m\leqslant H_{c1g}$, is shifted along the plateau from H_{c1j} to H_{c1g} when the properties of the intergranular medium are changed, while the segments of the plateau are preserved. These investigations on controlling the intergranular links by additional annealing or by degradation support the main tenets of the negative-trapping model, which assumes that the system contains both Josephson weak links belonging to most of the loops, and stronger junctions, belonging to loops of smaller dimensions. However, in contrast to the opinion expressed in Ref. 1, we believe that this effect is due not to the suppression of superconductivity in the large chains by the fields of smaller loops, but simply to the destruction of the larger loops by the fields of Josephson weak links, which are trapped in more stable small loops with increasing H_m.

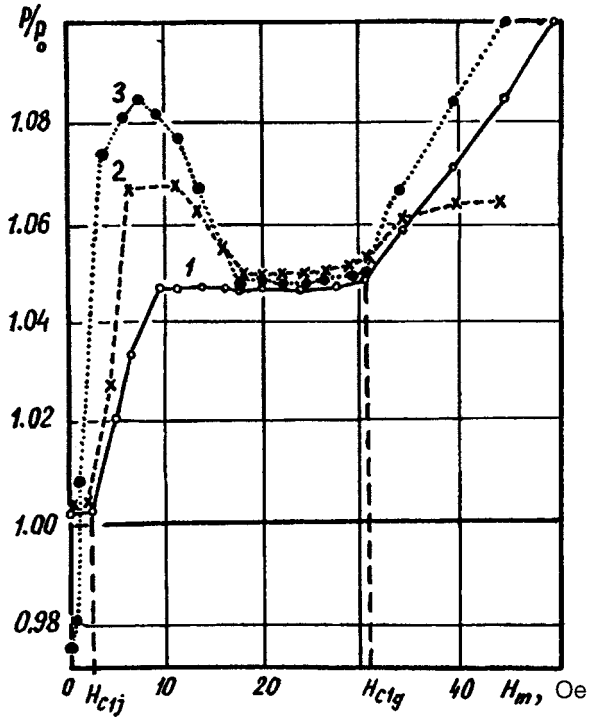

FIG. 1. Relative absorption P/P_0 versus the magnetizing field H_m after additional annealing of the sample: *1* — sample in the initial state, *2* — after additional annealing for 6 h, *3* — after additional annealing for 26 h.

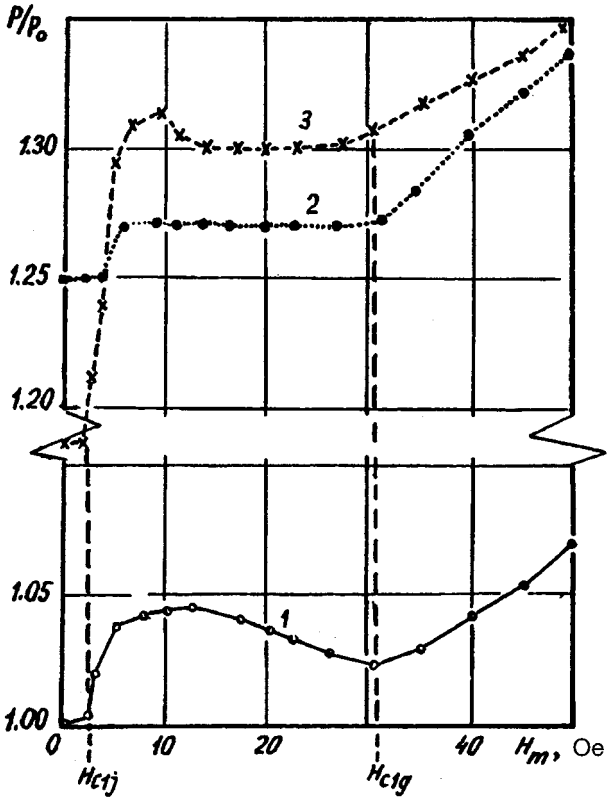

FIG. 2. Relative absorption P/P_0 versus the magnetizing field H_m for the sample: *1* — in the initial state, *2* — after degradation due to contact with water, *3* — after regenerating annealing.

That is, with the trapping of hypervortices in the intergranular medium as the magnetization field increases, two processes occur: a) gradual trapping of the magnetic flux by all the smallest loops and b) the destruction of the larger loops both by the external field and by the fields trapped in the sample. In Ref. 1 it was shown clearly that the field of the trapped magnetic flux near the trapping peak is 3–4 Oe; i. e., it can exceed $H_{c1j} \approx 3$ Oe, characteristic of these samples.

We believe that the additional annealing generates more Josephson links between the granules, but these links are weaker than those between the granules formed when the sample was synthesized. The enhancement of the magnetizing field on the negative trapping section increases the trapped field, facilitating the breaking of large closed loops, which can reduce the general pinning of the magnetic flux. However, thereafter the only trapped magnetic flux fixed in the sample is that in closed loops formed during the standard synthesis before the additional annealing. In this connection, the rf absorption P directly before $H_m = H_{c1g}$ can reach the same level, which is confirmed by the curves in Fig. 1.

With the degradation of the ceramic samples the weakest links are destroyed first. Then the negative trapping effect may disappear.

[1] Kh. R. Rostami, A. A. Sukhanov, and V. V. Mantorov, Fiz. Nizk. Temp. **22**, 58 (1996) [Low Temp. Phys. **22**, 42 (1996)].
[2] A. Ya. Kirichenko and N. T. Cherpak, Pis'ma Zh. Tekh. Fiz. **16**(12), 85 (1990) [Sov. Tech. Phys. Lett. **16**, 476 (1990)].
[3] G. V. Golubnichaya, A. Ya. Kirichenko, N. T. Cherpak, V. T. Zagoskin, Yu. G. Litvinenko, S. V. Lobas, and G. Kh. Rozenberg, Sverkhprovodimost' (KIAE) **5**, 486 (1992) [Superconductivity **5**, 484 (1992)].
[4] Cao Xiaowen, Han Guchang, and Zhang Tingyu, Mod. Phys. Lett. B **1**, 383 (1988).
[5] A. A. Zhukov, D. A. Komarkov, G. Karapetrov, S. N. Gordeev, and R. I. Antonov, Supercond. Sci. Technol. **5**, 338 (1992).
[6] G. V. Golubnichaya, A. Ya. Kirichenko, V. I. Nitsevich, N. T. Cherpak, V. T. Zagoskin, Yu. G. Litvinenko, V. A. Murakhovskiĭ, and Yu. B. Poltoratskiĭ, Sverkhprovodimost' (KIAE) **5**, 348 (1992) [Superconductivity **5**, 348 (1992)].

Translated by J. R. Anderson

Lagrange–Euler description of discontinuous flows of a two-phase reacting medium

Yu. A. Kurakin and A. A. Shmidt

A. F. Ioffe Physicotechnical Institute, Russian Academy of Sciences, St. Petersburg
(Submitted November 29, 1996)
Pis'ma Zh. Tekh. Fiz. **23**, 26–32 (March 26, 1997)

Novel methods for calculating hydrodynamic behavior are used to analyze the propagation of shock waves in two-phase reacting mixtures. New data are reported on the detailed structure of shock-wave two-phase flow, and criteria are proposed to determine the conditions for the initiation of combustion, which is important for explaining the characteristic features of such flows. © *1997 American Institute of Physics.* [S1063-7850(97)02303-3]

We have carried out a numerical analysis of the structure of discontinuous flows of two-phase reacting media, based on the Lagrange–Euler (L–E) description.[1]

The algorithm permits one to analyze interphase transport processes and homogeneous and heterogeneous chemical reactions, in particular, the combustion of disperse inclusions.

1. In the modeling of the motion of the carrier phase (the Euler step of the algorithm), we use the system of Euler equations supplemented by source terms that describe interphase exchange of mass, momentum, and energy, and also describe homogeneous chemical reactions. Using the conventional notation, we write these equations as

$$\frac{\partial \rho}{\partial t}+\frac{\partial \rho u}{\partial x}=-\langle J_{gp}\rangle n_p,$$

$$\frac{\partial \rho u}{\partial t}+\frac{\partial(\rho u^2+p)}{\partial x}=-[\langle F_{gp}\rangle+\langle J_{gp}\cdot V_p\rangle]n_p,$$

$$\frac{\partial e}{\partial t}+\frac{\partial(eu+pu)}{\partial x}=-\left[\langle F_{gp}\cdot V_p\rangle+\langle Q_{gp}\rangle+\left\langle J_{gp}\left(C_p^0\cdot T_p+\frac{V_p^2}{2}\right)\right\rangle\right]n_p,$$

$$\frac{\partial \rho c_i}{\partial t}+\frac{\partial \rho c_i u}{\partial x}=-\langle J_{gp_i}\rangle n_p+W,$$

where $e=C_\nu T+\rho u^2/2$.

2. In the Lagrange–Euler algorithm the evolution of the disperse phase (the Lagrange step of the algorithm) is described by a system of ordinary differential equations of motion of the test particles:

$$\frac{d\mathbf{r}_p}{dt}=\mathbf{V}_p,\quad \frac{dm_p}{dt}=J_{gp},$$

$$\frac{dm_p\mathbf{V}_p}{dt}=\mathbf{F}_{gp},\quad \frac{dC_p^0 m_p T_p}{dt}=Q_{gp}.$$

3. The effect of the disperse phase on the carrier phase is taken into account by a special space–time averaging of the parameters of the test particles over sections of the trajectories within the calculation cells:

$$\langle\varphi\rangle_i=\frac{\sum\limits_{l\in(i)}\dot\eta\int_0^{\tau_i}\varphi_l dt}{\sum\limits_{l\in(i)}\dot\eta\tau_l},\quad n_p=\frac{\Sigma_{l\in(i)}\dot\eta\tau_l}{\Delta x_i\Delta t}.$$

4. The relevant set of homogeneous and heterogeneous chemical reactions induced by a shock wave appears as follows: homogeneous reaction

$$CO_2+M\rightleftarrows CO+O+M$$

$$O_2+M\rightleftarrows 2O+M$$

$$CO_2+O\rightleftarrows CO+O_2$$

where

$$M:\ O,\ O_2,\ CO,\ CO_2; \tag{1}$$

heterogeneous reaction

$$C+O_2\leftrightarrows CO_2$$

$$C+CO_2\rightleftarrows 2CO. \tag{2}$$

5. The description of interphase transport are based on phenomenological models using well-known approximations for the drag coefficient and the Nusselt number.[2] The rates of the chemical reactions determining the composition of the carrier phase and interphase mass exchange were applied by the corresponding investigations in Ref. 3 for homogeneous processes and in Ref. 4 for heterogeneous processes.

6. The algorithm for the calculation within one iteration is the following:

i. calculation of the flow of the carrier phase, without taking into account the disperse phase; ii) calculation of the trajectories of the test particles, iii) calculation of the source terms by space-time averaging; iv) calculation of the flow of the carrier phase with allowance for the source terms. In the later iterations the sequence of steps starts from the second one.

7. In the Euler step of the algorithm the numerical solution is constructed using separation by physical process.[5] The complete step in time looks as follows

$$U_i^{n+2}=L(2\Delta t)U_i^n=L_x(\Delta t)L_c(\Delta t)L_c(\Delta t)L_x(\Delta t)U_i^n,$$

where the operator L_x describes the solution of the equation

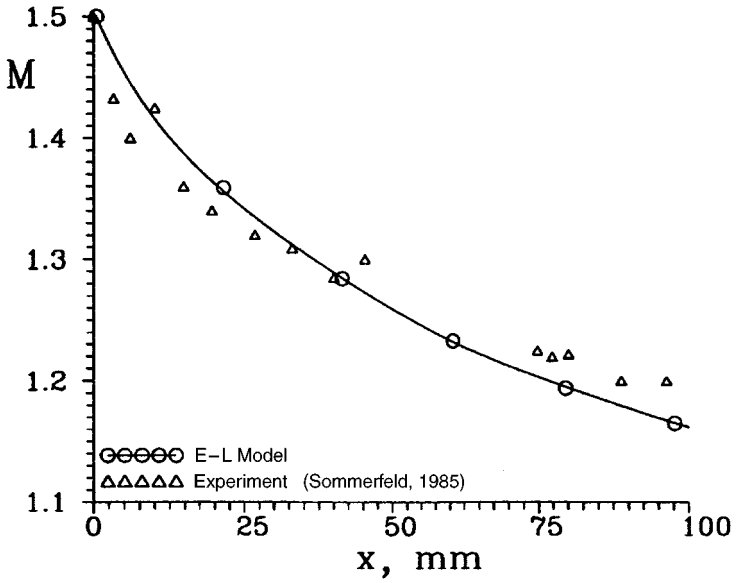

FIG. 1. Intensity of a shock wave moving in a powder-laden gas.

$$\frac{\partial U}{\partial t}+\frac{\partial F}{\partial x}=0$$

and is constructed with the aid of the TVD scheme,[6] while the operator L_c describes the solution of the equation

$$\frac{dU}{dt}=W+Q_p\,.$$

To construct the operator L_c and also to calculate the trajectory of the test particles we used the Adams second-order implicit scheme of approximation.

8. The algorithm described above was used to solve the problem of the interaction of a planar shock wave propagating in oxygen with a cloud of carbon particles located to the left of the closed end of the shock tube. The shock wave moves from right to left.

In Fig. 1 we show a comparison between the experimental data and test calculations of the variation of the intensity of the shock wave and the dependence on the path traveled in the dust-laden gas. The experimental conditions are[7] $M=1.5$, $p_0=1$ atm, concentration of particles by weight is $\alpha=0.6$, the Stokes number, which characterizes the rate of interphase exchange, is $Sk=\tau_{gp}/\tau_g$, where τ_{gp} is the characteristic interphase relaxation time, and τ_g is the characteristic gasdynamic time, which was set equal to 0.01. A calculation using the proposed model shows good agreement with experiment.

In Fig. 2 we present on an x–t plot the density of the carrier gas. The simulation was carried out for the following conditions: $M=5.8$, $p_0=0.01$ atm, the length of the particle cloud 0.3 m, the particle diameter $d_p=1$ μm, and for a mass fraction $\alpha=0.25$ and these parameters, the flow is characterized by a Stokes number $Sk=0.15$ and is close to equilibrium. The normalization scales of the variables, x_0 and t_0, are, respectively, 0.5 m and 3.58×10^{-6} s.

The diagram shows *1* — the incident shock wave that initiates the combustion of the carbon particles, *2* — the waves detached from the outer boundary of the cloud, carried away by a supersonic accompanying flow, *3,4* — the trailing

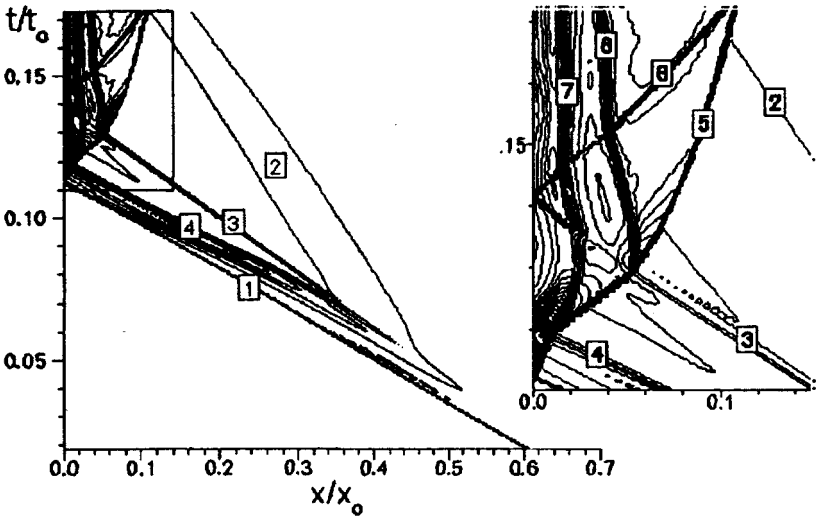

FIG. 2. x–t diagram of the carrier gas ($Sk=0.15$).

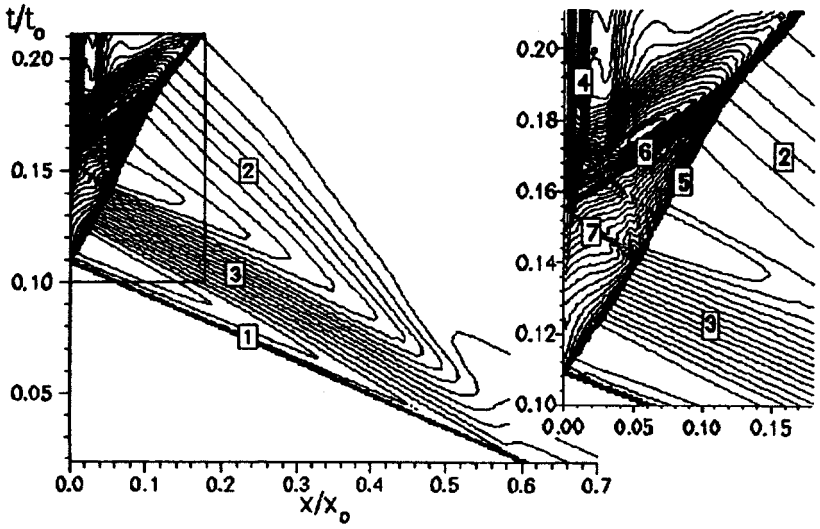

FIG. 3. $x-t$ diatram of the density of the carrier gas ($Sk=3.75$).

and leading edges of the region of hot gas that is formed from the combustion of the particles, *5* — the shock wave *I* reflected from the wall and refracted by nonuniformities in the oncoming accompanying flow, *6* — the wave formed as the result of the interaction of the reflected shock wave *5* with the boundary of the hot gas, and the contact discontinuities *7* and *8* represent the trajectory of the contact discontinuities *4* and *3* after their interaction with the shock waves *5* and *6*. The system of waves included between *1* and *4* and which are formed as the result of the generation of the combustion products, augments the incident wave *1* and increases its velocity.

In Fig. 3 we show on an $x-t$ diagram the density of the carrier gas for particles of diameter $d_p=5$ μm, which corresponds to a Stokes number $Sk=3.75$. This shows *1,5* — the incident shock wave and that reflected from the wall, and *2* — the waves that have reflected from the outer boundaries of the particle cloud. Unlike the preceding case, the flow is characterized by the development of relaxation zones: *3* — the zone of interphase relaxation behind the incident shock wave. The boundary between zones *2* and *3* corresponds to a trajectory of the front of the particle cloud with which the wave *5* interacts and is reflected as a jump *7*. In this case, because of the low rate of the interphase relaxation processes, the combustion of the particles starts only behind the reflected shock wave *5*, and *4* denotes the region of hot gas formed from the combustion of the particles. The generation of the combustion products initiates a system of waves *6* that supplement and accelerate the reflected shock wave.

An analysis of the propagation of the shock wave over a reacting two-phase mixture distinguishes two regimes of initiating combustion: behind the incident shock wave and behind the reflected shock wave. The critical Stokes number, which characterizes the parameters of the mixture and the flow in the transition from one regime to another, can be written as

$$Sk^*=\left(\ln\frac{T_0-T_g}{T^*-T_g}\right)^{-1},$$

where T_0, T_g, and T^* are, respectively, the initial temperature of the disperse phase, the characteristic temperature of the carrier phase, and the temperature at which combustion is initiated. For the mixture and flow parameters given above, $Sk^*\approx 1.6$.

This work received partial support from grants RFFI 95-01-00521 and INTAS 94-4348.

[1] C. T. Crowe, J. Fluids Eng. **104**, 297 (1982).
[2] R. I. Nigmatulin, *Dynamics of Multiphase Media* [in Russian] (Nauka, Moscow, 1987).
[3] Yu. P. Golovachev, *Numerical Simulation of Flows of a Viscous Gas in a Shock Layer* [in Russian] (Nauka, Moscow, 1996).
[4] M. Olim, G. Ben-Dor, M. Mond *et al.*, KSME J. **4**, 167 (1990).
[5] A. I. Zhmakin, Preprint A. F. Ioffe Physicotechnical Institute, Academy of Sciences of the USSR, No. 644 (1980).
[6] S. A. Ilin and E. V. Timofeev, Preprint A. F. Ioffe Physicotechnical Institute, Russian Academy of Sciences, No. 1611 (1993).
[7] M. Sommerfeld, Exp. in Fluids No. 3, 197 (1985).

Translated by J. R. Anderson

Self-excited oscillations in a fiber-optic laser–collimator–microresonator system

V. D. Burkov, F. A. Egorov, and V. T. Potapov

Institute of Radio Engineering and Electronics, Russian Academy of Sciences, Fryazino
(Submitted November 1, 1996)
Pis'ma Zh. Tekh. Fiz. **23**, 33–39 (March 26, 1997)

This paper proposes and studies experimentally a design for a fiber-optic self-excited oscillator, characterized by high stability of the operating point. The design appears promising for developing fiber-optic transducers of physical quantities with a frequency output. © *1997 American Institute of Physics.* [S1063-7850(97)02403-8]

It has been shown[1,2] that in a laser with an additional mirror in the form of an optically excited micromechanical resonator (MR) it is possible to set up self-excited oscillations at the resonant frequency f of the mechanical oscillations of the micromechanical resonator. The properties of the system can be accounted for qualitatively within a model of passive Q-switching of the optical cavity: the oscillations of the micromechanical resonator cause modulations in the effective reflection coefficient R of the Fabry-Perot interferometer formed by the mirror of the optical cavity and the reflecting surface of the micromechanical resonator. Because of the complicated dependence of the spectral characteristics of a three-mirror optical cavity on its geometrical parameters, the reflection coefficient of the interferometer is not only amplitude modulated, but also phase modulated. Because of the dependence of R on the phase change, there exist discrete regions of existence of self-excited oscillations, periodic with the period of the interferometer, equal to $\lambda/2$ (where λ is the lasing wavelength). As the result of external perturbations the operating point of the self-excited oscillation can drift on the interference pattern away from the region of existence, and the self-excited oscillator will therefore be cut off. In this investigation we have proposed and investigated experimentally a design for passive Q-switching of a laser with the use of a micromechanical resonator, in which amplitude modulation of the reflection coefficient plays a major role.

The design is shown in Fig. 1. Its operation is based on Q-switching of a two-mirror optical cavity by the photoinduced angular deflection of one of the mirrors, which is a micromechanical resonator. Active Q-switching of lasers by tilting a mirror has been analyzed in Ref. 3, where the method was shown to be highly effective: a tilt angle of $9'$ results in 100% modulation of the output power of the laser. The experiments were carried out with an erbium fiber-optic laser, whose main parameters are listed in Ref. 1. In the present case, the mirror M_1 was the fiber-air interface ($R_1 \approx 3.2$ %), and the intermode beat frequency of the fiber-optic laser was 12 MHz. Some of the power in the optical beam formed by the collimator C is reflected from the surface of the micromechanical resonator, making an angle θ with the axis of the beam, and is returned back into the fiber-optic cavity of the laser. Because of the photoinduced deformation, the variation of the laser power W_1 incident on the micromechanical resonator causes modulation of the deflection angle $\theta(t)$ of the reflected beam, i. e., modulation, $\eta(\theta(t))$. The collimator consisted of quarter-period graded-index rod lenses, which form Gaussian beams with the parameters 1) beam waist diameter $2w_0 = 780$ μm, divergence angle $2\theta_0 \approx 2.6 \times 10^{-3}$ deg, 2) $2w_0 = 440$ μm, $2\theta_0 \sim 4.0 \times 10^{-3}$ deg. The residual reflection coefficient of the lens did not exceed 0.2%, while the insertion loss was $\simeq 0.4$ dB. The state of the laser was monitored by an asymmetric (1 : 3) single-mode X coupler with ≈ 0.5 dB losses. The micromechanical resonator was made of silicon micromembranes, microbridges, and microcantilevers, prepared by anisotropic etching; their parameters are described in Ref. 1. The experimental curve $\eta(\theta)$ is shown in Fig. 2. The variation in the distance H between the lens and the resonator did not make any significant change in the output optical signals W_2 and W_3, which indicates the absence of large interference effects.

The main experimental results are as follows. Regardless of the topology and construction of the mechanical resonator, when certain conditions are satisfied in this system, self-excited oscillations are set up with a frequency F, which is nearly the same as the resonant frequency, $f \approx F$. These conditions reduce to the following: 1) in the initial state the tilt angle θ_i of the mirror is in the range $\theta_1 \leqslant \theta_i \leqslant \theta_2$, where the ends of the interval (θ_1, θ_2) depend on the characteristics of the mechanical resonator of the laser; 2) the resonant frequency of the resonator is near the frequency f_{rel} of the relaxation oscillations of the laser or its harmonics, $f \approx n \cdot f_{rel}$, where $n = 1,2,3, \ldots$. We note that f_{rel} is determined by the relative pump power $r = P_p / P_{pl}$, where P_{pl} is the threshold pump power of the laser (Ref. 4); 3) the average radiation power W_1 exceeds a certain threshold level W_{1th} that depends on the characteristics of the mechanical resonator and the optical fiber cavity.

Figure 2 shows the experimental results obtained for a mechanical resonator in the form of a microbridge of dimensions $1650 \times 400 \times 6$ μm, with a nickel (Ni) film as the reflecting coating, with a reflection coefficient of 72% (the film thickness h_{Ni} was ≈ 0.3 μm). Because the resonator is quite wide, it coupled efficiently with the optical beam. In the situation described here, the self-excited oscillations were induced with frequencies $F_1 \approx 35.5$ kHz and $F_2 \approx 112.2$ kHz, corresponding to the resonant frequencies of the fundamental and third harmonics of the mechanical resonator, measured with a fiber-optic interferometer.[1] The average power W_1 was 1.5–4.0 mW, and the signal-to-noise ratio in the system

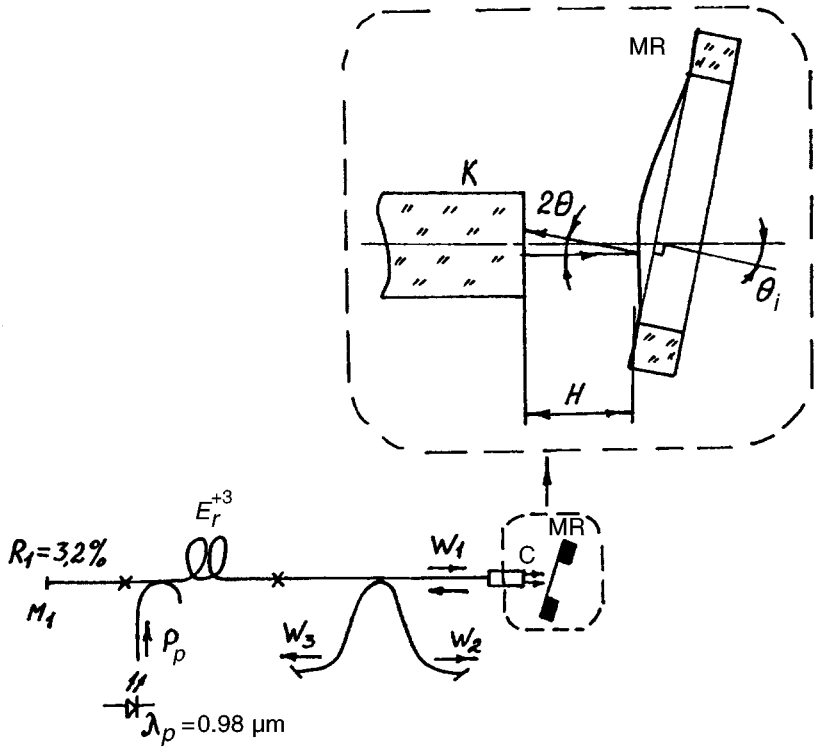

FIG. 1. Diagram of the experimental setup.

was 40–50 dB. The amplitude of the oscillations was $\lesssim 30$ nm. The Q of these modes, measured by means of acoustic excitation, was 90 and 120, respectively. As one can see from Fig. 2, the region of existence of the self-excited oscillations (θ_1, θ_2) for the fundamental is located entirely on one branch of the curve $\eta(\theta)$. This means that the Q-switching of the optical cavity is accomplished principally through modulation of the inclination angle of the beam, and not additionally by its focusing (defocusing) due to bending of the surface of the mechanical resonator during the self-excited oscillations. We note that for the higher oscillation modes, depending on the type of mechanical resonator, these regions can consist of separated intervals. In Fig. 2 the width of the interval $\Delta\theta = \theta_2 - \theta_1$ is $\approx 4\times 10^{-3}$ deg, which gener-

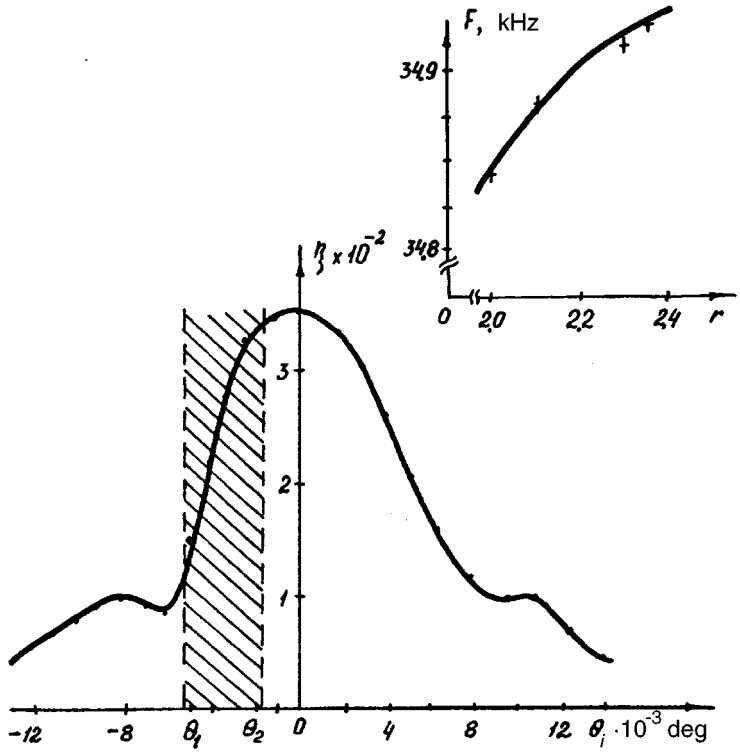

FIG. 2. Experimentally measured $\eta(\theta_p)$ and $F(r)$.

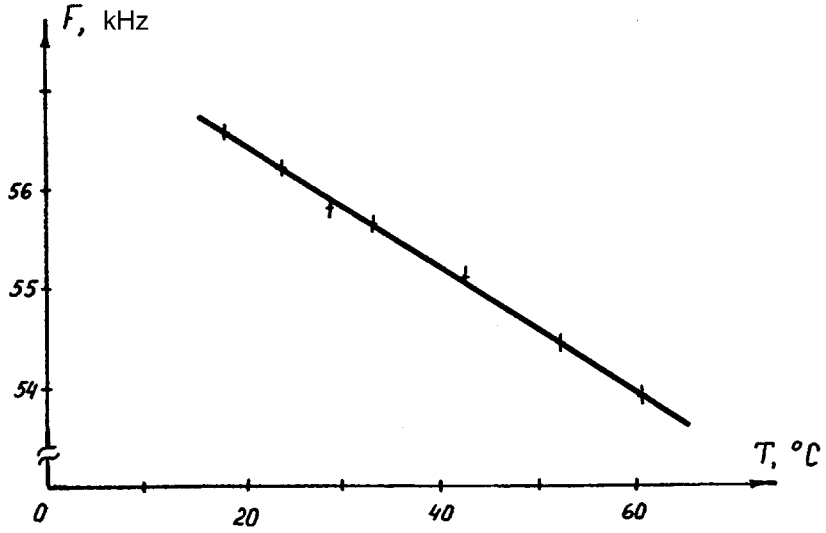

FIG. 3. Experimentally measured $F(T)$.

ally decreases with increasing divergence angle of the beam. It is worth pointing out that when the variation of H is in the submicron range or when it is large, (± 1.5 mm) the self-excited oscillations are not cut off, and the frequency instability is $\Delta F/F \leqslant 3\times 10^{-4}$. In the interval (θ_1, θ_2) we find a weak functional dependence $F(\theta_i)$, which may or may not be monotonic, depending on the angular and linear geometric parameters that characterize the spatial orientation of the optical beam relative to the mechanical resonator. The dependence of the frequency $F(r)$ of the self-excited oscillations on the pump power, determined for fixed spatial parameters of the system, is shown in Fig. 2. We believe that this monotonic dependence can be explained by the pulling of the frequency of the mechanical resonator by the relaxation oscillations of the laser, whose frequency increases with increasing P_p. When the parameters of the system are varied, the kind of excitation of the self-excited oscillations (''soft'' or ''hard'') depends on the specific type of parameter that is varying.

Figure 3 shows the frequency of the self-excited oscillations versus the microbridge temperature T, which is varied by means of a Peltier element in the temperature range 10–70 °C. The micromechanical resonator with the Ni film had dimensions of $1400\times 300\times 6$ μm, and the fundamental resonant frequency at room temperature was $f \approx 56.3$ kHz. When the temperature was varied in the stated interval, the system remained at all times in the range of stable self-excited oscillations. It is shown in Fig. 3 that the function $F(T)$ is nearly linear, with a temperature coefficient $K_T = (1/F)dF/dT \approx -0.08\%$ K^{-1}. The negative sign of K_T is probably related to the fact that the effective thermal expansion coefficient α_{eff} of the micromechanical resonator, which is a layered structure of silicon and nickel, is higher than the thermal expansion coefficient α_{Si} of the silicon base of the microbridge

$$\alpha_{\text{eff}}/\alpha_{\text{Si}} = (1 + E_{\text{Ni}} h_{\text{Ni}} \alpha_{\text{Ni}} / E_{\text{Si}} h_{\text{Si}} \alpha_{\text{Si}}) \times (1 + E_{\text{Ni}} h_{\text{Ni}} / E_{\text{Si}} h_{\text{Si}})^{-1},$$

where E_{Ni}, E_{Si}, h_{Ni}, and h_{Si} are the Young's modulus and thickness, respectively, of the nickel and the silicon mechanical resonator, respectively.

Since $\alpha_{\text{Ni}} = 13.0\times 10^{-6}$ K^{-1} and $\alpha_{\text{Si}} = 2.3\times 10^{-6}$ K^{-1}, it is obvious that $\alpha_{\text{eff}} > \alpha_{\text{Si}}$. As a consequence, a temperature rise of the microbridge induces longitudinal stresses that reduce the resonant frequency.[5] The dependence of the composite mechanical resonator on the physical parameters of the films thus allows us to study their properties.

In this investigation it has been shown that 1) amplitude modulation of the reflectance of the optical cavity of the laser is sufficient to generate self-excited oscillations in a system composed of a laser and a micromechanical resonator; 2) the proposed method for obtaining optical feedback between the laser and the mechanical resonator makes the operating point of the self-excited oscillator very stable; 3) a fiber-optic system will allow one to measure the parameters of the surrounding medium (for example, the temperature) and study the physical properties of the thin-film structures.

[1] V. D. Burkov, F. A. Egorov, and V. T. Potapov, Pis'ma Zh. Tekh. Fiz. **22**(18), 16 (1996) [Tech. Phys. Lett. **22**, 738 (1996)].
[2] V. D. Burkov, F. A. Egorov, and V. T Potapov, Pis'ma Zh. Tekh. Fiz. **22**(19), 18 (1996) [Tech. Phys. Lett. **22**, 785 (1996)].
[3] G. N. Belova and E. I. Remizova, Kvantovaya Elektron. (Moscow) **11**, 192 (1984) [Sov. J. Quantum Electron. **14**, 131 (1984)].
[4] V. N. Tsikunov, Zh. Eksp. Teor. Fiz. **58**, 1646 (1970) [Sov. Phys. JETP **31**, 882 (1970)].
[5] D. Walsh and B. Culshaw, Sensors and Actuators A **25–27**, 711.

Translated by J. R. Anderson

Model of a two-dimensionally focusing ultrasonic x-ray lens based on Bragg–Fresnel optics

A. M. Egiazaryan

Institute of Applied Problems in Physics, Armenian National Academy of Sciences, Erevan
(Submitted November 12, 1996)
Pis'ma Zh. Tekh. Fiz. **23**, 40–43 (March 26, 1997)

A model is proposed for a two-dimensionally focusing x-ray lens, whose operation is based on the principle of Bragg–Fresnel optics. It is shown that the lens has a large aperture.
 [S1063-7850(97)02503-2]

The rapid development of microelectronics has been due to the conception and development of new x-ray elements. In Refs. 1 and 2 a one-dimensionally focusing x-ray lens was devised, whose operating principle is based on the idea of Bragg–Fresnel optics — a newly developing field of x-ray optics. A one-dimensional microstructure is produced on the entrance surface of a perfect single crystal in such a way that only even Fresnel zones participate in the Bragg reflection of the incident x-ray beam and focus the beam in a single direction.

In the present paper a model is proposed for a two-dimensionally focusing x-ray lens, whose operation is like that described above. The two-dimensional microstructure at the entrance surface of the single crystal is created by the interference of ultrasonic waves.

We assume that the beam of monochromatic x rays comes from a point source located at the point $(x_0, 0, z_0)$ and is incident on the entrance surface $(x, 0, y)$ of a perfect single crystal with parallel faces (see Fig. 1). The reflecting planes are parallel to the entrance surface. Simultaneously, point sources of coherent ultrasonic waves are produced in pairs at the points $(-x_1, 0, -t_0)$, $(x_1, 0, -t_0)$, $(0, -y_1, -t_0)$ and $(0, y_1, -t_0)$ of the exit surface of the single crystal. These waves interfere inside the crystal where they superimpose, and because of this interference a corresponding microstructure is produced on the entrance surface of the single crystal. When this microstructure matches the geometry of the one-dimensional Fresnel zones in the X and Y directions the reflected x-ray beam is focused in these directions at the point $(x_f, 0, z_f)$.

The surfaces of constant intensity in the interference field of ultrasonic waves, generated at the points $(-x_j, 0, -t_0)$ and $(x_j, 0, -t_0)$, are hyperboloids that satisfy the equation

$$d_1 - d_2 = \text{const}, \tag{1}$$

where

$$d_1 = \sqrt{(x+x_1)^2 + t_0^2}\,,$$

$$d_2 = \sqrt{(x-x_1)^2 + t_0^2}\,. \tag{2}$$

When the condition

$$k\frac{x^4}{d^3} \ll 1 \tag{3}$$

is satisfied, where k is the wave number of the ultrasound, Eq. (1) takes on the form

$$\frac{2xx_1}{d} = \text{const}. \tag{4}$$

It is easy to see that the corresponding regions of the surfaces of maximum and minimum intensity, where the points $(-x_1, 0, -t_0)$, $(x_1, 0, -t_0)$, $(0, -y_1, -t_0)$, and $(0, y_1, -t_0)$ are excited, are evenly distributed, mutually perpendicular planes parallel to the ZY and ZX planes. The function $\overline{u}$ of the inclination of the crystal at the entrance surface of the single crystal varies according to the arrangement of these planes, which are responsible for the corresponding microstructure on this surface.

From the condition for the reflection of the x rays

$$\frac{x_0}{d_0} = -\frac{x_f}{f_0} \tag{5}$$

and the condition for the formation of the mth Fresnel zone

$$d_0 + f_0 + m\lambda < d_{01} + f_{01} < d_0 + f_0 + m\lambda + \frac{\lambda}{2} \tag{6}$$

we obtain for the coordinates x_m of the boundaries of this zone in an approximation that includes up through second-order terms

$$m\alpha\lambda < x_m^2 < m\alpha\lambda + \frac{\alpha\lambda}{2}, \tag{7}$$

where λ is the wavelength of the x rays and

$$\frac{1}{\alpha} = \frac{1}{d_{01}} + \frac{1}{f_{01}} - \frac{2x_0^2}{d_{01}^3} - \frac{2x_f^2}{f_{01}^3}. \tag{8}$$

A numerical evaluation of condition (7) shows that the dimensions of neighboring zones beginning with the third zone coincide to the second decimal place. Consequently it can be stated that the corresponding regions of the boundaries of the Fresnel zones are mutually perpendicular and equally spaced straight lines parallel to the ZY and ZX planes. The frequency of the ultrasonic waves can be chosen so that the planes of maximum intensity of the interfering fields, given by condition (4), pass through the middle of the even Fresnel zones, which, because of the interaction with the ultrasound, are incident in the angular range for Bragg reflection. In this case the odd Fresnel zones lie outside this range, and only the even Fresnel zones, which reinforce one

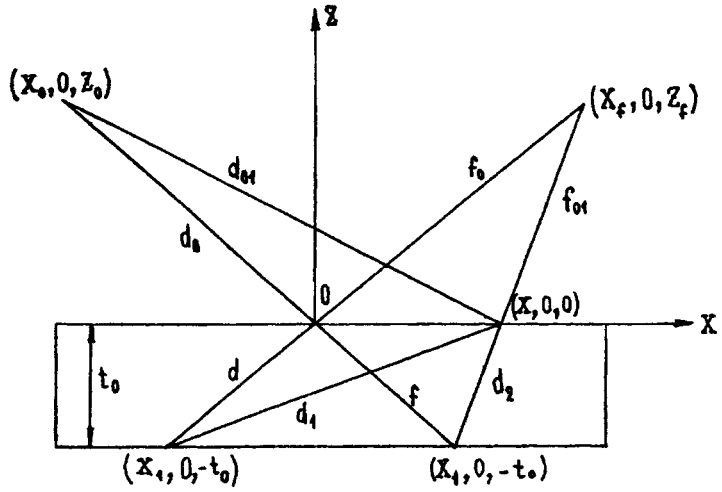

FIG. 1. $X-Z$ cross section of the proposed lens.

another, take part in the reflection of the x rays. As a result, the x rays are focused at the focal point $(x_f, 0, z_f)$ in the Y and X directions. Calculations show that the relative x-ray intensity at this point (relative to the intensity of the radiation reflected from the single crystal without the ultrasound) is proportional to the parameter N, where N is the number of participating Fresnel zones. In this way the proposed model of a two-dimensionally focusing ultrasonic x-ray lens, whose operation is based on the principle of Bragg–Fresnel optics, also has a large relative aperture.

I would like to extend my thanks to Academician A. R. Mkrtchyan for valuable discussions.

[1] V. V. Aristov *et al.*, JETP Lett. **44**, 265 (1986).
[2] V. V. Aristov, Yu. A. Basov, and A. A. Snigerev, Pis'ma Zh. Tekh. Fiz. **13**, 114 (1987) [Sov. Tech. Phys. Lett. **13**, 49 (1987)].

Translated by J. R. Anderson

Ultraviolet HeCd laser pumped by a high-frequency electron beam

Yu. N. Novoselov and V. V. Uvarin

Institute of Electrophysics, Russian Academy of Sciences, Ekaterinburg
(Submitted November 20, 1996)
Pis'ma Zh. Tekh. Fiz. **23**, 44–47 (March 26, 1997)

An electron beam with a large cross section and with a repetition rate of 3×10^5 pulses per second in a packet has been obtained for the first time. With this beam a HeCd high-pressure laser has been developed and high-frequency lasing on the Cd ion at a wavelength of 325 nm has also been achieved for the first time. © *1997 American Institute of Physics.* [S1063-7850(97)02603-7]

A high-pressure helium-cadmium mixture has a low lasing threshold,[1] which applies also to the threshold for lasing at the ultraviolet line at 325 nm.[2] Pulsed generation at 325 nm on the $5s^2\,{}^2D_{3/2}$–$5p^2P_{1/2}$ transition of the cadmium ion was obtained with electron beam pumping at nanosecond[3] and microsecond[2,4] pulse lengths. However, with pumping by a quasi-steady-state beam with a pulse length of tens of microseconds, lasing was obtained only in a mixture containing the electronegative component CCl_4 (Ref. 4). In Ref. 5 model calculations were carried out that showed that the pulse repetition rate in a HeCd laser with excitation of the mixture by a picosecond electron beam can reach 10^6 pulses per second. The purpose of the work reported in the present article was to obtain high-frequency lasing at 325 nm.

To carry out the experiments we used an apparatus similar to that described in Refs. 2 and 4. The mixture was pumped by an electron beam with a cross section of 2×70 cm and an electron energy of 180 keV. The laser cell was 3 cm in diameter, it had pieces of cadmium affixed to the wall, was filled with helium to a pressure of 1–2 atmospheres, and could be heated to 450 °C. The apparatus provided for continuous cleaning of the helium, by flowing the gas at a rate of $\sim$0.1 cm/s through a liquid-nitrogen-cooled zeolite filter and the laser cell. The laser cavity was formed from a spherical mirror with a 5 m radius of curvature and a plane exit mirror, with a reflection coefficient of 99.5% for the two mirrors. The power and time characteristics of the laser radiation were measured by a calibrated FÉU-22SPU photomultiplier, with the signal displayed on an S9-27 oscilloscope.

The electron source was an accelerator with a plasma cathode and grid control of the emission current, as described in Ref. 6, which could generate a packet of electron pulses with a pulse length of 200 ns at half-height, a repetition rate of 100 kHz, and a packet length of 200 μs. This accelerator was modernized to increase the pulse repetition rate in the packet to 300 kHz. For this purpose the control-grid pulse generator was equipped with a switching element including the previously used tasitron and in addition, a bank of 10 GMI-6 oscillator tubes connected in parallel. To reach the generation threshold in each pulse, the pulse length was increased to 1 μs. An oscilloscope trace of the electron beam pulse packet is shown in Fig. 1a. It can be seen that the pulse amplitude comes to a steady value in a period of time equal to the rise time of the plasma-forming discharge current in the emitter. Figure 1a shows the first 60 μs; thereafter there are no changes in the behavior of the current pulses out to 140 μs. The maximum steady-state current pulse amplitude was 30 A.

Ultraviolet lasing at 325 nm, as in Ref. 4, was obtained only when carbon tetrachloride was added to the mixture. In the experiments we determined the main parameters of the operating mixture for which the radiation pulse energy was the highest. An oscilloscope trace of the packet of laser pulses is shown in Fig. 1b. The maximum specific lasing power in a single pulse was 4 mW/cm^3. For this output the helium concentration was 1.2×10^{19} cm^{-3}, and the temperature of the medium was 390 °C, i.e., the concentration of cadmium vapor was $\sim3\times10^{16}$ cm^{-3}, and the concentration of CCl_4 was 3×10^{15} cm^{-3}.

It can be seen from the oscilloscope readouts (Fig. 1) that the first few pulses fail to produce lasing in the mixture. We believe the reason has to do with the pumping of the $5s^2\,{}^2D_{3/2}$ upper laser level of the cadmium ion. It is well-known that the Penning reaction between the metastable states of the helium and cadmium atoms contribute to the

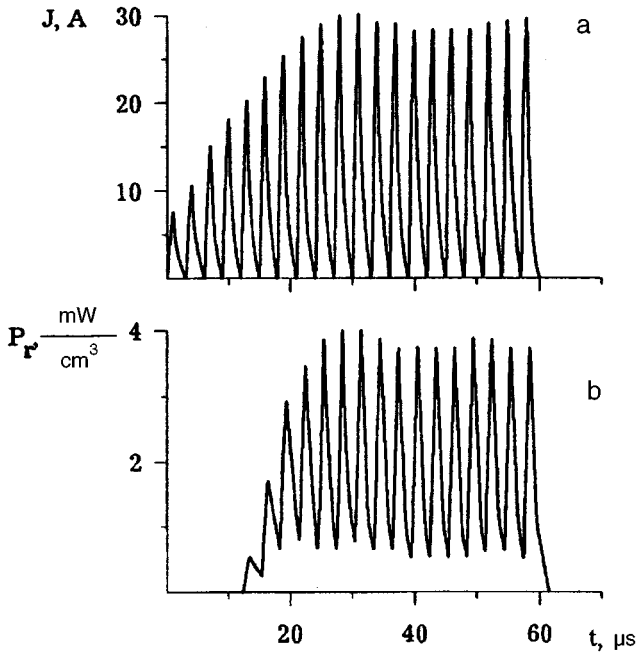

FIG. 1. Oscilloscope traces of the electron beam pulses (a) and the laser pulses (b).

 1063-7850/97/030229-02$10.00

population of this level.[1,5] It is probable that under our experimental conditions the pump power of the first 3–4 pulses of the electron beam is insufficient to create a concentration of metastable helium atoms for which the lasing threshold can be reached. Lasing starts when the accumulation of metastable heliums in the active medium is sufficient.

A characteristic feature of this oscilloscope trace of the radiation is the background emission in between the individual pulses. This can also be explained by the rather high concentration of metastable helium that cannot decrease very much in the intervals between the pump pulses. It is suggestive that the amplitude of the first lasing pulse is about equal to the background level.

In this figure one can see that the amplitude peak of the individual lasing pulses (b) is offset in time relative to the peak of the electron beam (a). This delay is about 0.5 μs, and is due to the recombination nature of the population of the upper laser level.[1,5]

To summarize, in this investigation we have obtained for the first time pumping of a high-pressure helium-cadmium laser by an electron beam with a repetition rate 3×10^5 pulses per second, and also have obtained for the first time high-frequency ultraviolet lasing in this laser.

[1] A. V. Karelin and S. I. Yakovlenko, Kvantovaya Elektron. (Moscow) **20**, 631 (1993) [Quantum Electron. **23**, (1993)].
[2] V. A. Makeev, Yu. N. Novoselov, M. Yu. Starovoĭtov, and V. V. Uvarin, Pis'ma Zh. Tekh. Fiz. **19**(9), 10 (1993) [Tech. Phys. Lett. **19**, 263 (1993)].
[3] F. G. Goryunov, V. I. Derzhiev, N. G. Zhidkov *et al.*, Kvantovaya Elektron. (Moscow) **16**, 2039 (1989) [Sov. J. Quantum Electron. **19**, 1312 (1989)].
[4] Yu. N. Novoselov and V. V. Uvarin, Pis'ma Zh. Tekh. Fiz. **21**(23), 15 (1995) [Tech. Phys. Lett. **21**, 955 (1995)].
[5] S. V. Makarov, Yu. N. Novoselov, and V. V. Osipov, Kvantovaya Elektron. (Moscow) **17**, 974 (1990). [Sov. J. Quantum Electron. **20**, 891 (1990)].
[6] V. I. Gushenets, N. N. Koval', D. L. Kuznetsov, G. A. Mesyats, Yu. N. Novoselov, V. V. Ufarin, and P. M. Shchanin, Pis'ma Zh. Tekh. Fiz. **21**(23), 26 (1991) [Sov. Tech. Phys. Lett. **21**, 834 (1991)].

Translated by J. R. Anderson

Photorefractive surface waves in sillenite crystals in an alternating-sign electric field

S. M. Shandarov and N. I. Nazhestkina

Tomsk State Academy of Control and Radioelectronics Systems
(Submitted September 2, 1996)
Pis'ma Zh. Tekh. Fiz. **23**, 48–53 (March 26, 1997)

A theoretical model is proposed for photorefractive TE surface waves in a sillenite crystal located in an alternating-sign electric field
[S1063-7850(97)02703-1]

The nonlinear self-channeling of light in photorefractive crystals is observed at low beam intensities,[1–7] and therefore is of considerable interest for developing optical switches, shutters, and other optoelectronic elements. The self-channeling effect can be observed in the formation of three-dimensional solitons, acting as a channel for the propagation of a light beam, in which the diffraction-related divergence is compensated by self-induced variations in the refractive index.[1–3] Nonlinear surface waves in photorefractive crystals with a strong diffusion response have been predicted in Ref. 4. The first experimental observation of such photorefractive surface waves in $BaTiO_3$ crystal was reported in Ref. 5.

In sillenite crystals ($Bi_{12}SiO_{20}$, $Bi_{12}GeO_{20}$, and $Bi_{12}TiO_{20}$) the small electrooptical constant ($\sim 5\times 10^{-12}$ m/V) entails a weak diffusion response. However, photorefractive variations in the refractive index can be greatly increased by applying to the crystal an external alternating-sign electric field.[8] The redistribution of the light beam intensity at the exit face of a fiber sample of $Bi_{12}SiO_{20}$ attached to one of the electrodes used to apply the alternating-sign field has been studied in Refs. 6 and 7. This effect results in a substantial reduction in the time of the photorefractive response and is interpreted as the self-channeling of light in the form of surface photorefractive waves. The present communication presents as theoretical analysis of the photorefractive variations in the refractive index by the action of a light beam on a crystal of a group of sillenites placed in an alternating-sign electric field and an analysis of the photorefractive surface waves in these crystals.

Let us consider a sillenite sample *1* in which a light beam travels with uniform intensity $I(x)$ along the [110] crystallographic axis (the Z axis in Fig. 1). The external alternating-sign field in the form of a square wave with an amplitude E_0 and a period T is applied to the electrodes *2* along the X axis. The photoexcitation of charge carriers and their redistribution over the impurity centers by way of diffusion and drift in an electric field create a space-charge field $E_{sc}(x)$. This field through the electrooptical effect changes the refractive index of the crystal by an amount $\Delta n(x)\sim E_{sc}(x)$, and under certain conditions induces self-screening of the initial light beam. For crystals with a single partially compensated optically active donor level and one type of carrier the space-charge field $E_{sc}(x)$ can be found from an analysis of the known constitutive equations for a model of zone transport.[9] We linearized these equations with the conditions $\partial n/\partial t=0$, $n\ll N_A$, $\gamma_R N_A \gg SI$, $N_D \gg N_A$, and $\partial E_{sc}/\partial x \ll eN_A/\varepsilon$, where n is the electron concentration in the conduction band, N_A and N_D are the concentrations of compensating acceptors and donors, e is the electron charge, ε is the dc permittivity of the crystal, γ_R is the two-particle recombination coefficient and the S-cross section for photoionization of the donor center. The first four approximations are frequently used for analyzing photorefractive effects (see, e. g., Ref. 10), and the last term corresponds to a field (x) small in comparison with the trap saturation field. The linear equation for $E(x)$ can be written as

$$\frac{\partial}{\partial t}\left\{E_{sc}-L_E\frac{\partial E_{sc}}{\partial x}-L_D^2\frac{\partial^2 E_{sc}}{\partial x^2}\right\}+\delta(\beta+SI)\times\left\{E_{sc}-\frac{L_S^2}{L_D^2}L_E\frac{\partial E_{sc}}{\partial x}-\frac{L_S^2}{(\beta+SI)}\frac{\partial}{\partial x}\left[(\beta+SI)\frac{\partial E_{sc}}{\partial x}\right]\right\}=-\delta SI\left[E_0+\frac{k_BT}{e}\frac{1}{I}\frac{dI}{dx}\right], \quad (1)$$

where $L_E=\mu\tau_R E_0$ is the drift length, $L_S=[k_BT\varepsilon/(e^2N_A)]^{1/2}$ is the Debye screening length, $L_D=(\mu\tau_R k_BT/e)^{1/2}$ is the diffusion length, $\delta=e\mu\tau_R N_D/\varepsilon$, β is the thermal ionization rate, $\tau_R=(\gamma_R N_A)^{-1}$ is the recombination time, μ is the electron mobility, k_B is Boltzmann's constant, and T is the absolute temperature.

For the $Bi_{12}TiO_{20}$ crystal with the typical parameters $\mu/\gamma_R=1.7\times 10^{12}$ m$^{-1}\cdot$V^{-1} and $N_A=10^{23}$ m^{-3} (Ref. 6), and an electric field amplitude $E_0=10$ kV/cm we have $L_S=0.025$ μm, $L_D=0.66$ μm, and $L_E=17$ μm. In this case, when the size of the nonuniformities of the light distribution are $a>5$ μm, we can neglect terms containing second derivatives with respect to the spatial coordinate in Eq. (1). Using thereafter the well-known procedure for averaging the field $E_{sc}(x)$ over the period T of the applied voltage[8] and neglecting trap saturation, we obtain an expression for the average space-charge field $\widetilde{E}_{sc}(x)$ in the form

$$\widetilde{E}_{sc}(x)=\left(\mu\tau_R E_0^2+\frac{k_BT}{e}\right)\frac{1}{(\beta+SI)}\frac{d}{dx}(SI). \quad (2)$$

If the thermal conductivity is negligible, $\beta \ll SI$, then expression (2) for $E_{sc}(x)$ corresponds to the logarithmic model of photorefractive nonlinearity,[4,5] but with a response that can be much faster than the diffusion response in crystals with $L_E \gg L_D$. In this case the transverse field distribution in the photorefractive surface TE wave, $E_y(x,y)=A(x)\exp(i\beta z)$ satisfies the linear equation[4,5]

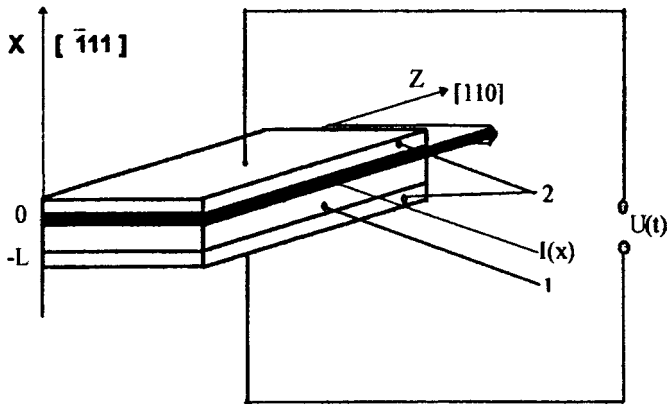

FIG. 1. Configuration of the sillenite crystal with an applied square- wave voltage $U(t)$ and a light beam that excites the photorefractive surface wave: *1* — crystal, *2* — metal electrodes.

$$\frac{d^2A}{dx^2}+(k_2^2-\beta^2)A+2q\frac{dA}{dx}=0 \text{ for } 0\geqslant x\geqslant -L, \tag{3}$$

where $k_2=2\pi n_2/\lambda$, λ is the wavelength of the light wave, n_2 is the refractive index of the unperturbed crystal, and the parameter q takes into account the change in the refractive index due to the photorefractive effect. In our model it takes the form

$$q=\left(\frac{2\pi}{\lambda}n_2^2\right)^2 r_{\text{eff}}\left(\mu\tau_R E_0^2+\frac{k_BT}{e}\right), \tag{4}$$

where r_{eff} is the effective electrooptical coefficient of the crystal.

For a sample with metal electrodes (Fig. 1), if we use the boundary conditions $E_y(0,z)=E_y(-L,z)=0$, the transverse field distribution in the photorefractive surface wave can be brought to the form

$$A(x)=\exp(qx)\sin(\sqrt{k_2^2-q^2-\beta}x) \tag{5}$$

with a propagation constant

$$\beta=\sqrt{k_2^2-q^2-\frac{(m+1)^2\pi^2}{L^2}}, \tag{6}$$

where $m=0,1,2,\ldots$ is the index of the eigenmode. Strictly speaking, the optical activity and the linear birefringence induced by the external field results in elliptical polarization of the light wave in the sillenite crystals, which is not accounted for in Eq. (3). However, when an external field $E_0\sim 10$ kV/cm is applied in the [111] direction in the $Bi_{12}TiO_{20}$ crystal, the polarization eigenvectors have very little ellipticity, with the ellipse axes parallel and perpendicular to this direction.[11] Therefore we can assume that if the input light beam is polarized $e_{\perp}^{\parallel}$ [111] (Fig. 1), photorefractive TE surface waves will be excited in the crystal.

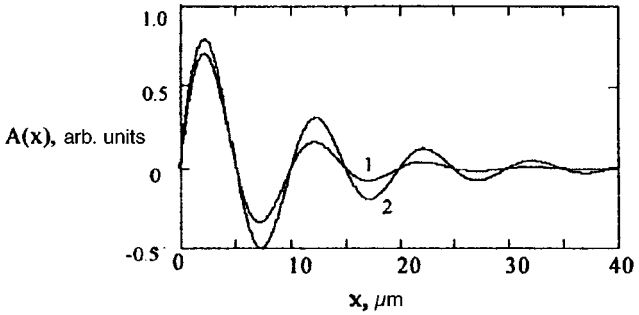

FIG. 2. Typical profiles of the transverse distribution of the optical field in a photorefractive surface wave for the $m=150$ TE mode for an external field amplitude $E_0=10$ kV/cm (*1*) and $E_0=8$ kV/cm (*2*).

The transverse distributions of the optical field ($\lambda = 633$ nm) for the mode with $m=150$ in a $Bi_{12}TiO_{20}$ crystal with a thickness $L=1$ mm for $E_0=10$ kV/cm and $E_0=8$ kV/cm are shown in Fig. 2. In the calculations we used the crystal parameters cited above and $r_{\text{eff}}=2\times10^{-12}$ m/V, which is determined with allowance for the photoelastic contribution from the data of Refs. 12. As one can see from Fig. 2, as the amplitude of the external field increases, the photorefractive surface of the TE wave close to the crystal boundary $z=0$ becomes more localized. At an amplitude $E_0=10$ kV/cm most of the energy in the wave is transported in a layer of thickness ~ 15 μm. Hence we have in this paper shown a simple theoretical model for the photorefractive surfaces of the TE waves for a sillenite crystal placed in an alternating-sign electric field.

This work was carried out with the partial support of the ''Stek'' company.

[1] G. C. Duree, J. L. Shultz, G. I Salamo *et al.*, Phys. Rev. Letters **71**, 533 (1993).
[2] M. Taya, M. Bashaw, M. M. Fejer *et al.*, Phys. Rev. A. **52**, 3095 (1995).
[3] M. Morin, G. Duree, G. Salamo, and M. Segev, Opt. Lett. **20**, 2066 (1995).
[4] G. S. Garcia Quirino, J. J. Sanchez Mondragon, and S. Stepanov, Phys. Rev. A. **51**, 1571 (1995).
[5] M. Cronin-Colomb, Opt. Lett. **20**. 2075 (1995).
[6] A. A. Kamshilin, E. Raita, V. V. Prokifiev, and T. Jaaskelainen, Appl. Phys. Lett. **67**, 3242 (1995).
[7] E. Ratia, A. A. Kamshilin, and A. V. Khomenko, *Second International Conference on Optical Information Processing: Adv. Tech. Progr. and Abstr.*, 1996. p. 21–22.
[8] S. I. Stepanov, and Petrov, Opt. Commun. **53**, 292 (1985).
[9] N. V. Kukhtaren, M. V. Markov, and S. G. Odulov, Ferroelectrics **22**, 949.
[10] P. Gunter and J.-P. Huignard, eds., *Photorefractive Materials and Their Applications I and II*. V. 61 and 62 of *Topics in Applied Physics* (Springer-Verlag, Berlin, 1988 and 1989).
[11] R. V. Litvinov, *Investigation of the Interaction of Optical Waves with the Photorefractive Nonlinearity of Noncentrosymmetric Crystals, Based on a Modal Approach*, Candidate's dissertation, Fiz. Material. Nauk, Tomsk, 1996.
[12] S. M. Shandarov, V. V. Shapelevich, and N. D. Khat'kov, Opt. Spektrosk. **70**, 1068 (1991) [Opt. Spectrosc. (USSR) **70**, 627 (1991)].

Translated by J. R. Anderson

New potential applications of scanning electron microscopy to studying InAsSb/InAsSbP lasers

V. A. Solov'ev, M. P. Mikhaĭlova, M. V. Stepanov, V. V. Sherstnev, and Yu. P. Yakovlev

A. F. Ioffe Physicotechnical Institute, Russian Academy of Sciences, St. Petersburg
(Submitted December 17, 1996)
Pis'ma Zh. Tekh. Fiz. **23**, 54–60 (March 26, 1997)

New potentials are demonstrated for the application of scanning electron microscope methods to identifying heteroboundaries, monitoring the sharpness of interfaces, and determining the positions of $p-n$ junctions in laser structures based on InAsSb/InAsSbP, including at low temperatures. The method permits optimization of the parameters of long-wavelength lasers and to obtain record low threshold currents ($I_{th} \leqslant 25$ mA at $T = 77$ K) for lasing wavelengths $\lambda = 3-3.5$ μm. © *1997 American Institute of Physics.* [S1063-7850(97)02803-6]

A great deal of interest has recently been focused on the laser diodes for the mid infrared region of 3–5 μm, based on narrow-gap semiconducting III–V compounds.[1–5] Such lasers operating at room temperature are very important for laser diode spectroscopy and ecological monitoring, since the absorption bands of many industrial and natural gases lie in this wavelength range.[6] However, the highest operating temperature for lasers based on the solid solutions InAsSb/InAsSbP has been 180–200 K (Refs. 1 and 4).

The problem of obtaining better laser structures having a correspondingly higher operating temperature is directly related to the development of methods of monitoring the parameters of the internal geometry of the structure, such as the layer thickness, the sharpness of the heteroboundary, the position of the $p-n$ junction relative to the heteroboundary, etc. The last parameter is particularly important, since it determines to a large degree the threshold current of injection heterolasers. Methods that have gained wide use for diagnostics of heterostructures involve scanning electron microscope techniques, which have a high spatial resolution and are able to record a number of different signals, including secondary electron emission, reflected electrons, the current induced by the electron probe, etc.[7] To determine the position of the $p-n$ junction relative to the known positions of the heteroboundaries one can use simultaneous measurements of the current induced by the electron probe and the reflected electrons, or the current induced by the electron probe and secondary electrons. However, an attempt to use the standard approaches of secondary electron microscopy to study lasers based on solid solutions of InAsSb and InAsSbP encountered a number of problems, whose solution is the subject matter of this paper.

Such heterostructures, as a rule, will have a large leakage current at 300 K, so that in most cases it is not possible to record the signal current induced by the electron probe at room temperature. Difficulties also arise in measuring the reflected electron signal because of the low signal-to-noise ratio. In addition, the reflected electron signal profile has an unusual shape, which is difficult to explain from a comparison with previously published information.

We investigated double heterostructures with $InAsSb_{0.15}P_{0.3}$ wide-gap emitters and an $InAsSb_{0.05}$ active region, as well as structures with a broadened $InAsSb_{0.05}P_{0.1}$ waveguide, grown by liquid-phase epitaxy on an InAs(100) substrate. The line profiles of secondary electrons, reflected electrons, and the current induced by the electron probe were measured by scanning the electron beam over a cleavage surface of the sample in the direction perpendicular to the epitaxial layers. The accelerating voltage in our experiment was set at $U = 10-15$ kV, and probe current was $I_b = (1-5) \times 10^{-10}$ A.

To solve the problem of the identification and accurate determination of the position of the heteroboundary, we studied the formation of the secondary electron signal and the reflected electron signal because these signals are also used for measuring the thickness of the layers with different chemical composition.

It was found that the contrast in the secondary emission measurements was not stable. With a single scan of a previously unirradiated portion of the sample, we observed sharp contrast, opposite in sign to the contrast observed in the reflected electron measurements (Fig. 1). With multiple scanning this contrast decreased, reversed its sign, and became

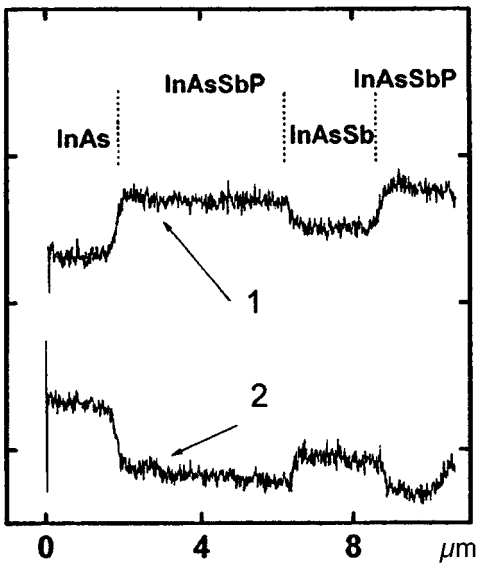

FIG. 1. Line profiles of the reflected electron signals (*1*) and of the secondary electron signals (*2*) for a double heterostructure.

 1063-7850/97/030233-03$10.00

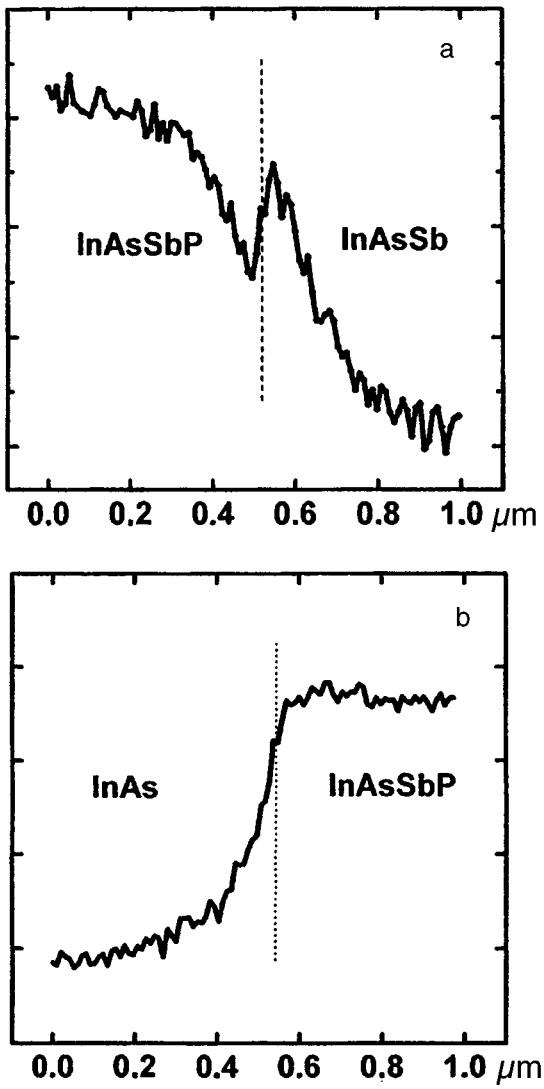

FIG. 2. Line profiles of the reflected electron signals near the InAsSbP–InAsSb heterojunction (a) and the InAs–InAsSbP heterojunction (b).

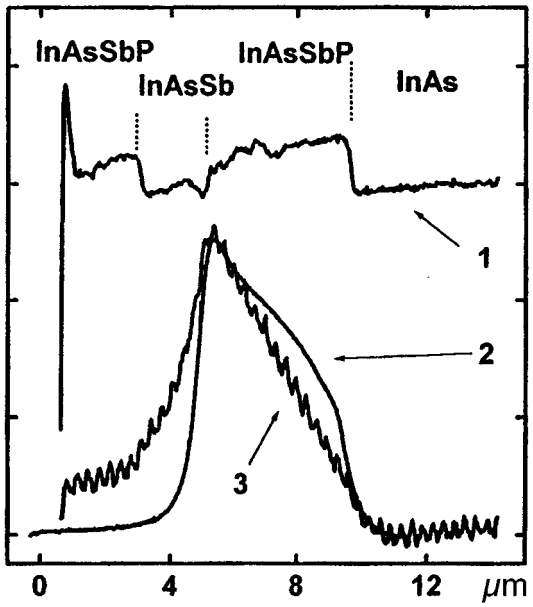

FIG. 3. Line profiles of the reflected electron signals (*1*) and the current induced by the electron probe, at $T=81$ K (*2*) and 300 K (*3*) for a double heterostructure.

similar to that in the secondary electron measurements. Therefore it is better to use the reflected electron methods.

A feature of the structures based on the multicomponent solid solutions is that the average atomic numbers Z for neighboring epitaxial layers are nearly the same. Therefore the contrast of the reflected electrons is small even compared to the system AlGaAs–GaAs (Ref. 8), and is $<2\%$ in relative units. To eliminate artifacts and determine accurately the location of the heteroboundary, the reflected electron profiles were studied on freshly cleaved structures before applying the contacts, with the cleaves made close to the crystallographic planes with a minimum of defects.

In Ref. 9 the structure AlGaAs–GaAs was used to demonstrate that the reflected electron signal varies nonmonotonically near the heterojunction. The line profiles of the reflected electrons have a maximum and minimum in the intensity on opposite sides of the interface, which is due to the anisotropy of the energy spectrum of the reflected electrons at the heterojunction.[9] For the structures studied in this investigation, the analogous reflected electron profiles were observed only for the heterojunctions between InAsSbP layers with different phosphorous content.

As one can see from Fig. 1, the reflected electron yield for the InAsSbP layers is greater than for the compounds InAs or InAsSb. However, the profile of the reflected electron signal measured at sharp InAsSbP–InAs or InAsSbP–InAsSb heterojunctions is considerably different from the profiles of the reflected electrons for the system AlGaAs–GaAs and has the form of a zigzag curve (Fig. 2a). We shall show that these variations in the reflected electron signal as the electron beam moves towards the interface are due to the difference in the stopping power of the materials composing the heteropair,[9] whereas the jump in the reflected electron signal at the heterojunction is related to the forward-scattering properties of the electrons in the quaternary InAsSbP solid solutions compared to the binary and ternary compounds. It should be noted that the zigzag shape of the reflected electron profile with the jump at the heterojunction is characteristic of sharp interfaces. The less sharp the interface the smaller and more washed out is the jump in the reflected electron signal. For smooth (diffused) heterojunctions the jump not there at all (Fig. 2b).

To execute the method for determining the position of the $p-n$ junction in structures based on narrow-gap semiconductors, we propose to make the measurements at low temperatures, near the temperature of liquid nitrogen. At lower temperatures the leakage current in these structures is considerably lower, which permits measurements of the current signal induced by the electron probe.

To measure the current signal induced by the electron probe we used a highly accurate low-noise amplifier, with which it is possible to measure the current signal induced by the electron probe for probe currents $I_b<10^{-12}$ A. The experiments were carried out at temperatures in the range $T=81$–300 K by an automated apparatus based on a Can-

Scan Series 4-88 DV100 scanning electron microscope with a cooling stage to cool samples to $T=77$ K. The laser we studied was clamped on a specially designed attachment, which then was affixed to the regular stage.

Even in those rare situations where it was possible to measure the signal current induced by the electron probe at $T=300$ K, cooling of the sample greatly enhanced the signal-to-noise ratio, and consequently the accuracy of the determination of the position of the $p-n$ junction (Fig. 3). Of course, by applying the method used to process the curve of the current induced by the electron probe, one can obtain information on the diffusion lengths, the surface recombination velocity, and the interface recombination velocity of the minority carriers. A positive aspect is that these parameters can be determined for the temperatures at which the laser operates.

In summary, we have demonstrated new potentials for identifying heteroboundaries, monitoring the sharpness of interfaces, and also determining the position of the $p-n$ junction in lasers based on InAsSb/InAsSbP by using scanning electron microscope methods. By the proposed method it is possible to optimize the parameters of long-wavelength laser structures based on InAsSb/InAsSbP and obtain record low threshold currents ($I_{th}\leqslant 25$ mA at 77 K) in the lasing wavelength range $\lambda=3$–3.5 μm (Ref. 5).

This work was carried out with the partial support of the United States European Division of Aerospace Research and Development, Contract No. F61708-96-W0078.

[1] A. N. Baranov, A. N. Imenkov, V. V. Sherstnev, and Yu. P. Yakovlev, Appl. Phys. Lett. **64**, 2482 (1994).
[2] H. K. Choi, S. Y. Eaglash, and Turner, Appl. Phys. Lett. **64**, 812 (1994).
[3] Y. H. Zhang, Appl. Phys. Lett. **66**, 118 (1995).
[4] T. N. Danilova, O. G. Ershov, A. N. Imenkov, M. V. Stepanov, V. V. Sherstnev, and Yu. P. Yakovlev, Fiz. Tekh. Poluprovodn. **30**, 1244 (1996) [Semiconductors **30**, 656 (1996)].
[5] A. Popov, V. Sherstnev, Yu. Yakovlev, R. Muecke, and P. Werle Spectrochimica Acta Part A. **52**, 863 (1996).
[6] A. I. Nadezhdinski, and A. M. Prokhorov SPIE **1724**, 2 (1992).
[7] J. I. Goldstein, *et al.*, *Scanning Electron Microscopy and X-Ray Microanalysis* (Plenum Press, New York, 1981) [Mir, Moscow, 1984].
[8] V. A. Solov'ev, S. A. Solov'ev, and V. E. Umanskiĭ, Izv. Akad. Nauk SSSR Ser. Fiz. **54**, 232 (1990).
[9] L. A. Bakaleĭnikov, S. G. Konnikov, V. A. Solob'ev, and V. E. Umanskiĭ, Izv. Akad. Nauk SSSR Ser. Fiz. **51**, 458 (1987).

Translated by J. R. Anderson

One-dimensional chain of maps with unidirectional threshold coupling

A. A. Koronovskiĭ

N. G. Chernyshevskiĭ Saratov State University, State Educational Science Center ''Kolledzh''
(Submitted November 19, 1996)
Pis'ma Zh. Tekh. Fiz. **23**, 61–66 (March 26, 1997)

A study is made of a loop of logical transformations, semi-infinite or closed in a ring, with a fundamentally new type of coupling, which we call unidirectional threshold coupling. The chain is a unidirectional series-coupled union of bistable elements, whose switching from one state to the other requires a finite time. © *1997 American Institute of Physics.* [S1063-7850(97)02903-0]

Systems with a discrete time are widely studied by physicists and mathematicians.[1,2] The interest in systems with a discrete time is due first to their relative simplicity and the possibility of being studied quickly for a broad range of variation of the control parameters; second, in the language of systems with discrete time, the possibility of clearly and transparently elucidating the nature of chaotic dynamics and the scenarios for the transition from periodic to chaotic oscillations.[3,4] In addition, by means of maps, including those based on the logistic map, a broad class of coupled maps have been constructed, chains and lattices of maps that modulate distributed systems and play an important role in helping to understand the dynamics of similar systems.[5–8]

In this paper we shall investigate a chain of logistic maps (semi-infinite or closed in a ring) with a fundamentally new type of coupling, which I call unidirectional threshold coupling. The dynamics of such a chain is described by maps of the form

$$x_{ij+1}=x_{ij}[a-x_{ij}\pm s\cdot\tanh(k(x_{i-1j}-x_s))],$$

where i is the spatial coordinate of an element of the chain and j is the discrete time. If the chain consists of N elements and is closed in a ring, then we have the relation

$$x_{1j+1}=x_{1j}[a-x_{1j}\pm s\cdot\tanh(k(x_{Nj}-x_s))].$$

Since the coupling is fundamentally new, it may be expected that the behavior of the chain will differ from that of chains of logistic maps with the ''traditional'' types of couplings (for example, with dissipative coupling), which are widely discussed in the literature (see, e.g., Ref. 9). The parameters a and s are chosen so that in the absence of the coupling the behavior of each element of the chain does not exhibit any complex dynamics. With the coupling the behavior of each element of the chain corresponds to the attracting point $x^*_{ij+1}=a-1\pm s\cdot\tanh(k(x_{i-1j}-x_s))$ (as $k\to\infty, x^*_i=a-1\pm s$) if the value in the adjacent $(i-1)$ element is less than a certain threshold x_s. If the value of x_{i-1j} exceeds this threshold, the behavior of the ith element corresponds to the attracting point $x^*_{ij+1}=a-1\mp s\cdot\tanh(k(x_{i-1j}-x_s))$ (for $k\to\infty$, $x^*_i=a-1\mp s$). Later we shall examine a chain described by the map

$$x_{ij+1}=x_{ij}[a-x_{ij}+s\cdot\tanh(k(x_{i-1j}-x_s))].$$

It is entirely understandable that if a given semi-infinite chain is left to itself, then after a transition process one of two equilibrium states will be set up in it, depending on the value of the first element: $x^0_{ij}>x_s$ if $x_{1j}>x_s$ and $x^0_{ij}<x_s$ if $x_{1j}<x_s$. Indeed, such a chain is a sequence of unidirectionally coupled bistable elements, for which the transition from one of the states to the other occurs after a finite time (in the present case we have in mind a discrete time). It is also clear that if an external agent is applied at the entrance to such a chain (since the chain consists of bistable elements, it makes sense hereafter to consider a rectangular pulse of a certain duration), then the perturbation begins to propagate from the entrance of the chain, initiated by this external agency. How will the external perturbation introduced into the semi- infinite chain evolve as $t\to\infty$? At first we can envision three scenarios for the development of the events: First, an external agency in the form of a rectangular pulse can begin to propagate almost without distortion with a constant velocity in the direction determined by the (unidirectional) coupling of the previous element with the succeeding element. Such a situation is possible if the leading and trailing edges of the pulse travel with the same velocity, which in turn, is determined by the time required for the transition of any element of the chain from one state to the other, and thus, ultimately by the parameters of the medium. If our system is closed in a ring, then the introduced pulse will circulate over the chain forever if the length of the chain is greater than the duration of the perturbation multiplied by the velocity of propagation of the pulse; otherwise all the elements of the chain will remain in the ''perturbed'' state.

Second, it may happen that the leading edge of the pulse propagates faster than the trailing edge (in other words, the time for an element of the chain to make the transition from the unperturbed state ($x^0_{ij}<x_s$) to the perturbed state ($x^0_{ij}>x_s$) is shorter than the reverse); then the leading edge ''runs away'' from the trailing edge and an expanding rectangular pulse travels over the chain. One can understand that in a chain of elements closed in a ring the leading edge of the pulse will overtake the trailing edge and all the elements will end up in the perturbed state.

Finally, the leading edge of the pulse can travel slower than the trailing edge, and then the propagating pulse will steadily shrink until the trailing edge of the pulse reaches the leading edge, and then the pulse collapses. Obviously, the same thing will happen for a chain closed into a ring.

As one can infer from this discussion, all three scenarios are possible for the development of events in a chain (which,

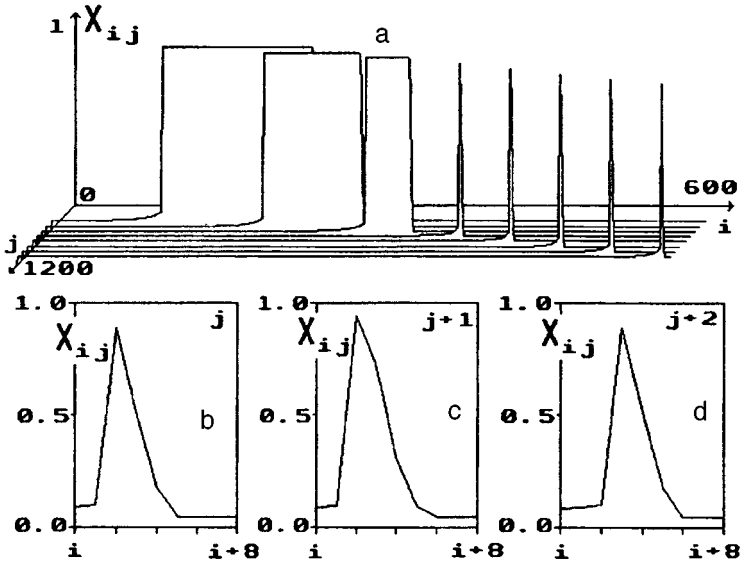

FIG. 1. An external perturbation transformed into a solitary pulse propagating thereafter in a chain (a). Profile of the solitary pulse at three sequential discrete times (b–d).

in fact can be considered as a discrete model of some medium), depending on the parameter values: for $x_s=0.095$ the pulse travels along the chain with a constant length and a constant velocity; for $x_s=0.08$ the pulse expands as it travels, and for $x_s=0.22$ the pulse shrinks, and after a certain interval of discrete time it collapses. (the parameter values are $a=1.5$ and $s=0.45$).

However, there is yet one more possible scenario for the propagation of a perturbation introduced into a chain, which is realized for the parameter values $a=1.5$, $s=0.45$, $k\to\infty$, and $0.096<x_s<0.215$. The trailing edge of the rectangular pulse travels faster than the leading edge, but when the trailing edge catches up with the leading edge, the pulse does not collapse, but rather a solitary pulse travels over the chain (Fig. 1a). This pulse is stable in the sense that any initial perturbation that has an amplitude larger than x_s and a duration longer than that of the solitary pulse, which is determined by the parameters of the medium, and is introduced into the chain over a certain interval time is converted into this solitary pulse. It is noted that the solitary pulse cannot be called ''stationary'' (by analogy with stationary waves in continuous media; see, e.g., Ref. 10), since its profiles at

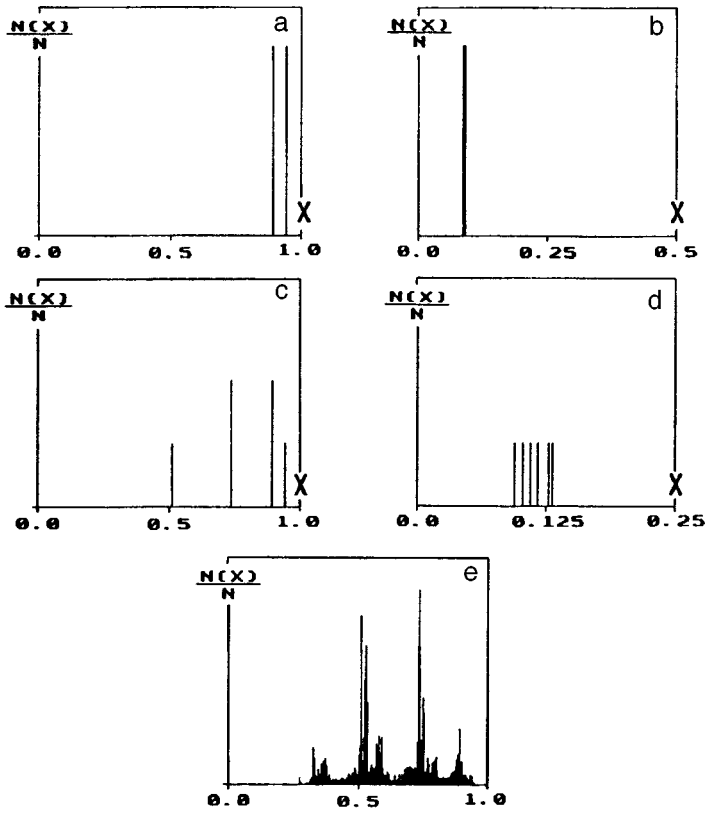

FIG. 2. Histograms of a solitary pulse for different parameter values (a–d).

different discrete times are different. Figures 1b–d show the profiles of a solitary pulse propagating over a chain at three consecutive discrete times, j, $(j+1)$, and $(j+2)$ for $x_s=0.1$. From these figures it can be seen that the solitary pulse is stable spatial structure that varies periodically in discrete time with a period 2. A similar situation occurs in the cells of an automaton (see, e. g., the game of ''life''; Ref. 11). It should be pointed out, however, that the profile of a solitary pulse can change with a complex period, or chaotically. Figure 2 shows histograms for the characteristic points of the pulse profile for various parameter values: Fig. 2a shows the histogram for the peaks of the solitary pulse for the parameter values $a=1.5$, $s=0.45$, $k\to\infty$, and $x_s=0.1$, while Fig. 2b shows the histogram for a point of the solitary pulse two spatial units away from the peak of the pulse (for the same parameter values). Figure 2c and d show histograms for these same two points for parameter values $a=1.5$, $s=0.45$, $k\to\infty$, and $x_s=0.15$, and Fig. 2f is a histogram for the peak of the solitary pulse for $a=1.5$, $s=0.45$, $k=100$, and $x_s=0.19$. This figure shows that the profile of the solitary wave is a stable structure with chaotic dynamics, propagating in the chain.

In conclusion, I would like to thank D. I. Trubetskov for his steady interest and support, and also V. I. Ponomarenko for valuable advice that I used in writing this paper.

[1] K. Kaneko, *Theory and Applications of Coupled Map Lattices* (John Wiley and Sons, Chichester, 1993).
[2] A. N. Sharkovskiĭ, S. F. Kolyada, A. G. Sivak, and V. V. Fedorenko, *Dynamics of One-Dimensional Maps* [in Russian] (Naukova Dumka, Kiev, 1989).
[3] A. P. Kuznetsov and S. P. Kuznetsov, Izv. Vyssh. Uchebn. Zaved. PND **1**(1,2), 15 (1993).
[4] A. P. Kuznetsov and S. P. Kuznetsov, Izv. Vyssh. Uchebn. Zaved. PND **1**(3,4), 17 (1993).
[5] A. P. Kuznetsov and S. P. Kuznetsov, Izv. Vyssh. Uchebn. Zaved. Radiofiz. **34**(10, 11, 12) (1991).
[6] A. P. Kuznetsov, S. P. Kuznetsov, and I. R. Sataev, Izv. Vyssh. Uchebn. Zaved. Radiofiz. **34**, 357 (1991).
[7] S. P. Kuznetsov, Pis'ma Zh. Tekh. Fiz. **9**, 94 (1983) [Sov. Tech. Phys. Lett. **9**, 41 (1983)].
[8] A. P. Kuznetsov and S. P. Kuznetsov, Izv. Vyssh. Uchebn. Zaved. Radiofiz. **34**, 142 (1991).
[9] V. V. Astakhov, B. P. Bezruchko, V. I. Ponomarenko, and E. P. Seleznev, *Lectures on Microwave Electronics and Radiophysics*, 10th Winter School-Seminar: Inter-University Collection of Scientific Papers, Book 2 (Published by GosUNTs ''Kolledzh,'' Saratov, 1996).
[10] A. Scott, *Active and Nonlinear Wave Propagation in Electronics* (Wiley, New York, 1970) [Russ. transl., Sov. Radio, 1977].
[11] M. Gardner, *Krestiki-Noliki* [Russian translation] (Mir, Moscow, 1988).

Translated by J. R. Anderson

Frictional self-oscillations caused by deformation of the irregularities of the contacting surfaces

F. M. Borodich and I. V. Kryukova

Moscow Institute of Radio Engineering, Electronics, and Automation
(Submitted November 27, 1996)
Pis'ma Zh. Tekh. Fiz. **23**, 67–73 (March 26, 1997)

A numerical simulation is carried out for the dynamic processes caused by friction during the sliding of solid bodies. It is shown that frictional self-oscillations can arise even in a purely elastic system, in which there is no difference between the static and dynamic coefficients of friction, and the material at each point of a rough surface is deformed linearly. © *1997 American Institute of Physics.* [S1063-7850(97)03003-6]

The theoretical and experimental study of the dynamical processes due to the friction generated when two normal planes slide past each other has been the subject of a large number of papers (see, e.g., the review, Ref. 1). In the theoretical models the following assumptions are almost always made: the irregularities of the body can be neglected; the motion occurs only along the nominal contact plane; the friction is described by the modified Amantons law. The last assumption means that the static and dynamic coefficients of friction differ, and the coefficient of friction as a function of the relative velocity of the sliding bodies has the following form: it is antisymmetric, it has vertical segments corresponding to resting friction, and then it falls off monotonically or discontinuously, always concave to the horizontal axis. This dependence has also been applied in a somewhat different form: it falls off at first and then begins to rise.[2,3]

Within these assumptions, simulations have been carried out, with greater or lesser thoroughness, for a number of complex physical processes, up to self-oscillations of violin strings and chaotically oscillating systems undergoing external and internal excitations.[2–5] Nevertheless, no detailed description exists for the underlying causes of the difference between static and kinetic friction.

Many experiments have been done that support the hypothesis that the basic cause for this difference is the motion (oscillation) of the body in the plane perpendicular to the sliding plane.[6,7] Of these hypotheses, the one that has been developed to the greatest extent is presented in Ref. 1, which considered the classical system: a sliding block, slides with friction over moving conveyor belt that pulls on a horizontal spring. This system permits the motion of the sliding block in two directions (vertically and horizontally). A numerical simulation showed that self-oscillations of the block can occur even in the absence of local maxima corresponding to resting friction. The main feature of this model, that which permits the system to exhibit this behavior, was the presence of a phenomenological nonlinear viscous-elastic dependence between the proximity of the two bodies and the contact force.

We present here the results of a numerical simulations that show that frictional self-oscillations can arise even in a purely elastic system, in which no artificial differences between the static and dynamic coefficients of friction are introduced, and the material at each point of the rough surface deforms according to a linear-elastic law. This seemingly paradoxical result is obtained within one of the models advanced in Ref. 8. This model, like the model of Ref. 1, permits motion in two mutually perpendicular directions and rejects the Amanton law. However, unlike in Ref. 1, the present model explicitly introduces a function that describes the roughness of the contacting surfaces.

Let us consider a sliding block of length $2a$ and unit mass M lying on a belt moving with a constant velocity U. As the block moves it pulls on a horizontal spring with a spring constant k_x. In the calculations we use the following coordinate system: absolute coordinates (x,y) and local coordinates (ξ_s, η_s) for the block and the belt, respectively (Fig. 1).

We assume that the block and the belt are rigid and planar, but each surface is covered with a deformable rough

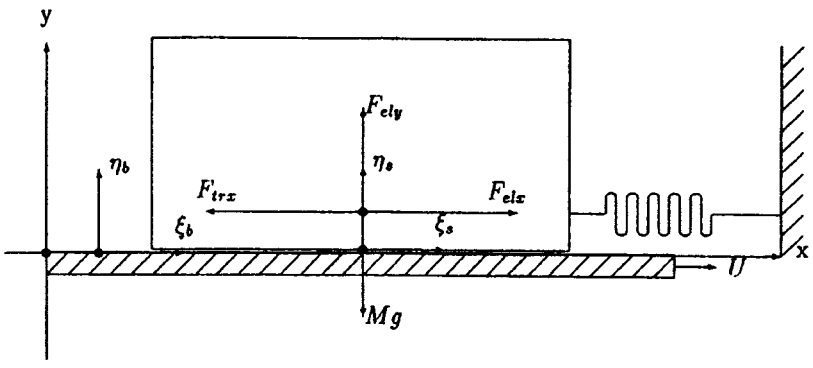

FIG. 1. General diagram of the model and the system of coordinates.

 1063-7850/97/030239-03$10.00

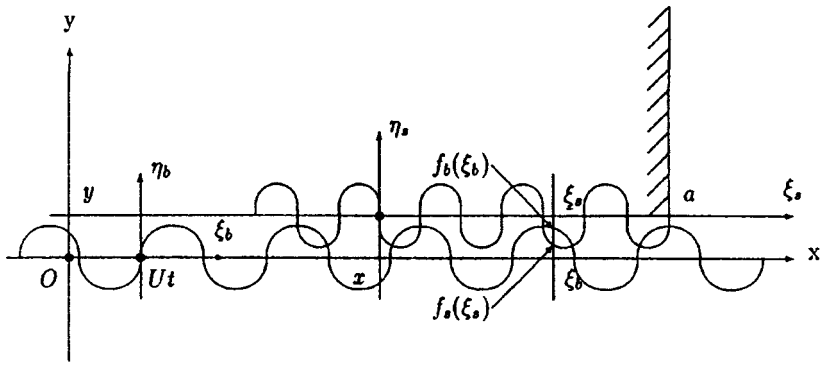

FIG. 2. Schematic depiction of the contact between the block and the belt.

layer. In the local coordinate system the rough surfaces of the block and the belt are described by the functions f_s and f_b, respectively. The first approximation in the calculations is taken as

$$f_b(x)=a_b \sin(\omega_b x), \quad f_s(x)=a_s \sin(\omega_s x). \tag{1}$$

In this model it is also assumed that these surfaces consist of linearly elastic springs all with the same stiffness ϵ. It is clear that if the distance between the belt and the block is small, then the irregularities of the two surfaces partially overlap (Fig. 2).

Then the force of elastic interaction F_{ely} will be equal to the integral of all the local elastic interaction forces over the entire length of the block

$$F_{ely}=\int_{-a}^{a}\Phi(\xi)d\xi, \tag{2}$$

where

$$\Phi(\xi)=b\epsilon_s\Psi(f_b(\xi+x-Ut)-f_s(\xi)-y).$$

One can readily see that the local deformation function vanishes if the irregularities at a given point do not interact, i.e.,

$$\Psi(x)=x \text{ for } x>0 \text{ and } \Psi(x)=0, \quad x<0.$$

In a numerical modeling the function $\Psi(x)$ is described by the smoothed function

$$\Psi(x)=x(1/\pi \arctan(\alpha_2 x)+1/2)+1/\pi, \quad \alpha_2=1.$$

Similarly, for the numerical modeling, the jump in the force of friction is smoothed out and the coefficient of friction in the Coulomb law is taken as

$$\text{sign}(x)=2/\pi \arctan(\alpha_1 x), \quad \alpha_1=100.$$

Thus the dynamic behavior of the system for a sliding block of unit mass is described by the system of equations

$$\ddot{x}(t)=F_{frx}(F_y,\dot{x}-U)+F_{elx}(x-\alpha_0), \quad \alpha_0=0, \tag{3}$$

$$\ddot{y}(t)=F_{ely}-g, \quad g=9.81\times10^3, \tag{4}$$

where F_{elx} is the elastic resistance force of the spring, F_{frx} is the force of friction.

In the calculations we used the following parameter values: the stiffness of the springs representing the irregularities is $\epsilon=10$ per spring, the width of overlap of the contacting surfaces is $b=4.0$, the amplitudes of the surface roughness functions of the belt and of the block are $a_b=a_s=1.0$, the frequencies of the surface roughness functions on the belt and on the block are $\omega_b=1.0\times10^5$ and $\omega_s=3.0\times10^5$, respectively, and the stiffness of the horizontal spring is $k_x=10$. The system of equations (3)–(4) was solved by the Runge-Kutta method with the integration done by Simpson's rule at each step of the iteration. The initial values were

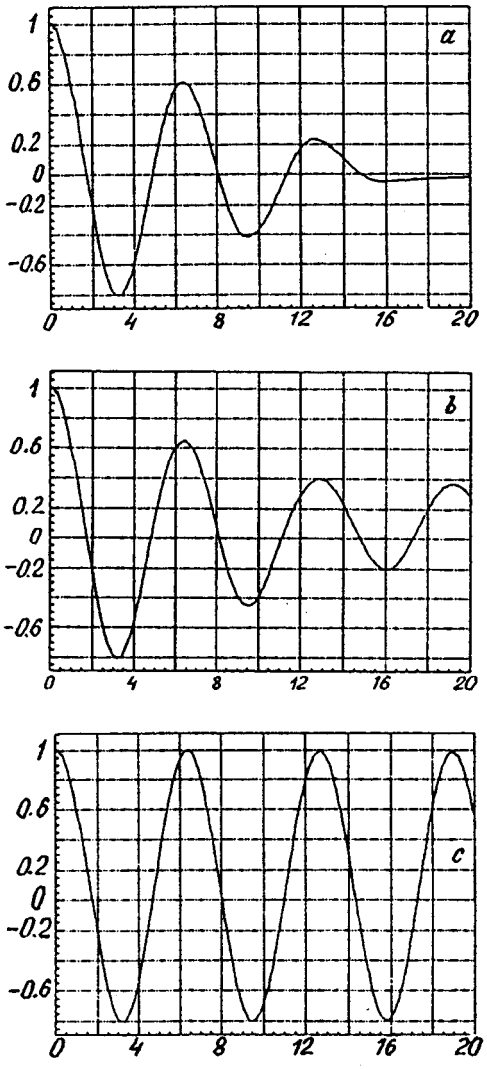

FIG. 3. Time dependence of the coordinate x of the center of mass of the block: a — $U=0.0$, b — $U=0.3$, c — $U=1.0$.

$x(0)=1.0$, $\dot{x}(0)=0.0$, $y(0)=2.0$, and $\dot{y}(0)=0.0$.

In Fig. 3 we show some results of the calculations, specifically the time dependence of the x coordinate of the center of mass of the block for various belt velocities.

One can see that for $U=0.0$ the horizontal oscillations are quickly damped, while for $U=0.3$ they are damped more slowly. For $U=1.0$, frictional self-oscillations arise which are sinusoidal.

It is obvious that this model permits one to analyze any arbitrary surface roughness function, and not only a function of the form (1). It is also easy to model the roughness not by a layer of springs of the same stiffness, but by a layer of elastic rods of equal height, as proposed in Ref. 8.

We note that in almost all investigations of the deformation of the irregularities of contacting surfaces the models that are used are based on the Greenwood-Williams model[1] This model is based on the solution of the Hertz problem, in which the contact between two curved surfaces reduces to the problem of contact between a planar surface and an equivalent curved surface. While this model gives good results in the static case, when it is applied to dynamical problems it may omit certain important details, since the dependence of the force of contact on the proximity of the bodies is the same for any relative displacement of the bodies along the contact plane. One of the important features of this model, in contrast to those used previously, is that both surfaces are rough, and therefore with a relative displacement of the contacting surfaces the distribution of the mutually overlapping irregularities changes, and consequently the integrated dependence of the contact force on the proximity of the bodies will vary with the displacement of the block from point to point.

By taking the surface roughness and the vertical oscillations of the block into account explicitly, we were able to demonstrate that frictional self-oscillations are possible in an elastic system in which no artificial differences between the static and dynamic coefficients of friction are introduced.

The authors wish to thank A. P. Kryukov for his kind attention to this investigation and for stimulating discussions. The first author thanks the Alexander von Humboldt Foundation for financial support of his work at Hannover University, where this work was completed.

[1] J. A. C. Martins, J. T. Oden, and F. M. E. Simões, Int. J. Eng. Sci. **28**, 29 (1990).
[2] A. A. Witt, Zh. Tekh. Fiz. **6**, 1459 (1936).
[3] A. Witt, Tekhn. Phys. of USSR. **4**, 261 (1937).
[4] K. Magnus, *Schwingungen* (Teubner, Stuttgart, 1961).
[5] K. Popp and P. Stelter P. Philos. Trans. R. Soc. London. Ser. A. **332**, 89 (1990).
[6] B. V. Budanov, V. A. Kudinov, and D. M. Tolstoĭ, Trenie Iznos **1**, 79 (1980).
[7] M. E. Levinshteĭn and S. L. Rumayntsev, Pis'ma Zh. Tekh. Fiz. **18**(5), 42 (1992) [Sov. Tech. Phys. Lett. **18**, 144 (1992)].
[8] F. M. Borodich, in *Abstracts of the First European Nonlinear Oscillations Conference*, TU Hamburg-Harburg, 1993, p. 20.

Translated by J. R. Anderson

Minimum concentration of surface-active material required for damping of capillary waves

D. F. Belonozhko, A. I. Grigor'ev, and S. O. Shiryaeva

Yaroslavl' State University
(Submitted December 9, 1996)
Pis'ma Zh. Tekh. Fiz. **23**, 74–79 (March 26, 1997)

It is shown that for low concentrations of surface-active and surface-inactive materials dissolved in a liquid, their effect on the behavior of capillary wave motion differs from the case of standard concentrations: the surface-active material does not cause the capillary wave damping, while the surface-inactive material does not destroy the stability of the free surface of the liquid. The presence of an electric charge on the free surface of the liquid weakens the phenomenon. © *1997 American Institute of Physics.* [S1063-7850(97)03103-0]

The damping of capillary waves by surface-active material has been known for a long time. The basic theory of the phenomenon has been described in Ref. 1, and the number of papers concerned with the study of this phenomenon continues to grow steadily. Nonetheless, some aspects of the damping effect have not yet been studied. The first is the relation between the effective elasticity of the film and its ability to damp capillary waves. There has been little study of the effect of inactive surface materials on the motion of capillary waves with a surface electric charge or the possible interaction of surface-active material with a surface electric field, which the free surface of a liquid can maintain.[2]

We shall study the problem of calculating the spectrum of capillary motion in an ideally conducting medium of infinite depth in a gravitational field **g** and an electrostatic field **E**, both normal to the free surface. We assume that the liquid has a density ρ, a kinematic viscosity ν, and a surface-active material dissolved in it to a concentration C. This material will emerge by diffusion to the surface and form a film on it with a surface concentration Γ_0 in the unperturbed state. This film is assumed to be completely entrained into the motion of the liquid surface. We denote the surface tension of the liquid with the surface-active medium as σ, and μ_n and μ_p are the chemical potentials of its volume and surface phases. The relaxation time of the active material between the surface and the bulk region of the solvent adjacent to the surface is small compared to the period $2\pi/\omega_0$ of the perturbation, which is produced by a wave with a frequency ω_0. This means that the surface and bulk solutions are always in a state of equilibrium. The electric field **E** at the liquid surface is determined by the potential difference between the electrodes: the lower electrode is the conducting liquid itself — one can apply a potential $\Phi_1=0 (z\to-\infty)$, and parallel to the surface of the liquid in the absence of any perturbations, and the upper counter electrode, located a distance b from the surface, and having a potential $\Phi_2=V$.

Consider now a Cartesian coordinate system arranged so that the z axis is points upward: $\mathbf{n}_z \| -\mathbf{g}$ (here $\mathbf{n}_z$ is the unit vector of the Cartesian coordinate z), and the x axis is along the direction of motion of the planar capillary wave, $\sim\exp(st+ikx)$. We have the plane $z=0$ coincide with the free unperturbed surface of the liquid (s is the complex fre-

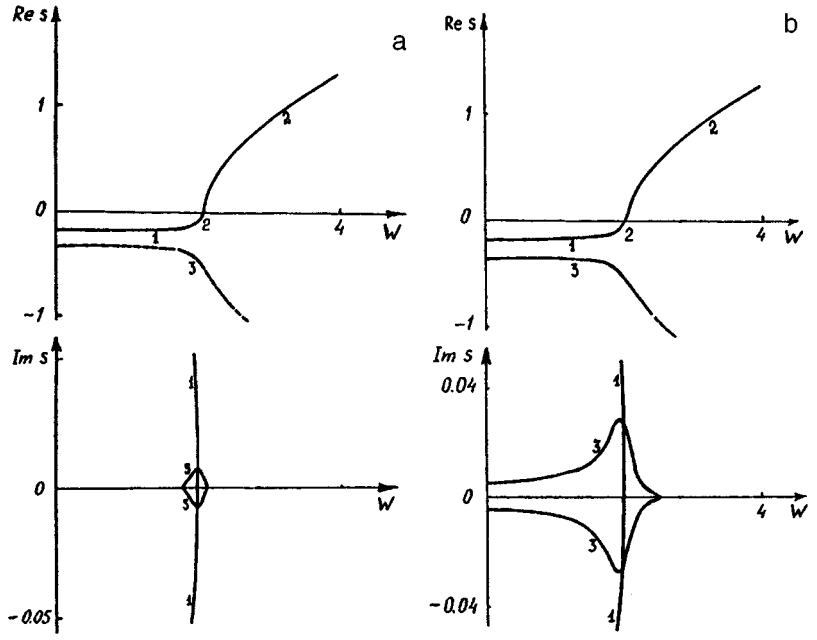

FIG. 1. Curves of $\mathrm{Re}\, s = \mathrm{Re}\, s(W)$ and $\mathrm{Im}\, s = \mathrm{Im}\, s(W)$ for a liquid covered with a film of surface-active material, plotted against the dimensionless parameter W, which characterizes the surface charge density, calculated for $k=1$, $\nu=0.1$, $L=500$, $D=3\times10^{-6}$, and $D_*=3\times10^{-5}$. a — $\chi_0=-0.097$, b — $\chi_0=-0.11$.

quency, k is the wave number t is the time, and i is the imaginary unit). The function $\xi(x,t)=\xi_0\exp(st+ikx)$ describes a small disturbance of the equilibrium plane of the liquid surface, caused by thermal capillary wave motion of extremely small amplitude ($\xi_0\sim(kT/\gamma)^{1/2}$); k is Boltzmann's constant, T is the absolute temperature; $\mathbf{U}(\mathbf{r}t)$, the velocity field of the liquid caused by the perturbation $\xi(x,t)$, has the same order of smallness.

In dimensionless variables, where $g=\rho=\sigma=1$, the dispersion equation of the capillary motion of the liquid has the form[2]

$$-s^2(s+2\nu k^2)^2\{s+D_*k^2+L\sqrt{D(s+Dk^2)}\}+\omega_0^2\{\chi_0 k^2 s \times(k-\sqrt{k^2+s/\nu})-s^2(s+D_*k^2+L\sqrt{D(s+Dk^2)})\} +4\nu^2k^3s^2\{s+D_*k^2+L\sqrt{D(s+Dk^2)}\}\sqrt{k^2+s/\nu} -s^3\chi_0k^2\sqrt{k^2+s/\nu}=0; \quad (1)$$

$$\chi_0=\frac{\partial\sigma}{\partial\Gamma}\Gamma_0; \quad L=\left(\frac{\partial\mu_n}{\partial\Gamma_0}\right)\Big/\left(\frac{\partial\mu_p}{\partial C_0}\right); \quad W=\frac{\varepsilon E_0^2}{4\pi};$$

$$E_0=V/b; \quad \omega_0^2=k^3+K-Wk^2\coth(kb),$$

where D^* is the surface diffusion coefficient of the surface-active material, W characterizes the pressure of the electric field on the charged surface of the liquid, or, equivalently, the surface charge density. The quantity χ_0 has the meaning of the elastic constant of the surface film of this material, and varies between -1 and $+1$. The range of values $\chi_0<0$ corresponds to an ordinary active material, which reduces the surface tension σ of the free surface, while the range $\chi_0>0$ corresponds to the inactive materials, which increase σ; the quantity L is the reciprocal characteristic length of variation of the bulk concentration of the surface-active material near the surface $L\sim(\sigma D^2/\rho g^3)^{-1/4}$ and in practice is determined by the slope of the adsorption isotherm $\Gamma=\Gamma(C)$.

A numerical analysis of the dispersion equation (1) shows that in addition to the usual capillary motion of the liquid, which occurs in the absence of the material, two additional damping waves appear in this situation: one associated with wave motion in the elastic film and the other with the flow of material diffusing to the surface from the bulk of the liquid.[2] The range $\chi_0<0$ corresponds to damping of the surface waves by the film, and is due to waves that form in the film, as has been shown theoretically and experimentally in Refs. 3–6. However, numerical calculations show that the wave motion in the film (and thus the damping effect) exists not for just any values of χ_0, but only for $\chi_0<-0.11$. The reason for this lies in the negative feedback between the concentration Γ_0 of the surface-active material on the free surface of the liquid and the bulk concentration C_0: for low Γ_0 (small values of χ_0) the inhomogeneities induced in its concentration distribution over the surface by the thermal capillary wave do not create a surface wave associated with the redistribution, but are rapidly compensated by flows that arise from the bulk of the liquid normal to the free surface. The presence of uncompensated electric charge on the free surface extends the region where the damping effect occurs.

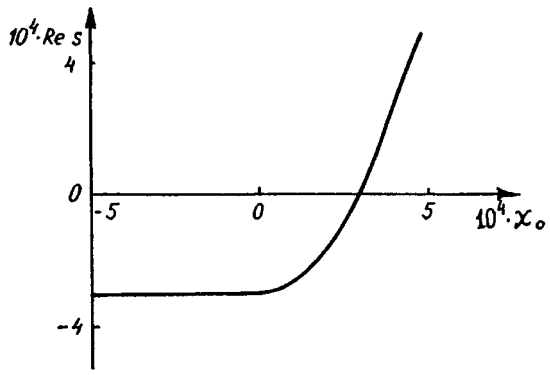

FIG. 2. Curve of $\mathrm{Re}\,s=\mathrm{Re}\,s(\chi_0)$ for a liquid containing a dissolved surface-inactive materials, plotted against the dimensionless parameter χ_0, which is the elastic constant of the film of the active material, calculated for $k=1$, $\nu=0.1$, $L=500$, $D=3\times10^{-6}$, and $D_*=3\times10^{-5}$; $W=2$.

For example, with a high enough surface charge density W, wave motion appears in the film even for $\chi_0>-0.11$, or more precisely, at $\chi_0=-0.097$. When χ_0 decreases from $\chi_0=-0.097$ to $\chi_0=-0.11$, the region of existence of wave motion in the film expands along the W axis to $W=0$.

The results of a numerical analysis of the dispersion equation (1) are illustrated in Fig. 1a,b, where the real part of the complex frequency, Re s, and the imaginary part Im s are plotted as functions of the parameter W for various negative values of χ_0.

Figure 2 shows $\mathrm{Re}\,s=\mathrm{Re}\,s(\chi_0)$ for the region of inactive materials: $\chi_0>0$, which, as shown in Ref. 2, are able to destabilize the free surface of a liquid. The range of values $\mathrm{Re}\,s>0$ determines the growth increment of the corresponding instability as a function of χ_0. However, for small values of χ_0, because of the negative feedback, destabilization of the free liquid surface by inactive materials does not occur: the curve $\mathrm{Re}\,s=\mathrm{Re}\,s(\chi_0)$ for $\chi_0\to+0$ moves from the region $\mathrm{Re}\,s>0$ to the region $\mathrm{Re}\,s<0$, to the right of the origin, and falls off monotonically to $\chi_0=0$, passes into the region $\chi_0<0$, in which there is essentially no change up to $\chi_0=-1$, and stops at parameter values that are comparable in absolute magnitude with the bulk diffusion coefficient D.

The conclusion common to the usual and inactive surface materials reduces to the damping of their effect on capillary oscillations at low concentrations and the stability of the free liquid surface due to the formation of liquid flows in the bulk, normal to the free surface. This effect does not occur for insoluble surface-active materials.

[1] V. G. Levich, *Physico-Chemical Hydrodynamics* [in Russian] (Fizmatgiz, Moscow, 1959).
[2] D. F. Belonozhko, S. O. Shiryaeva, and A. I. Grigor'ev, Pis'ma Zh. Tekh. Fiz. **22**(15), 60 (1996) [Tech. Phys. Lett. **22**, 626 (1996)].
[3] R. Dorrenstein, Proc. K. Ned. Akad. Wet. **354**, 350 (1951).
[4] J. T. Davies and R. W. Vose, Proc. R. Soc. London Ser. A **286** 219 (1965).
[5] E. H. Lucasen-Reynders and J. Lucasen, Adv. Colloid Interface Sci. **2**, 347 (1969).
[6] W. Albers and H. Hünerfuss, J. Geophys. Res. **94**, C5, 6251 (1994).

Translated by J. R. Anderson

Control of the morphology of *n*-type porous silicon

É. Yu. Buchin and A. V. Prokaznikov

Institute of Microelectronics, Russian Academy of Sciences, Yaroslavl'
(Submitted April 26, 1996)
Pis'ma Zh. Tekh. Fiz. **23**, 80–84 (March 26, 1997)

The morphology of layers obtained by anodic etching is related to the current-voltage characteristics of the electrolytic cell during the etching. By etching at various points of the current-voltage characteristic one can obtain porous silicon with various structures. © *1997 American Institute of Physics.* [S1063-7850(97)03203-5]

Porous silicon has attracted the attention of scientists of many groups because of the broad range of its physicochemical properties, as well as the multitude of properties of the structures produced by a single silicon technology. Most of its physical-chemical characteristics are closely linked with the properties of the morphology of its porous structure. The morphological aspect of the complex of problems has not yet been investigated adequately.[1] Despite the existence of papers reporting studies of preparing porous silicon and controlling its properties, there is still no common theory for pore formation in silicon or other semiconductors.[1]

Possible ways to control the morphology of lightly-doped *n*-type porous silicon have been sought in Refs. 2–5. Macropores in the form of vertical channels perpendicular to the surface have been observed in Ref. 2. In Ref. 4 it has been shown that with an increase in such parameters as the illumination intensity and the anodization time, and with a decrease in the current density, the amorphization of the surface is enhanced during the anodization in concentrated hydrofluoric acid (HF), while the pores branch out into a lower part to form microstructures.[5] In Ref. 3 it was noted that when the wavelength of the illumination was changed during anodization in dilute HF solutions the external profile of the macrochannels can change from cylindrical to conical.

It has been observed[6–8] that in the anodization of *n*-type silicon in a mixture of HF with isopropyl alcohol (1 : 1 by volume), four types of pore morphology appear, which are formed with specific combinations of the parameters involved in the anodization, a correlation was observed between the type of morphology and the properties of the photoluminescence spectra, and it was shown possible to control the generation of porous silicon consisting of alternating structures with different types of morphology.

We have studied the current-voltage characteristics ($I-V$ characteristics) taken under various conditions of anodization corresponding to the formation of the four main types of pore morphology, and also advanced a theoretical explanation of the behavior of the characteristics and the formation of the main types of morphology.

The experimental method and the method for taking the $I-V$ characteristics for a system consisting of a silicon anode (type KÉF silicon) and the electrolyte (a mixture of HF with alcohol) were carried out in the standard way, described in Refs. 4–7. The rate of linear sweep of the stabilized voltage was 10 V/s.

The general shape of the $I-V$ characteristics for the parameter values noted is shown in Figs. 1 and 2; it is similar to that published in Refs. 4, 9, and 10. The $I-V$ characteristics can nominally be divided into four sections. The first is the initial part of sharp rise, the second is the upper part of the sharp rise, the third is the current saturation (plateau) region, and the fourth is the second part of rise. The external shape of the $I-V$ characteristics is determined by the following parameters: the sample doping, the composition and concentration of the electrolyte, the illumination conditions, and the temperature; this is the object of the present study. Investigations show that in the classification scheme used in Refs. 6–8, the zeroth type of morphology of the porous structure is formed with the operating point on the first section of the $I-V$ characteristic, the first type of morphology is formed with the operating point on the second section, and so forth. Consequently structures with a given morphology can be formed in the following way. In taking the $I-V$ characteristic one can select the operating point according to the current

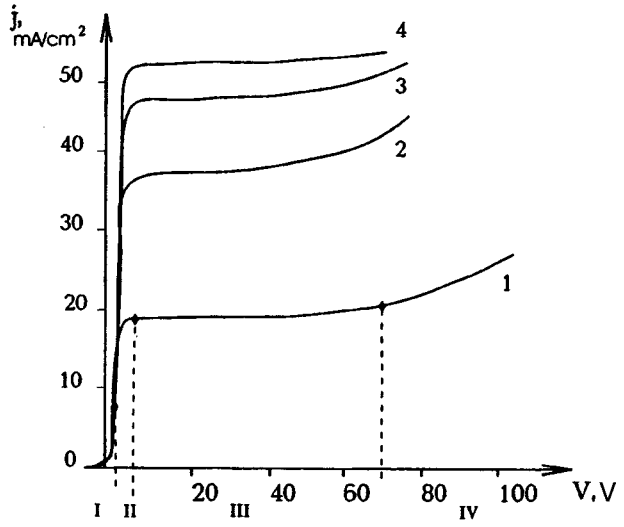

FIG. 1. Current-voltage characteristics taken during anodization in a solution consisting of HF and isopropanol in the ratio 1 : 1 by volume for various anodization parameters — illumination power density J, electrolyte temperature t, °C, anodization time, τ: *1* — $J=0.06$ W/cm^2, $t=30$ °C, $\tau=1$ min; *2* — $J=0.12$ W/cm^2, $t=30$ °C, $\tau=1$ min; *3* — $J=0.12$ W/cm^2, $t=60$ °C, $\tau=1$ min; *4* — $J=0.1$ W/cm^2, $t=60$ °C, $\tau=3$ min. The stabilized anode current during anodization before taking the $I-V$ characteristic was $j=25$ mA/cm^2. The Roman numerals for curve *1* show the sections of the $I-V$ characteristic on which the porous structures with the different pore morphologies are formed.

 1063-7850/97/030244-02$10.00

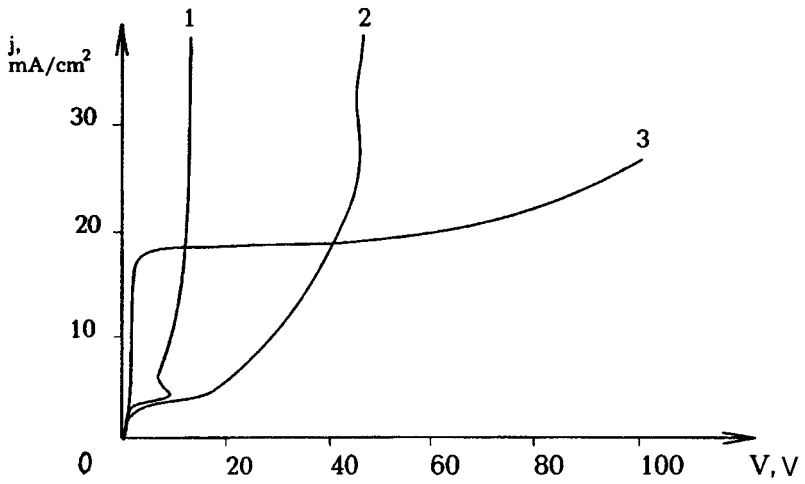

FIG. 2. Current-voltage characteristics, taken during anodization 1 min after the start of the process with stabilized anode current $j = 25$ mA/cm^2 for various electrolyte compositions: *1* — concentrated HF (48% by weight), *2* — a mixture of HF and water (1 : 1 by volume), *3* — a mixture of HF and isopropanol (1 : 1 by volume).

and voltage in the four regions of the $I-V$ characteristic mentioned above, and form any one of the four basic morphological structures or any of them in combination, by moving along the $I-V$ characteristic during the anodization.

It can be seen on Fig. 2 that the $I-V$ characteristic depends strongly on the concentration and composition of the electrolyte. We note that the experiments carried out in Ref. 4 used concentrated HF, while in Ref. 11, a very dilute solution of HF was used. Figure 2 also shows that with the alcohol addition the $I-V$ characteristic takes on a shape for which the sections of the $I-V$ characteristic corresponding to the formation of porous silicon with the different morphologies are very well resolved for certain light intensities, and consequently the conditions for controlled formation of porous silicon with different morphology become optimum.

The overall form of the $I-V$ characteristic is on the whole well accounted for by the theory of kinetics with the generation of minority carriers in the space-charge region[9,10] as applied to the pore formation processes. The distribution of the total potential drop depends on the doping level in the semiconductor, the concentration and composition of the electrolyte, and the potential difference applied to the system.[9] The initial region of increase in the $I-V$ characteristic is described by the Tafel law. The saturation section is described by the formula $j \propto \varphi^{1/2}$ (where j is the current density and φ is the applied potential difference. The second section of growth of the $I-V$ characteristic is explained by breakdown phenomena.[9]

The morphology of the porous structure is determined by the scattering of charge carriers by scattering centers in the semiconductor (impurities, phonons, dislocations, etc.). The probability of scattering of a carrier by scattering centers varies with the carrier energy. For example, in scattering by charged impurities, the scattering cross section decreases with increasing carrier energy, which corresponds to the more elongated shape of the pores with increasing voltage. Thus when the anodization is done with the operating point chosen on the second rise, the porous structure is formed with less branching, with a ''shower'' morphology.

In this investigation we have presented detailed, systematic data from which one can relate the different morphology of the porous structures with the parameters of the electrolyte (HF)-semiconductor (n-type silicon) system used in the anodization. It is thus possible to generate controlled morphology of the porous structure. It has been shown that the morphology of the porous structure is determined by the position of the operating point on the current-voltage characteristic of the electrolyte (HF)-semiconductor (n-type silicon) system. The shape of the $I-V$ characteristic is determined by the parameters of the system: the doping level of the sample, the temperature, the composition and concentration of the electrolyte, and the illumination of the sample. The overall shape of the $I-V$ characteristic is described by kinetic theory with the generation of minority carriers in the space-charge region. It is concluded that the morphology of the porous structure is determined by scattering of the charge carriers by scattering centers, which affords the possibility of simplifying quantitative models reflecting the laws for the formation of various types of morphology of the porous structure.

[1] R. L. Smith and S. D. Collins, J. Appl. Phys. **71**, R1 (1992).
[2] G. Bomchil and R. Herino, L'Echo Recherches **131**, 25 (1988).
[3] V. Lehmann and H. Foll, J. Electrochem. Soc. **137**, 653 (1990).
[4] Y. Arita and Y. Sunohara, J. Electrochem. Soc. **124**, 285 (1977).
[5] S. O. Izidinov, A. P. Blokhina, and L. A. Ismaĭlova Fiz. Khim. Obrab. Mater. **2**, 92 (1987).
[6] É. Yu. Buchin, A. V. Postnikov, A. V. Prokaznikov, V. B. Svetovoĭ, and A. B. Churilov, Pis'ma Zh. Tekh. Fiz. **21**(1), 60 (1995) [Tech. Phys. Lett. **21**, 27 (1995)].
[7] E. Yu. Buchin, A. B. Churilov, A. V. Postnikov, A. V. Prokaznikov, and V. B. Svetovoy, Phys. Low Dim. Str. **2/3**, 97 (1995).
[8] E. Yu. Buchin, A. B. Churilov, and A. V. Prokaznikov, Appl. Surf. Sci. **102**, 431 (1996).
[9] V. A. Myamlin and Yu. V. Pleskov, *Electrochemistry of Semiconductors* [in Russian] (Nauka, Moscow, 1965).
[10] Yu. Ya. Gurevich and Yu. V. Pleskov, *Photoelectrochemistry of Semiconductors* [in Russian] (Nauka, Moscow, 1983).
[11] V. Lehmann, J. Electrochem. Soc. **140**, 2836 (1993).

Translated by J. R. Anderson

Basic rules and effects of structural conditioning

G. E. Skvortsov

M. V. Lomonosov St. Petersburg State University
(Submitted November 28, 1996)
Pis'ma Zh. Tekh. Fiz. **23**, 85–89 (March 26, 1997)

The law of structural conditioning of disequilibrium is discussed. [S1063-7850(97)03303-X]

Four basic rules describing highly nonequilibrium processes were stated in Ref. 1. The application of these rules to a wide range of systems and processes has demonstrated various new aspects and possibilities. The original rules have been modified accordingly and have essentially been elevated to the status of laws.

In this paper we examine the first of these laws: the law of structural conditioning of disequilibrium. We discuss different manifestations of this law: behavioral regularities and structurally conditioned effects.

A characteristic feature of highly nonequilibrium processes is that the effects that arise depend importantly on the structure and its changes in the course of the process. This circumstance is reflected symbolically in the formulation of the law of structural conditionality of disequilibrium: ''disequilibrium is structurally conditioned.''

1. The structure of a system is formed by structural-kinetic elements and the relations between them. In an initial, simplified statement the structure is characterized by quantities such as (for structural-kinetic elements) the mass m_e, the size (diameter) λ_1, the rms velocity v_T (energy of random motion $\varepsilon_T = m_e v_T^2/2$), the binding energy ε_1, the ''lifetime'' (relaxation time) τ_1, and the charge q_e; (for bonds) the average distance between structural-kinetic elements λ_2, the time between ''collisions'' τ_2 ($\tau_2 v_T = \lambda_3$ is the ''mean free path''), and the interaction energy ε_2. These average structural characteristics depend on the external conditions and the intensities of the external influences (''actions'') and are functions of the coordinates and time.

The characteristics of the structure are used for making estimates, determining the similarity of processes, classifying systems, and finding structurally conditioned effects.

2. On the basis of the general dynamical equations for the controlling macroscopic quantities $a_n(xt)$ (Ref. 2), after forming the corresponding structural quantities $a_{ns}(xt)$ from the structural characteristics, we will obtain, in analogy with Ref. 3, a complete system of suitable dimensionless controlling quantities $A_n = (a_n - a_{ne})/a_{ns}$, where a_{ne} is the equilibrium value of a_n.

Using a system of suitable controlling quantities supplemented appropriately to allow for the natural conditions (such as positivity, ''consistency with the action,'' compliance with known similitarity relations, and the ''normed nature of the transition''), we obtain expressions for a set of degrees of disequilibrium. They have the form of a dimensionless products of action factors g and the corresponding structural factors $s[g]$:

$$|gs|:|A_n|:V = \left|\frac{u}{v_T}\right|, \quad E_i = \left|\frac{e}{\varepsilon_i}\right|, \quad P_i = \left|\frac{\dot{e}}{\dot{\varepsilon} i}\right|, \tag{1.1}$$

$$J_n = |(j_n - j_{ne})/j_{ns}|, \ldots;$$

$$F_i = \left|\frac{\tau_i f}{m_e v_T}\right|, \quad \mathrm{res}_n = \left[1 + k_n^{\pm}\left|\frac{a_n - a_{nc}}{a_{nc}}\right|\right]^{-1},$$

$$\mathrm{res}F_i = [1 + l_i^{\pm}|\ldots|]^{-1}, \ldots; \tag{1.2}$$

$$W_{in,j} = |\tau_i \partial_t \ln(|A_n|, F_j)|, \quad H_{in,j} = |\lambda_i \partial_x \ln(|A_n|, F_j)|, \tag{1.3}$$

where u is the velocity, e and $\dot{e}$ are the energy and power of the action on the structural-kinetic elements, j_n is the flux of a_n, and a_{nc} is the threshold value of a_n (resonance, critical point).

Together with the degree of disequilibrium, as a measure of the action and a measure of the change in structure it is appropriate to use the quantities

$$G = gs_0, \quad S = s[g]/s_0, \quad s_0 = s[0]. \tag{2}$$

The values of gs are subdivided, according to the nature of the actions, into active, neutral, and scale (1.3). Active structural disequilibria involve fluxes of mass, momentum, and energy; they appear in the quality boundary law.[1]

3. The set gs (1), describing an ''action–object'' system, has the fundamental properties of universality, completeness, and constructivity. The completeness property means that all the basic relations — the equations of state, the controlling relations, the response functions — can be expressed in terms of gs.

For small values of gs these properties lead to a universal (for any system and any type of action) representation of the basic relations in the form of the linear relations

$$\Phi(gs) \approx \Phi_0 + \sum K_{\Phi n} gs_n, \quad K_{\Phi n} = \frac{\partial \Phi}{\partial gs}/g = 0. \tag{3}$$

We will call the quantities $K_{\Phi n}$ the susceptibility coefficients, which are structurally conditioned quantities; they are realized as the specific heat, the kinetic coefficients, the rate constants, etc. Relations (3) in essence represent the entire classical theory of slightly nonequilibrium processes.

Using the set gs with allowance for it fundamental properties, one can construct a theory of similarity of large disequilibria of process, a generalized Kutateladze dynamical theory of similarity (scaling).[3] Here the set of degrees of disequilibrium specifies a universal scale of disequilibrium,

which allows one to compare processes occurring in different systems and to ''carry over'' effects observed in one system to other systems.

The form of gs shows that at a constant action factor the degrees of disequilibrium increase in magnitude as the structural factor increases. This circumstance makes it possible to determine the potential disequilibrium of systems by means of the ratios of the corresponding structural factors for the different systems. An essentially similar scale of the potential disequilibrium was used in a classification of fluids[2] according to their structural complexity: a larger value of the structural factors corresponds to a more complex structure.

The universality of similarity is ensured by the ''normed transition'' condition, which means that a structural transition corresponds to equality of the active structural disequilibrium to unity. For example, $V=1$ corresponds to a subsonic–supersonic transition (v_{T} is the local speed of sound). Essentially, it was universal similarity that was used in Ref. 4 to carry over to all gases the anomalous relaxation observed for xenon.[4] On this same basis it can be stated that for fluids and solids in shock waves there will be anomalous relaxation at $E_1=1$.

4. Let us indicate several classes of disequilibria of effects, according to the features of the behavior of different sorts of kinetic coefficients.

According to the general expressions for the kinetic coefficients[5,2] we obtain approximate formulas for the viscosity and conductivity:

$$\eta\sim\frac{m_e v_{\mathrm{T}}}{\sigma_e(1-\gamma)\left[1+\dfrac{\tau_1}{\tau_2}+F\right]},\quad \sigma\sim\frac{n_q q^2}{n m_e v_{\mathrm{T}}\sigma_e[\ldots]},\quad (4)$$

$\tau_2=1/n_e v_{\mathrm{T}}\sigma_e$, $\gamma\simeq\pi\lambda_1^3 n_e$, $n_{e,q}$ are the number densities of the structural-kinetic elements and charges, and $\sigma_e(T,P,F)\sim\pi r_1^2$ is the interaction cross section of the structural kinetic elements.

It is clear from Eq. (4) that the behavioral features of the kinetic coefficients are conditioned by the same structural characteristics. Obvious behavioral features are substantially smaller or larger values (in comparison with the average value for the given class of system) or a sharp change (jump) in the characteristics.

4.1. A decrease (increase) in the cross section will lead to an increase (decrease) in the relaxation time τ_2 and in the mean free path and, with them, in the corresponding structural disequilibria; here the kinetic coefficients obviously increase (decrease). An effect of this nature, in consequence of an increase in the cross section as a result of the ionization of argon, is in evidence in the results of Ref. 6.

The effect of a minimum of the cross section, in the form of a maximum of the current, can be observed in a weakly ionized inert-gas plasma at the energies of Ramsauer scattering. In the case of shock waves there are data indicating a sharp increase in the (previously increasing) relaxation time with increasing shock wave velocity.[7] This indicates that the corresponding regime ($u\approx 9$ km/s in air) must be anomalous (it correlates with the regime of shock wave instability that was pointed out in Ref. 8).

4.2. A sharp change in the mass of the structural-kinetic elements leads to diverse nonequilibrium effects.

Rapid dissociation of a gas (e.g., in consequence of resonant laser irradiation) will, according to Eq. (4) with allowance for the approximate formula $\sigma_e\sim m_e^{2/3}$, lead to a decrease in the viscosity as $\eta\sim m_e^{1/3}$.

The Gunn effect, as we know, is conditional on a sharp increase in the effective mass $m_{\mathrm{f}}(E)$ for $E>E_c$. This leads to a drop in conductivity and the onset of a traveling ''domain.''

4.3. Effects of ''turbulization'' (the formation of macroscopic stochasticized structural-kinetic elements) can be regarded as being due to a very strong growth in m_e and a strong decrease in v_{T}.

An estimate of the turbulent viscosity η_{T} relative to the molecular viscosity according to Eq. (4) gives ($\lambda_{1\mathrm{T}}\sim 0.1$ cm)

$$\frac{\eta_{\mathrm{T}}}{\eta}\sim\left(\frac{m_{\mathrm{T}}}{m}\right)^{1/3}\frac{v_{\mathrm{TT}}}{v_{\mathrm{T}}}\sim(10^{19})^{1/3}\frac{u\cdot 10^{-2}}{3\cdot 10^4};$$

at a flow velocity $u=10^3$ cm/s this has a value of the order of 10^3, which is consistent with experience.

Upon an ordinary complex change in the structural parameters, a characteristic indicator of a possible effect is a substantial decrease in the kinetic coefficients upon an increase in the effective action, leading to negativity of the differential kinetic coefficient:

$$K_d=\left(\frac{\partial K}{\partial g}\right)g+K<0. \quad (5)$$

Effects of negativity of a differential coefficient — the onset of instabilities and inhomogeneities — are foremost among the set of disequilibria of effects. This circumstance is directly related to the law of anomalous behavior.[1]

[1] G. E. Skvortsov, Pis'ma Zh. Tekh. Fiz. **16**(17), 15 (1990) [Sov. Tech. Phys. Lett. **16**, 647 (1990)].
[2] G. E. Skvortsov, Vestn. Leningr. Gos. Univ., No. 13, pp. 94–98 (1979).
[3] S. S. Kutateladze, *Similarity Analysis and Physical Models* [in Russian], Nauka, Moscow (1986).
[4] G. I. Mishin, A. P. Bedin, N. I. Yushchenkova, G. E. Skvortsov, and A. P. Ryazin, Zh. Tekh. Fiz. **51**, 2315 (1981) [Sov. Phys. Tech. Phys. **26**, 1363 (1981)].
[5] G. E. Skvortsov, Zh. Éksp. Teor. Fiz. **68**, 956 (1975) [Sov. Phys. JETP **41**, 473 (1975)].
[6] P. P. Kulik, Teplofiz. Vys. Temp. **9**, 431 (1971).
[7] M. B. Zheleznyak and A. Kh. Manatsakanyan, Teplofiz. Vys. Temp. **6**, 390 (1968).
[8] A. S. Baryshnikov and G. E. Skvortsov, Zh. Tekh. Fiz. **49**, 2483 (1979) [Sov. Phys. Tech. Phys. **24**, 1401 (1979)].

Translated by Steve Torstveit

Influence of heterogeneity of an insulating film on its activation process and on the parameters of the thermally stimulated exoelectron emission observed from it

A. I. Vilenskiĭ, V. A. Klyuev, and Yu. P. Toporov

Institute of Physical Chemistry, Russian Academy of Sciences, Moscow

E. S. Revina

Institute of Crystallography, Russian Academy of Sciences, Moscow
(Submitted November 20, 1996)
Pis'ma Zh. Tekh. Fiz. **23**, 90–93 (March 26, 1997)

The influence of surface heterogeneity of an insulating film on its exoelectron emission is investigated. It is shown experimentally that the thermally stimulated exoemission spectra of control samples and samples irradiated for the purpose of creating local regions with a higher electrical conductivity are substantially different, even though the combined surface area of the regions of the film having an irradiation-modified structure comprises an insignificant fraction of the total surface area of the film. © *1997 American Institute of Physics.*
[S1063-7850(97)03403-4]

Methods of exoelectron spectroscopy are finding wide application for studying the structure and properties of various materials.[1] In order to observe thermally stimulated or photostimulated exoemission of electrons from a surface it is necessary to carry out a preliminary activation of that surface. One means of activation of solid surfaces to be investigated by exoemission methods is to treat them in a negative corona in air or in a stream of electrons in vacuum. Here it is assumed that the entire surface to be investigated is irradiated uniformly and that the activating charged particles are localized at biographical defects (traps), which are characteristically present throughout the entire subsurface volume of the sample material, and that the exoemission observed in the subsequent photo- or thermal stimulation characterizes the integrated defect density of the surface under study.

However, there are conditions under which the activating particles can be selectively trapped by individual regions of the surface. In particular, this can occur in activation of insulating films in which there are local charged regions or regions having an increased electrical conductivity. In this case activation occurs only for these local regions, and the observed exoelectron spectrum (curves of the intensity of the exoelectron current versus temperature or versus the energy of the stimulating agent) will be characterized solely by the properties of these individual regions and decidedly not by the surface as a whole.

To check this very important conclusion, which can affect the interpretation of the results of exoelectron investigations, we undertook a special study.

We studied thermally stimulated exoelectron emission from the surface of polyimide films with thicknesses of 10–20 μm. To create local regions with increased electrical conductivity in the film, the latter was irradiated by a stream of Xe^{+6} ions with an energy of 1 MeV/nucleon. The studies showed that in the region where an ion has passed through there is complete destruction of the polymer, with the formation of low-molecular products. Around this zone a polymer region with a modified structure appears. It has been found[2] that the material in the track region has an increased electrical conductivity. Thus current-conducting regions are created in the polymer film. The diameter of these regions in a polyimide film can reach 60 nm.[3] The initial (control) films and the films that had been irradiated by high-energy ions were activated by means of a negative corona in air. For this the film was placed on a grounded metal plate.

The experiments showed that the thermally stimulated exoemission spectra of the initial and irradiated films are substantially different, even though the combined surface area of the parts of the film with an irradiation-modified structure comprises an insignificant fraction of the total surface area. As an example, Fig. 1 shows the glow curves for the initial polyimide film and for a film irradiated by a stream of Xe^{+6} ions. At the fluence employed (10^7 cm^{-2}), there were 10^7 structural altered regions created per square centimeter of the surface, each having an area of 3×10^{-15} cm^2.

Thus the total area of the surface regions with altered structure per square centimeter of the surface was only 3×10^{-8} cm^2, which is an insignificant part of the whole surface of the film. If the stream of charged particles during activation in a corona had uniformly activated the entire surface, then the contribution of the current from the track regions with altered structure to the total thermally stimulated current from the surface of the film would amount to a small fraction (proportional to the modified fraction of the surface). In that case there would be no noticeable difference in the spectra.

On the other hand, if it is assumed that the entire flux of activating particles selectively acts on the track regions, then the observed difference in the character of the glow curves finds a logical explanation.

We note that selectivity of the effect of charged particles on the current-conducting regions of a nonconducting film lying on a grounded metal plate is due to the corresponding configuration of the electric field lines, which curve the trajectories of the charged particles near the surface of the film.

Further confirmation of this conclusion comes from the fact that etching of the damaged layer of the polymer around the track to a depth greater than 35 nm (i.e., the entire layer

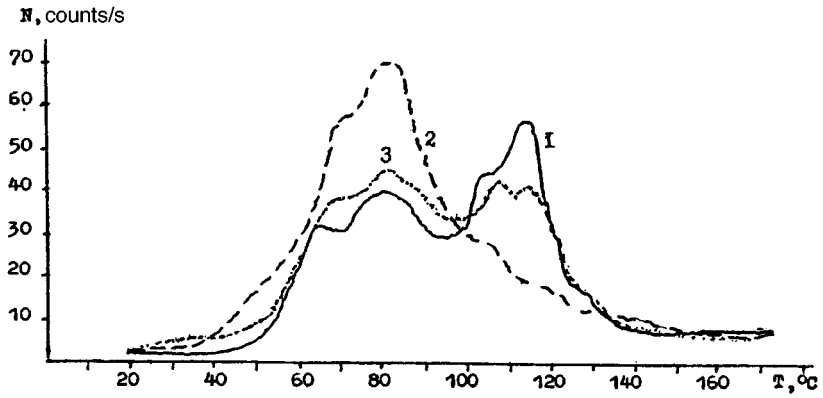

FIG. 1. Glow curves of the thermally stimulated emission of polyimide films: *1* — The initial film, *2* — after irradiation by a stream of Xe^{+6} ions, *3* — after a subsequent etching of the irradiated film for 200 min in a 30% solution of hydrogen peroxide.

with disrupted structure), with the formation of ''through'' channels, restores the character of the glow curve (see curve *3* in Fig. 1). We note that the reason why curves *1* and *3* are not identical is that the etchant acts not only on the structurally damaged polymer but also, to some extent, on the initial material.

Thus the data presented here demonstrate that in employing exoemission analysis to study the density of structural defects in insulating materials one must allow for the possibility that conditions of nonuniform activation of the defects will be created, and the results of the measurements must be interpreted accordingly.

[1] V. S. Kortov, A. I. Slesarev, and V. V. Rogov, *Exoemission Monitoring of the Surface of Manufactured Items After Treatment* [in Russian], Naukova Dumka, Kiev (1986).
[2] A. I. Vilenskiĭ, V. A. Oleĭnikov, B. V. Mchedlishvili *et al.*, Khim. Vys. Energ. **26**(4), 12 (1992).
[3] A. I. Vilenskiĭ, N. G. Markov, V. A. Oleĭnikov *et al.*, Khim. Vys. Energ. **28**(6), 507 (1992).

Translated by Steve Torstveit